Interfaces and Dynamics in Polymeric 3D Printing and Crystalline Polymer Blends

A Dissertation Presented for the

Doctor of Philosophy

Degree

The University of Tennessee, Knoxville

Stevenson Connor Perryman

December 2021

Copyright © 2021 by Stevenson Connor Perryman
All rights reserved.

Dedication

This dissertation is dedicated to my loving parents, Mike and Michelle Perryman, whose unwavering support, pride, and devotion, as the amazing people they are, has seen me through hardship, struggle, and the growth of myself into who I am today.

Acknowledgements

I wish to acknowledge the financial and academic support of Dr. Mark Dadmun, who's patience and dedication as a researcher and mentor has been above and beyond the call in the six years I have spent in my scientific growth. I would like to thank my committee members Dr. Brian Long, Dr. Kevin Kit, Dr. Joseph A. Baccile, Dr. Christopher Baker, and Dr. Frank Vogt (may he rest in peace), for their considerable time and input on my journey to completing my doctorate. I would also like to thank all my lab mates, past and present, for their collaboration, assistance, and companionship over the years, including Mr. Jacob Fischer, Mr. Kaizhong Guan, and Mr. Austin Riggins. I am especially thankful to Mr. Joshua Moncada and (by extension) his wife, Dr. Rachel Ramirez, for their advice and genuine care for my everyday struggles both in and out of graduate school. Last, but not least, I am forever grateful for the kinship and true friendships I have grown in my time here. To the Dr's Andrew and Alisha Pedersen, thank you, for your kindness, companionship, and all the birthday wishes and gifts. To my friends who carried me on through this endeavor with stiff encouragement or stiff drink: Nathan Harms, Caleb Garrett, and Kyle Huffstater. And last of all, to my best friend Luther Langston and his wife Melissa, whose love and openness helped me to fully grow out of my shell and find a true home away from home.

Abstract

This dissertation presents experimental work that provide a foundation to rationally improve fused filament fabrication (FFF) and immiscible blend compatibilization. Objects generated from additive manufacturing processes, such as FFF, have intrinsic structural weaknesses which include two project specific examples: structural anisotropy and irreversible thermal strain. Due to low adhesion between individual print layers that results in macroscopic defects, the mechanical strength of printed objects when force is applied perpendicular to the build orientation is drastically reduced. In the first dissertation chapter, we present a protocol to produce interlayer covalent bonds by depositing multi-amine additives between individual layers of a print to strengthen interlayer adhesion during the FFF printing process. Upon deposition, the amines then react with the deposited filament via functional groups produced by oxygenation to form the covalent crosslinks. Results demonstrate that the majority of amine crosslink reactions occur shortly after filament deposition from the residual thermal energy of extrusion, and that the amine reactivity is not the prevailing factor in determining the direct changes to print strength and interlayer fracture energy. The focus of our next project is to evaluate the effects of nanoscale additives on irreversible thermal strain ($\boldsymbol{\varepsilon}$) build-up within 3D printed poly (lactic acid) (PLA) monoliths by measuring the change in this irreversible thermal strain with annealing. Once the contributions of internal void spaces were removed, the results of the modified strain value, $\boldsymbol{\varepsilon_z^*}$, indicates that incorporation of low molecular weight 3-arm star PLA chains into the print filament increases print $\boldsymbol{\varepsilon}$ while pure PLA or graphene modified filaments have similar $\boldsymbol{\varepsilon}$. By correlating the strain measurements with results of a filament calorimetry experiment, it was shown that print irreversible thermal strain is influenced directly by how an additive changes the viscosity and

molecular dynamics of the deposited polymer chains. In the third project, we examine the use of telechelic oligomers to optimize the physical properties of crystalline polymer blends via reactive compatibilization. The results demonstrate that the blend properties are influenced by three molecular level processes that are governed by the loading of oligomers used for compatibilization. Ultimately, the detrimental effects of plasticization from excess oligomer in the blend can be avoided and optimized alongside the synergistic relationship of blend crystallinity and reactive compatibilization by using a targeted concentration of telechelic additive.

Table of Contents

Chapter 1. Introduction....1
An Introduction to Fused Filament Fabrication (FFF) 2
Common Weaknesses of Fused Filament Fabrication....5
3D Printing and Mechanical Anisotropy....5
Irreversible Thermal Strain within FFF Prints....9
Immiscible Polymer Blends and Compatibilization....10
Thermodynamic Model of Polymer Blends....11
Compatibilization via Copolymers....13
Reactive Telechelics Oligomers and In Situ Compatibilizers....16
Dissertation Outline and Objective....19
Chapter 2. Interlayer FFF Crosslinking Additives and Rate Analysis of Post-Deposition Reactions....21
Abstract....22
Introduction....23
Experimental....27
Materials....27
Interfacial Adhesion Determination....27
Infrared Spectroscopy of Butadiene Oxidation....29
Results and Discussion....32
Mechanical Testing and Quantifying Crosslink-Induced Isotropy....32
Adhesion Measurements with Varying Print Pause Time....36
Reaction Kinetics via Infrared Spectroscopy....37
Qualitative Analysis of Reaction Kinetics....39
Conclusion....53
Chapter 3. Nanoscale Additives and Irreversible Thermal Strain in Fused Filament Fabrication....55
Abstract....56
Introduction....58
Experimental....62

Materials and Filament Composite Production....62
Sample Printing, Thermal Annealing, and Sample Analysis....63
Scanning Electron Microscopy and Void Space Analysis....64
Glass Transition of Monoliths....64
Results....67
Additive Influence on Irreversible Thermal Strain (ε)....67
Void Space and Additional Strain Contributions....70
Filament Glass Transition Behavior....75
Discussion....79
Conclusion....82
Chapter 4. Immiscible Blend Changes Induced by Telechelic Oligomers and Biphasic Interface Copolymers....84
Abstract....85
Introduction....87
Experimental....91
Materials....91
Blend Dogbone Sample Production and Mechanical Property Testing....92
Differential Scanning Calorimetry and % Crystallinity Methods....92
Results and Discussion....95
Blend Mechanical Properties with Increasing Oligomer Concentration....95
Impact of PEO Crystallinity on Blend Properties....97
PEO Crystalline Changes and Blend Molecular Interactions....98
Blend Morphology and Predictive Models....107
Conclusion....112
Chapter 5. Conclusions and Future Work....114
Conclusions....115
Multi-Amine Additive and Interfilament FFF Crosslink Reactions....116
FFF Strain (ε) Variations with Nanoscale Additives....116
Crystalline Polymer Blend Compatibilization....118
Summary....119

Future Work.....120
Interlayer Crosslinker Reactions with Various Filament Backbone Functionalities 121
Chain Alignment Effects on Interfilament Entanglement and Strain (ε).....122
Dual Crystalline Polymer Blends and Reactive Compatibilization.....122
References.....124
Vita.....133

List of Tables

Table 2.1 Infrared signal assignments for Oxidized Polybutadiene and Crosslinker.....41

List of Figures

Fig. 1.1 Diagram of the components of a fused filament fabrication extruder tool and the layer-by-layer deposition of filament beads in a printed object.....4

Fig. 1.2 Interfilament bead adhesion process within an FFF print **a)** initial bead contact following extrusion **b)** initiation of bead to bead polymer diffusion **c)** entanglement and further diffusion of chains.....6

Fig. 1.3 Phase diagram of a two polymer blend system as depicted by the temperature of the mixture and the volume fraction of the polymer components…….....14

Fig. 1.4. Sequence distributions of various copolymer additives and the resulting biphasic interface architecture following blend compatibilization. …….....17

Fig. 1.5 Formation of a blend compatibilizing di-block copolymer from the reaction of carboxylic acid and epoxy telechelic oligomers.....18

Fig. 2.1 a. Illustration of an FFF object's build orientation and physical response to an increasing uniaxial force. **b.** Thermal history of an individual layer in a sample cube as recorded via thermal camera……...……25

Fig. 2.2 Chemical structures of the crosslinkers used in this study **a.** 4,4-diaminodiphenyl methane, **b.** 4,4'-diaminodicylohexylmethane, and **c.** pentaethylene hexamine……30

Fig. 2.3. a. Illustration of printed sample cube and **b.** Completed sample machined from cube.....31

Fig. 2.4. a. 3D model of Instron grips for fracture energy tests **b.** Image of sample tested with Instron and **c.** Typical force vs. displacement curve of fracture energy tests.....33

Fig. 2.5. a. Average fracture energy vs. interlayer crosslinker concentration **b.** Interfacial fracture energy as a function of print pause time.....34

Fig. 2.6. Modulus of printed tensile dogbones with and without crosslinker applied to each layer.....35

Fig. 2.7. a. Thermal camera imaging of the printing process **b.** Plot of average temperature as a function of time after layer completion.....40

Fig. 2.8. a. Infrared spectra analysis and peak assignment for an oxidized polybutadiene/DADPM mixture and **b.** Atomic stretching and signal assignment of DADPM's primary amine.....42

Fig. 2.9. a. Relative peak area of primary amines and **b.** Secondary amines as a function of annealing time for 10 wt% DADPM and oxidized PB.....45

Fig. 2.10. a. Relative peak area of primary amines and **b.** Secondary amines as a function of annealing time for 30 wt% DADPM and oxidized PB.....46

Fig. 2.11. a. Relative peak area of primary amines and **b.** Secondary amines as a function of annealing time for 10 wt% DADCM and oxidized PB.....47

Fig. 2.12. a. Relative peak area of primary amines and **b.** Secondary amines as a function of annealing time for 10 wt% PEH and oxidized PB.....48

Fig. 2.13. a. Primary (k_1') and secondary (k_2') DADPM amine rate constants and **b.** Combined (k') DADPM reaction rate constants at different annealing temperatures.....49

Fig. 2.14. a. Primary amine (k_1'), **b.** Secondary amine (k_2'), and **c.** Cumulative (k') pseudo depletion rate constants for each crosslinker species at set anneal temperatures.....52

Fig. 3.1. Illustration of print warpage in an FFF process as established layers are cooled or thermally annealed.....60

Fig. 3.2. Processing steps of dimensional analysis and SEM imaging for 3D printed monolith samples.....65

Fig. 3.3. Imaging stages of % area void space analysis consisting of **a.** raw images from SEM **b.** threshold filtration to isolate void spaces and **c.** pixel counting for area estimation.....66

Fig. 3.4. Irreversible thermal strain (ε) of printed monoliths in the **a.** Y-axis direction and **b.** Z-axis direction with various filament additives.....68

Fig. 3.5. Illustration of filament bead transformation in 3D printed monoliths before and after annealing.....69

Fig. 3.6. Scanning electron microscopy images of 3D-printed monolith interfilament void space after **a-c)** 1.25 minutes and **d-f)** 24 hours of annealing at 85 ºC.....71

Fig. 3.7. Interfilament void space area changes within printed monolith samples as a function of annealing time.....73

Fig. 3.8. Irreversible thermal strain (ε^*) of 3D printed monoliths in the z-axis direction adjusted for void space area.....74

Fig. 3.9. Calorimetry scans for pure (listed here as "blank") PLA monoliths after set annealing times.....77

Fig 3.10. Measured enthalpy of the glass transition endotherm as a function of monolith annealing time.....78

Fig. 3.11. Endothermic glass transition enthalpy as a function of Z-axis monolith thermal strain adjusted for void space.....80

Fig 4.1. Diagrams of minor phase droplet coalescence in an immiscible polymer blend **a)** and the formation of blocky copolymer from the reaction of telechelic oligomer end groups at the biphasic interface **b).**.....89

Fig. 4.2. Molecular structures of both the homopolymer and oligomer species used in this study with paired end chain functional groups, PEO **(top)**/ PBAE **(bottom)**.....93

Fig. 4.3. 70/30 PBAE: PEO blend tensile sample generation and analysis via melt mixing and extrusion, dogbone mold setting, tensile analysis, and calorimetry.....94

Fig. 4.4. Modulus and maximum elongation values versus **a)** reactive and **b)** unreactive wt% telechelic oligomer for a 70/30 PBAE: PEO blend.....96

Fig. 4.5. a) Modulus and **b)** Maximum Elongation values of 70/30 PBAE: PEO tensile samples with ≤ 2 wt% reactive telechelics as a function of wait time at room temperature.....99

Fig. 4.6. Calorimetry scans of a 70/30 PBAE: PEO blend with 0.5wt% reactive telechelic oligomers at increasing time spans at ambient temperature and the subsequent PEO phase melt enthalpy measurements.....101

Fig. 4.7. Calculated % PEO crystallinity for 70/30 PBAE: PEO blends with 0 (Pure) to 2 wt% reactive telechelic oligomers as a function of ambient temperature wait time.....102

Fig. 4.8. Changes in modulus vs. % PEO crystallinity for 70/30 PBAE: PEO blends with 0 (Pure) to 2 wt% reactive telechelic oligomers.....104

Fig 4.9. Diagram of molecular interactions in a 70/30 PBAE: PEO blend with telechelic oligomers at low loadings and the observed mechanical properties.....106

Fig. 4.10. SEM image of a 90:10 wt% Polystyrene/Polyisoprene blend compatibilized with telechelic oligomers (image from Ashcraft et. al.).[113] Scaling bar of image is 10 μm.....108

Chapter 1: Introduction

An Introduction to Fused Filament Fabrication (FFF)

Additive manufacturing (AM) is a relatively new object creation process that generates complex 3D objects in a rapid and accurate manner and has received large interest for development from the materials science community.[1] Various technologies used in AM have come to include Selective Laser Sintering (SLS), Stereolithography (SLA), and Fused Filament Fabrication (FFF) processes. Although each of the AM processes accomplish object generation through very different methods, each process is akin to two-dimensional printing but applied in 3D space. This distinct similarity between each technology places them beneath the umbrella term for AM production, 3D printing.[2] Prized for its ease of use and open-source foundation, FFF is an AM technology that has seen considerable interest from the hobbyist, commercial, and academic communities. Since the start of the 21st Century, research publications concerning FFF subjects have grown steadily from tens of papers a year to hundreds that cover everything from aerospace and automotive engineering to biomedical and medical research.[3, 4] As a result, a significant number of FFF publications concern the mechanical robustness of printed objects to increase the efficiency and accuracy of the technology at large scales. One prominent example of the steps being taken to move 3D printing into large-scale production devices is the Big Area Additive Manufacturing (BAAM) device used by the Manufacturing Demonstration Facility (MDF) of Oak Ridge National Laboratories.[5, 6]

FFF prints are first designed with the use of computer-aided design (CAD) software in 3D digital space. 3D model files are then converted to a set of two-dimensional layer "slices" with the use of various open-source slicing programs. The 2D file format is then interpreted by the printer's operating system to render the "slices" together into the original object using print parameters such as bed temperature, extrusion speed, and raster angle. Heated to the appropriate extrusion

temperature, filaments of thermoplastic polymer with fixed diameters are then pushed via electronic motors through a metallic nozzle where the material is rapidly converted to a semi-molten state and extruded. The filament material is then deposited with a nozzle determined diameter as individual “fibers” or “beads” in the X and Y-axis onto a heated bed system in two-dimensional layers that are covered in the Z-axis by subsequent layers until the 3D object is complete. An illustrative diagram depicting the general FFF extrusion and print building process as depicted in Figure 1.1.

Typical filament materials used in FFF consist of thermoplastic resins that are easily processed at moderate temperatures. Polymers such as Polylactic Acid (PLA) or Acrylonitrile-Butadiene-Styrene (ABS) are the most commonly used due to their high processability from a combination of desired flow properties and low melting or pseudo-melting temperatures. PLA, a biodegradable polymer with high economic demand, is a semi-crystalline polyester. The monomer is derived from starch fermentation of various crops such as sugar beets or corn and then polymerized via ring-opening polymerization of the cyclic dimer, lactide.[7, 8] ABS, an amorphous terpolymer, is made with a wide variety of compositions that lead to deviations in the observed material strength and thermal properties. Each polymer species contributes to the overall material characteristics, where styrene generates hardness and rigidity, polybutadiene provides ductility and improved toughness due to its rubber-like behavior, and acrylonitrile increases the overall chemical, fatigue, and heat resistances.[9]

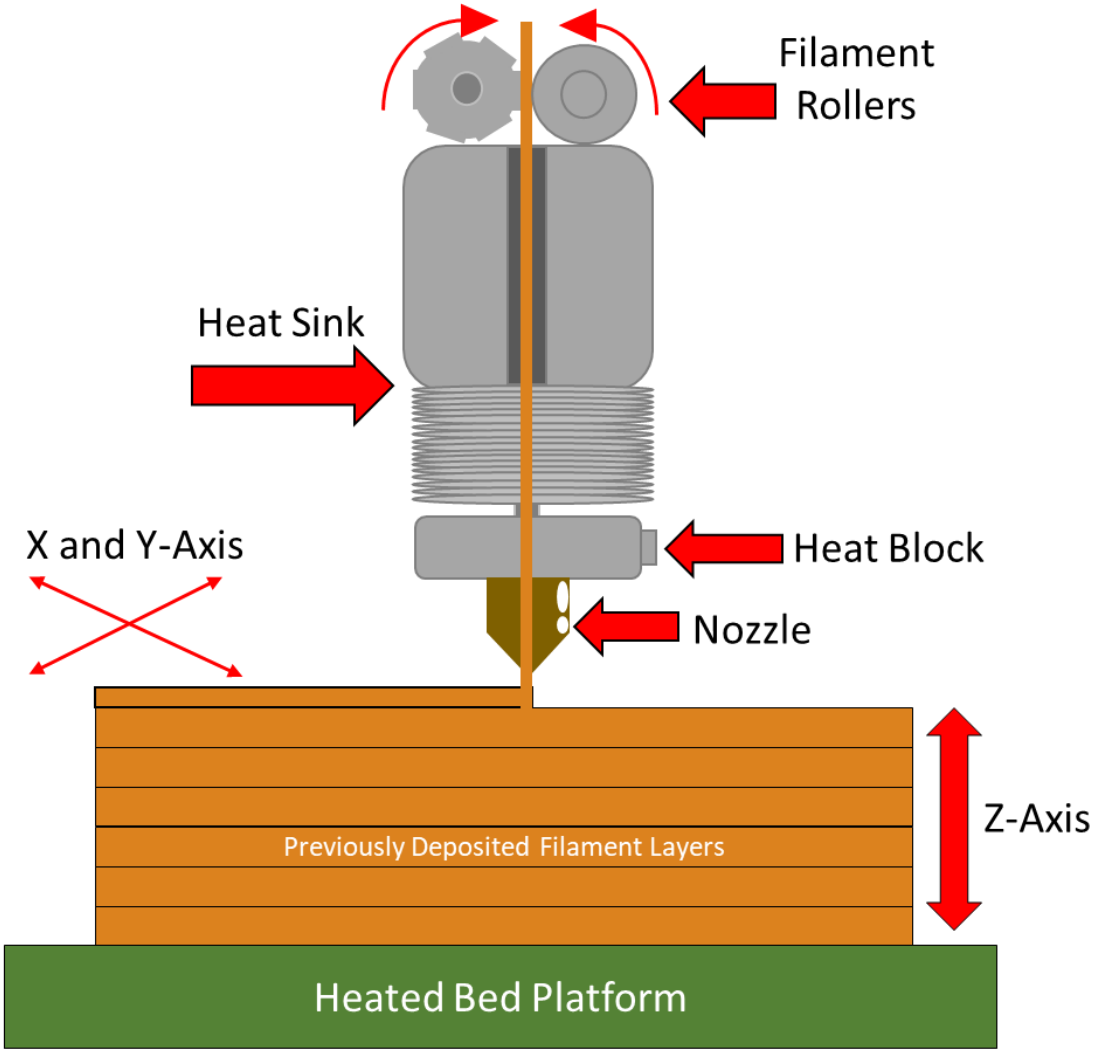


Fig. 1.1. Diagram of the components of a fused filament fabrication extruder tool and the layer-by-layer deposition of filament beads in a printed object.

Common Weaknesses of Fused Filament Fabrication

3D Printing and Mechanical Anisotropy

As discussed above, 3D printed objects are generated when an FFF device deposits individual "fibers" or "beads" of semi-molten polymer material adjacent to one another in two-dimensional layers. The layers are extruded consecutively upon each other in the Z-axis until the desired object is formed. When the semi-molten filament is extruded, the material is cooled below the glass transition by conduction with the surrounding air and bead neighbors. This return to the glassy state then prevents filament material from diffusing entirely into the surrounding polymer and generates interfilament void spaces based on the rate of cooling. From this layer-by-layer build process, structural anisotropy emerges and generates inconsistencies in the print's mechanical properties that limit the potential applications of 3D printed objects.[10-12] As opposed to an isotropic material where mechanical properties are independent of force direction, the two dimensional deposition of the filament material leads to different strength and modulus values depending on the orientation of an applied force. When a uniaxial force is applied parallel to the filament bead orientation, the polymer material of each layer is stressed isotropically along the same force vector, leading to the highest tensile properties for the printed object. If the same force is applied perpendicular to the two-dimensional orientation of the print layers, the interlayer interface is only maintained by the quality of interfilament bonding. This bond quality is directly related to the formation of interbead and interlayer welds and by extension the degree of polymer interfilament diffusion that occurs as the material is above the glass transition.[13-15] The stages of bead welding and interfilament diffusion between individual filament beads is depicted in Figure 1.2. The degree of welding and interfilament diffusion is influenced by several criteria, such as the polymer's thermal properties, print build parameters, and the complex thermal history of the filament.

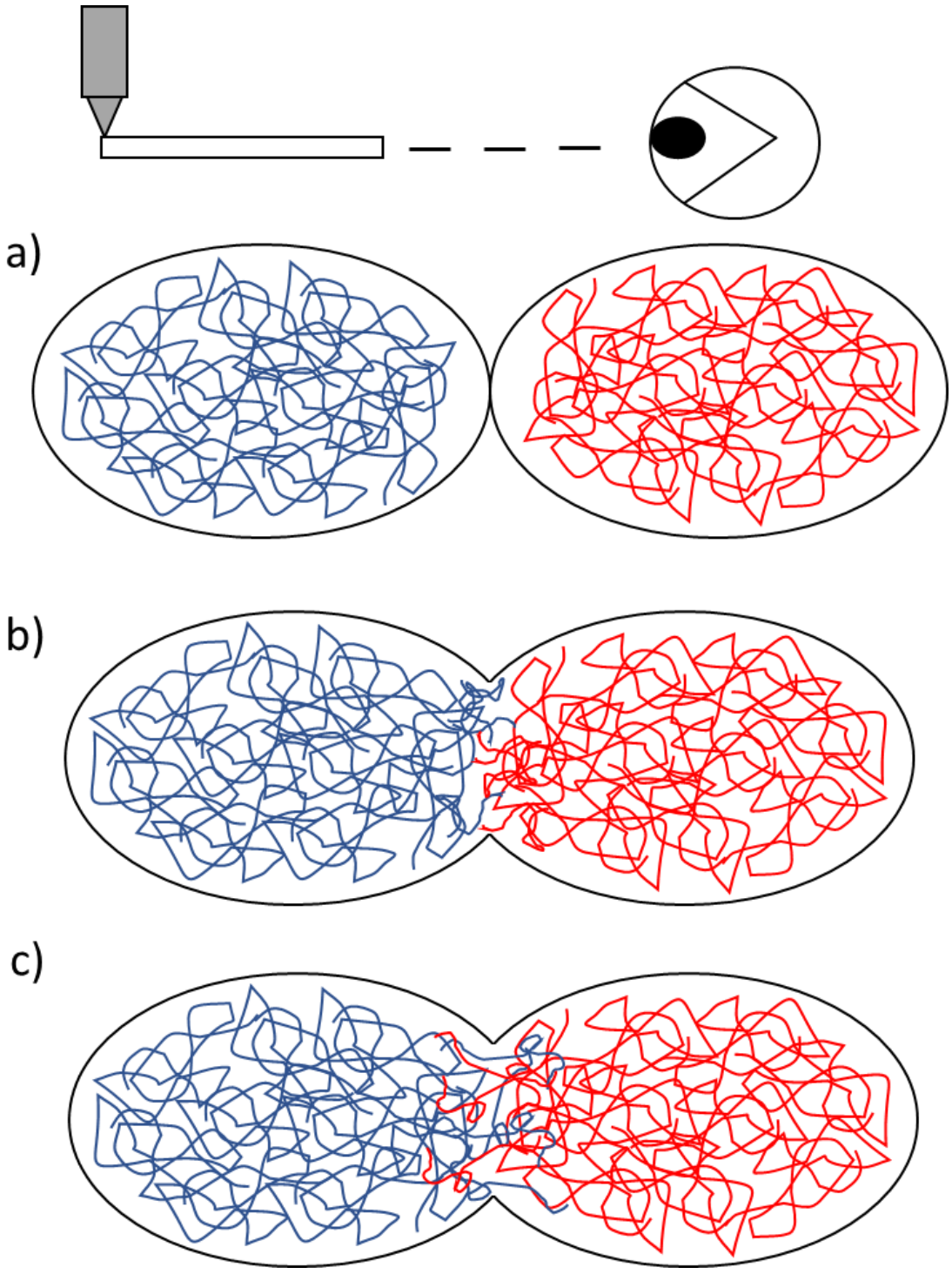


Fig. 1.2 Interfilament bead adhesion process within an FFF print **a)** initial bead contact following extrusion **b)** initiation of bead to bead polymer diffusion **c)** entanglement and further diffusion of chains.

Therefore, a large portion of modern FFF research is dedicated to manipulating the thermodynamic, molecular, and physical factors inherent to polymer filament and the print process to limit anisotropy.[16, 17]

Various chemical and engineering methods have been used to remove the weaknesses of anisotropy. One direct method is thermal annealing of completed prints. When filament material is heated above the glass transition, interfilament diffusion between the print beads is enhanced and leads to increased entanglements at the interface that generate more isotropic material characteristics. Annealing at elevated temperatures also lead to ordered structural changes in semi-crystalline polymer filaments. For instance, Wach et. Al. annealed PLA samples at various temperatures above the T_g and determined that higher temperatures led to faster interfilament crystal formation and higher tensile properties.[18] Although thermal annealing is a direct and simple method to mechanical improvements, the elevated thermal exposure typically leads to undesirable print warpage through the release of irreversible thermal strain. Another method of print mechanical improvement is the use of nanoscale additives that induce thermal, chemical or polymer dynamic changes in the filament material. A family of materials that has gained traction in research to improve print tensile properties is the various structures of carbon nanoparticles such as graphene, carbon nanotubes, and microdiamond aggregates. Typical benefits to 3D printer material include an enhanced elastic modulus and increased thermal stability alongside a reduction in both creep and the linear thermal expansion coefficient.[19-21] The use of nanoparticle additives, while beneficial in set weight percent concentrations, can also be detrimental to the print material. Overloading of the polymer material with nanoparticle additives is likely to induce higher material rigidity, which can be an undesirable trait when the printed part is used in certain applications, such as the biomedical field.

Although moderate removal of anisotropy has been observed with print parameter manipulation and the addition of thermomechanical modifying nanoparticles, the scope of FFF research has yet to fully utilize the numerous chemical possibilities of the assorted filament materials. In addition to the abundant number of functional groups in the backbone of certain filament chains, FFF filaments can be chemically modified either prior to or during the printing process to enhance the interfilament diffusion or generate new forms of interfilament bead connectivity. Once filament bead bonding is improved, a reduction in anisotropy is the likely outcome. For instance, Shaffer et. al. utilized two separate reactive pathways to achieve covalent crosslink formation between individual filament beads to enhance the overall interfilament bond strength.[22] By placing radiation sensitive crosslinker additives into filaments of PLA and acrylate thermoplastics, it was shown that the mechanical performance of printed samples was drastically improved following direct exposure to gamma radiation that induced covalent crosslink formation between the print layers. In a more recent example, Li et. al. developed an interesting method of interlayer adhesion improvement for high performance polyether ether ketone (PEEK) filament.[23] This was accomplished by introduction of a complex silsequioxane species that reacts via pyrolysis during the high temperature deposition process which then plasticized the interfilament interface. The benzene-derivative byproducts of the pyrolysis reaction then induced more complete interfilament diffusion that drastically improves the mechanical performance of PEEK prints. Ultimately, the branch of interfilament chemical reactions and their dynamics within the FFF process is still a relatively new concept and has yet to fully incorporate the complex thermal and shear history of a 3D printer. More specifically, the potential for certain reactions is heavily dependent upon the available thermal energy to induce crosslinking or other reactions, which is dependent upon the complex thermal history of a print and various print parameters such as

extrusion temperature and nozzle speed. In addition, these studies have yet to model how a reaction's kinetic rates may change under this fluctuating thermal environment.

Irreversible Thermal Strain within FFF Prints

Another common issue within FFF is the generation and accumulation of irreversible thermal strain (ε) within the layers of a print. Irreversible thermal strain is created within a printed structure due to the complex thermal history of the filament material as it is deposited, cooled, and re-heated by subsequently deposited filament beads. At the extrusion temperature, interfilament chains in the molten, rubbery state are stretched via shear forces of the hot nozzle to establish a layer's individual beads. When the filament is stretched by these forces, unfavorable deformations in the polymer matrix are then locked into place when the filament is cooled to the glassy state. The magnitude and generation of these unfavorable conformations is not a consistent process, and various portions of a print geometry will have inconsistent buildup of stresses due to the uneven distribution of thermal energy throughout the print. As a result, because the initial generation of the irreversible thermal strain itself is inconsistent, filament beads with trapped chain conformations will release the stored stress on an inconsistent basis. When the irreversible thermal strain is released, this process is observed macroscopically as a variety of different phenomenon, including object dimensional warpage and cracks between individual layers. The presence of these cracks or object warpage then ultimately prevents 3D printed objects from being utilized in specific part applications where uniform object dimensions or strong structural integrity is required.

Much like anisotropy, the various parameters used to generate printed objects have been modified to decrease the overall amount of irreversible thermal strain. Changes in raster angle, the rate of filament extrusion, nozzle temperature, and layer thickness have all been studied, with some moderate success in decreasing the strain buildup.[24-26] Although these studies have lessened the

effects of irreversible thermal strain, the overall deformation and transformation of printed objects still remains a large hurdle to 3D printing viability. As a change in focus for this specific issue, our research group and others have moved away from influencing the print parameters. Experimental emphasis is now to pinpoint the changing internal polymer dynamics and interactions at the molecular level when filament material is deposited and cooled. Recently, this research has focused on the use of nanoscale additives, which are introduced to FFF filament via melt blending, solution encapsulation, or other various methods. One of the more promising additives with conclusive results thus far is graphene, which has been shown to increase interfilament diffusion by enhancing a filament's thermal conductivity.[27]

Immiscible Polymer Blends and Compatibilization

The blending of two or more polymer materials that are physically or chemically dissimilar is an important material production method that has been used to make new materials that combine the physical properties of each component, resulting in a single product that exhibits tailor-made properties. However, without the use of a chemical compatibilizer, most polymer blends will separate from the incompatible thermodynamic nature of the components into distinct phases that are separated by a weak polymer-polymer interface, known as the biphasic interface. To prevent further dispersion and enhance the interface between the blend components, compatibilizers act as a buffer region that blocks further aggregations of the lower concentration polymer, or minor phase, from occurring. Due to the chemical nature of a compatibilizer, the material will selectively segregate to the interface between the thermodynamically incompatible polymer phases.[28, 29] One of the most important aspects of compatibilization is the time needed for the compatibilizer to diffuse to the biphasic interface from the bulk, which is heavily influenced by the molecular properties of the material. Interfacial compatibilizers that can reach the biphasic interface at a faster

rate than other substances have higher probabilities to ensure that the blend becomes compatibilized before complete phase segregation is achieved. Since copolymer compatibilizers are perhaps the most important form of compatibilizers used in polymer blending, it is vital to understand the thermodynamics of polymer diffusion in a blend, as it relates to both the copolymer additive and the homopolymers being compatibilized.

Thermodynamic Model of Polymer Blends

The mixing of chemicals together in a blend is understood thermodynamically by utilizing the standard Gibb's free energy equation for mixing (Equation 1.1), where the free energy of mixing for two polymer species together is represented by ΔG_m. The Gibbs free energy value is composed of both the enthalpy and entropy of the system, which change as a direct result of the mixing process. The entropy term, ΔS_m, accounts for all possible arrangements of the two polymers in the blend at a given temperature, while the repulsive and attractive molecular interactions are modeled by the ΔH_m value. A homogeneous mixture is then generated when the combination of these two terms results in a negative net ΔG_m value. Conversely, when the two components are too molecularly dissimilar, a sufficient increase in the enthalpic term or a general decrease in the entropic term generates a positive Gibbs free energy, leading to a thermodynamically driven separation of the polymer phases.

$$\Delta G_m = \Delta H_m - T\Delta S_m \qquad \text{Equation 1.1}$$

For both ideal solutions and polymer mixtures, the Gibbs free energy equation contains all the appropriate terms and is the most accurate model to use for complex polymer blend systems. However, the unique difference between ideal solution samples and polymer chains is the process by which the entropy and enthalpy terms are accounted for. Since the standard Gibbs equation is

used to model an exponential number of configurations of individual molecules in an ideal solution model, the standard enthalpy and entropy values cannot account for the large molecular weights of individual polymer chains where the covalently linked monomer units are bound and cannot rearrange into nearly as many conformations. This limited mobility then results in a smaller entropic term that contributes to the general immiscibility of most polymer blend combinations. To account for these limited configurations, analytical equations for both the ΔH and ΔS terms were developed from studies on polymer solution dynamics from a lattice approach developed independently by both Flory and Huggins in the 1940's.[30, 31] This modified equation, observed as Equation 1.2, accounts for both the number of either polymer or solvent molecules (n_i) and the volume fraction of each component (φ_i).[32]

$$\Delta G_m = RT[n_1 ln\phi_1 + n_2 ln\phi_2 + n_1\phi_2\chi_{12}] \qquad \text{Equation 1.2}$$

From the standard Gibb's free energy equation, the entropy of mixing term is replaced by the addition of the first two terms in the equation brackets. Similarly, the enthalpy of mixing value is supplanted by the third term, where the interpolymer interactions based on solubility and other energy parameters are represented by χ_{12}.

Flory-Huggins theory can be used to predict the range of blend compositions where the two components will phase separate as the volume fraction values of φ_1 and φ_2 are changed. By utilizing the thermodynamic requirement that individual phases maintain equivalent chemical potentials, the theory leads to derivations in plots of the Gibbs free energy vs the blend composition that denote where the blend is in a two phase or single-phase arrangement. Composition boundaries that separate the single and two phase regions are represented as a curve in these plots and known as the binodal. Subsequently, the rapid transition of a miscible blend through a thermodynamically

unstable, or metastable, phase, where phase separation is constricted via kinetic processes, is plotted on phase diagrams as the spinodal. The point of contact between the spinodal and binodal curves is designated as the critical point, where the temperature associated with this composition is known as the critical solution temperature or CST. Depending upon whether blend miscibility is above or below the CST value determines whether the blend has an Upper or Lower Critical Solution Temperature, UCST and LCST respectively, where the components of a polymer mixture are thermodynamically driven towards the formation of a single phase, homogeneous material. Although the Flory-Huggins theory is accurate enough to designate the existence of the spinodal, binodal, and critical point for UCST determination, the theory does not consider the effects of free volume. Comprehensive analysis of a blend's thermodynamics that extend the Flory-Huggins theory to include parameters of density and compressibility at various compositions and temperatures can circumvent these limitations to produce accurate models of phase diagrams for polymer blends with either the UCST or LCST determined.[33] An example of these comprehensive diagrams is seen below as Figure 1.2.

Compatibilization via Copolymers

In the generation of polymer blends, the original chemical and thermomechanical natures of each component that make their properties a desirable attribute to have within a blend are often the same properties that prevent the blend from becoming thermodynamically compatible. When incompatibility becomes an issue, the primary solution to utilize in blend formation is the use of chemical compatibilizers that simultaneously increase phase dispersion by modifying the blend

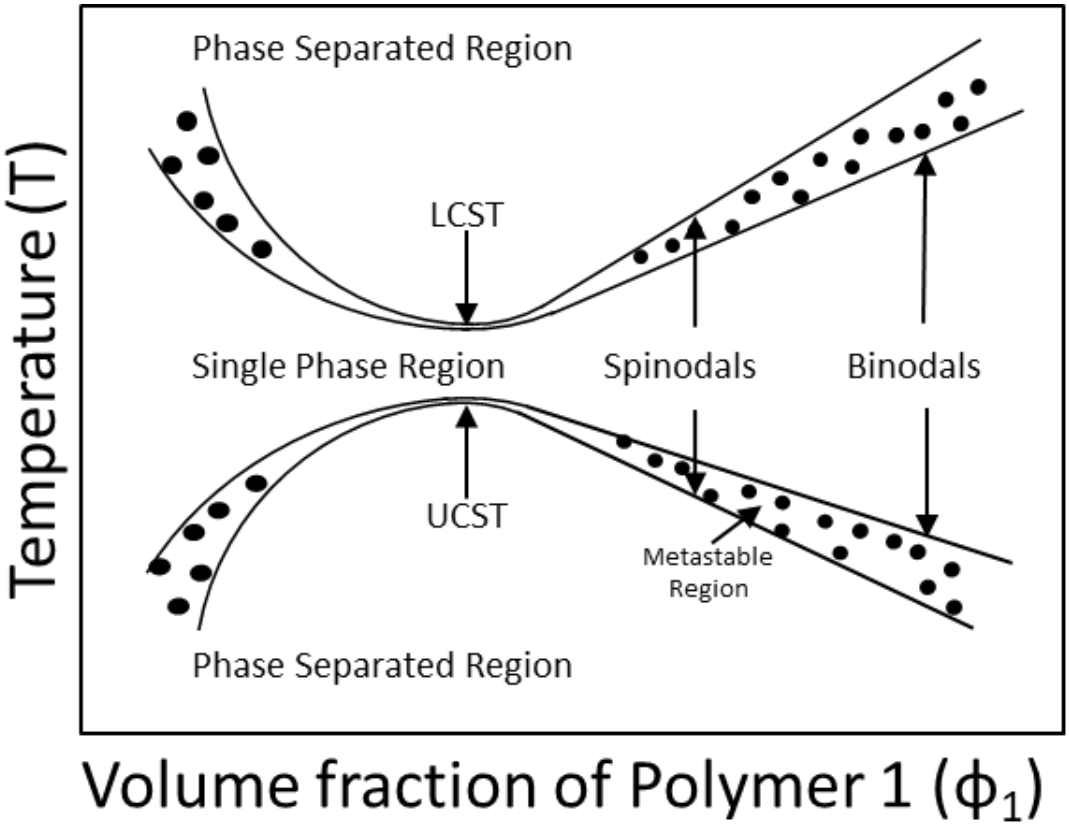


Fig. 1.3. Phase diagram of a two polymer blend system as depicted by the temperature of the mixture and the volume fraction of the polymer components.

and strengthening the biphasic interface to minimize the phase separation. For this purpose, compatibilizer molecules must have the proper enthalpic affinity with both molecular species to sufficiently diffuse throughout the blend and establish entanglements between the segregated phases and stabilize or strengthen the interface between them. For polymer blends, these requirements are translated into the pre-requisite of chain entanglement between the compatibilizer and the individual polymer phases.[34-36] Since entanglements are most likely to occur between polymer chains of sufficient length, and because each polymer in the blend has drastically different thermodynamic and chemical natures, the most common form of compatibilizer used in polymer blending are various forms of copolymer.

Copolymer compatibilizers act much like surfactants, where the interface between the individual phases is modified to increase its surface area whereby the coalescence of minor phase domains is stopped, and the phases maintain a high dispersion. In addition, as copolymer migrates into the interfacial space between the polymer phases, the compatibilizer acts as a boundary to prevent direct contact between said phases and minimize thermodynamically unfavored interactions.[37-39] Numerous experiments have determined that the addition of simple di-block copolymers, for instance, enhances the thermomechanical properties of phase separated polymer blends.[40-42] When the di-block copolymer merges with the biphasic interface, the two copolymer segments with set monomer species sufficiently entangle with chains of their corresponding homopolymer phase to generate a much stronger interface and create a blend material with better properties than without the compatibilizer. Though di-block species are the most simplistic of these compatibilizers, other sequence distributions have been experimentally used to enhance blend characteristics.[43] An illustration depicting some of the different potential copolymer compatibilizer sequence distributions can be seen below as Figure 1.4. By modifying the number of monomer

blocks present within the copolymer, the diffusion and entanglement dynamics between the compatibilizer and the individual homopolymers can be drastically changed. As an attempt to measure the relative blend compatibilization effectiveness based on the copolymer's architecture, Dadmun conducted a series of Monte Carlo simulations and experiments.[34, 44, 45] Cumulatively, the results indicate that the most effective copolymer sequence distribution for blend compatibilization are multi-block copolymers with blocks long enough to generate multiple entanglements with each homopolymer phase.

Reactive Telechelic Oligomers and In Situ Copolymer Compatibilizers

In the generation of polymer blends from melt extrusion, there is a branch of processing that incorporates reactive materials or components into the blend to change the end properties of the product. This method refers to reactive processing and is grouped into several categories depending upon the desired reaction outcomes that occur in situ. These reactions can range from the formation of copolymers with various architectures, the controlled degradation of one or more chemical components in a blend, or even the coupling of reactive functionalities together to form new chemical species. The reactions of interest in this dissertation involve the formation of copolymers from coupling reactions between functional groups located at the end of individual oligomer species dispersed within an incompatible polymer blend. Under the elevated temperatures of the melt extruder, the sufficient dispersion of thermal energy induces covalent bond formations between these "telechelic" species. This reactive process then produces in situ copolymers that then preferentially assemble at the biphasic interface in a similar manner to copolymers added via standard compatibilization practices. An example reaction of telechelics with carboxylic acid and epoxy groups arranging at the biphasic interface to form a copolymer via

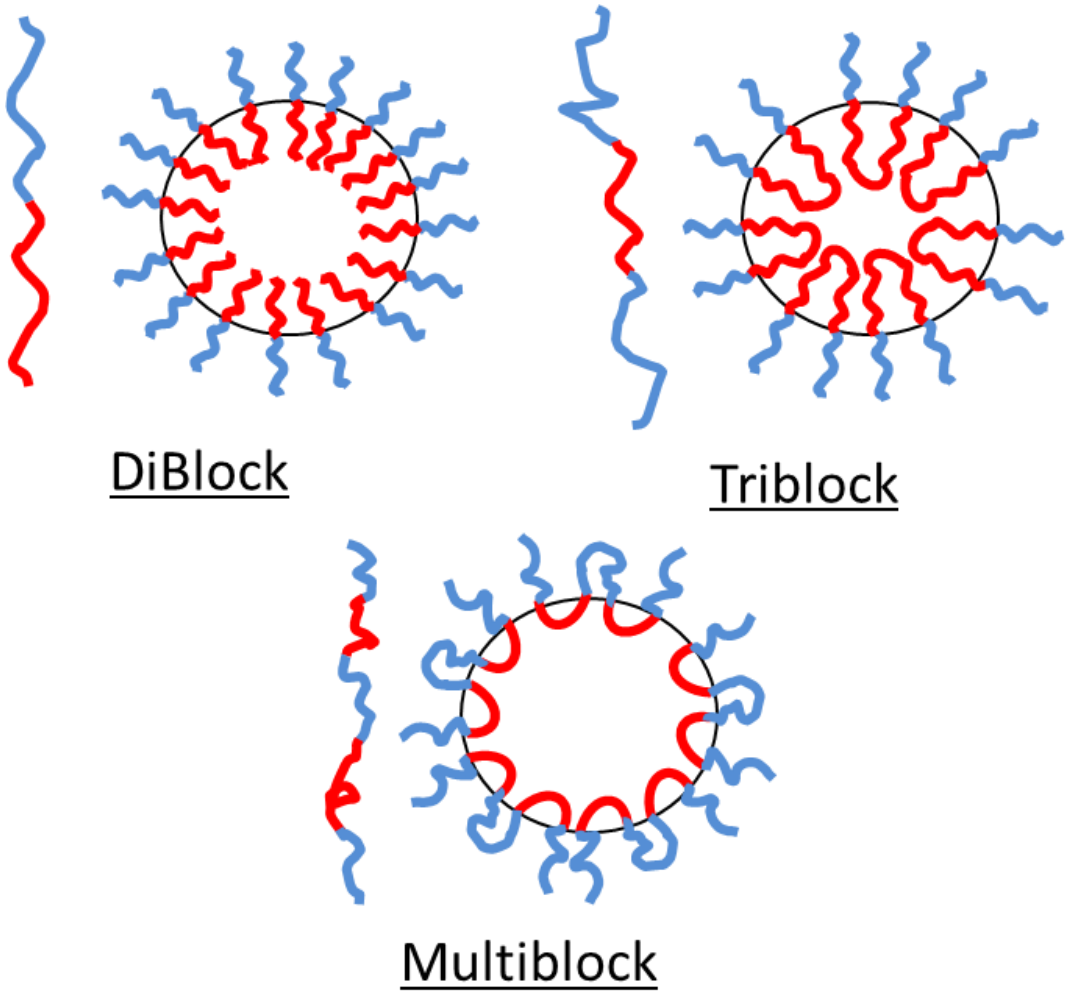


Fig. 1.4. Sequence distributions of various copolymer additives and the resulting biphasic interface architecture following blend compatibilization.

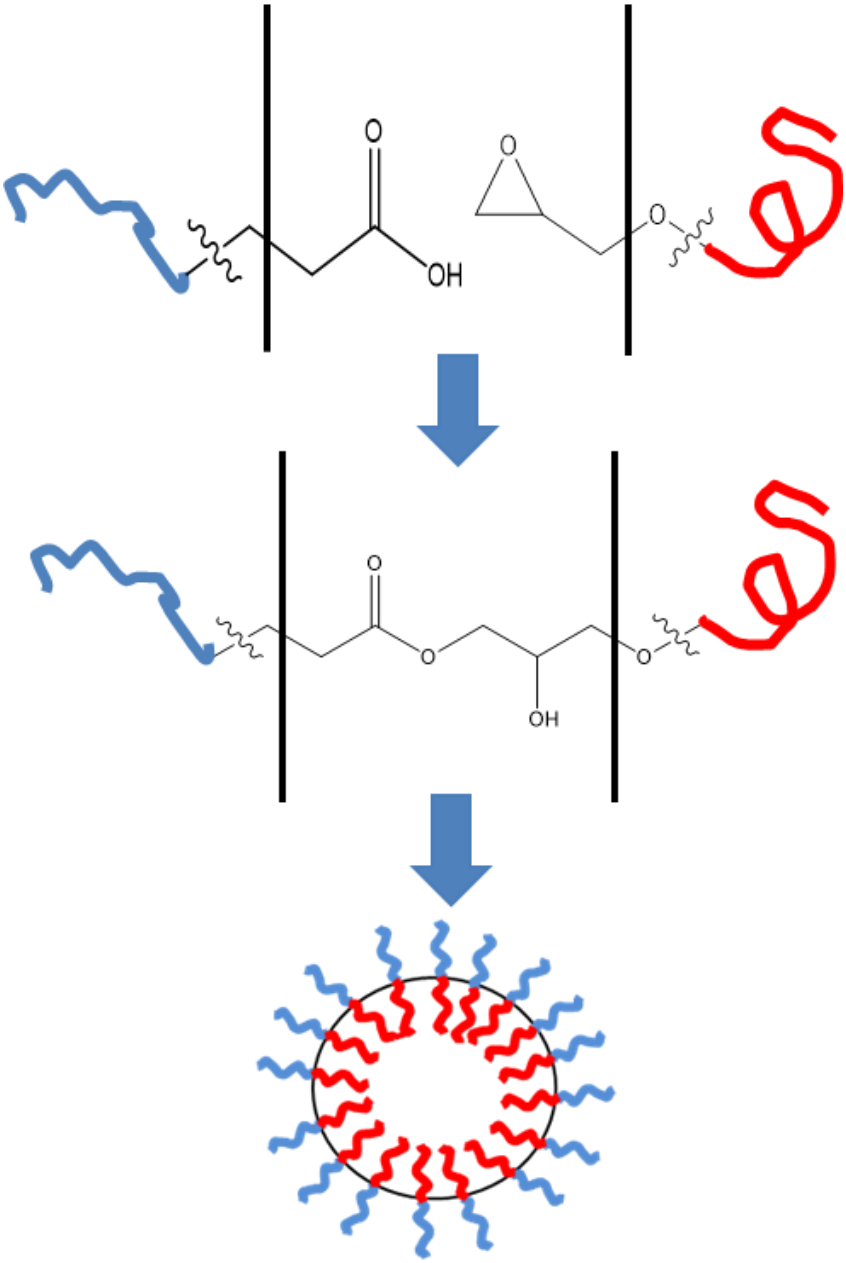


Fig. 1.5. Formation of a blend compatibilizing di-block copolymer from the reaction of carboxylic acid and epoxy telechelic oligomers.

an ester linkage is seen in Figure 1.5. The kinetics associated with this copolymer formation reaction have been analyzed in the literature, primarily by Schulze et al.[46] Blend molecular parameters that have been shown to influence the oligomer reaction kinetics include the complex entanglement behavior between oligomers and the individual homopolymer phases, the relative reactivity of the functional groups, and the existence of a critical coverage of the biphasic interface with increasing oligomer concentration.

Dissertation Outline and Objective

This research dissertation presents numerous findings concerning the molecular and chemical interactions between polymers and nanoscale additives within additive manufacturing and polymer blend compatibilization. Chapter two demonstrates the impact of multi-functional crosslinking agents on the interlayer adhesion and mechanical strength of FFF printed objects, and how the agent's reactivity, molecular structure, and concentration, along with the variable and complex thermal environment within a printer, contribute to these observed improvements in object isotropy. The third chapter correlates the magnitude of irreversible thermal strain ($\boldsymbol{\varepsilon}$) present within a printed PLA object to a physically measured deformation as the result of extensive thermal annealing above the glass transition. Furthermore, correlation of the filament's thermal behavior to the measured strain with deformation reveals that the molecular properties of different nanoscale additives to the filament directly influences the filament's irreversible thermal strain from changes to polymer viscosity and overall intrabead chain assembly. Lastly, in chapter four, the reactive compatibilization of a crystalline polymer blend was analyzed with the use of reactive telechelic oligomers. The results demonstrate a complex relationship and interplay between blend crystallization, blend plasticization, and reactive compatibilization as they influenced by increased loading of telechelic oligomer within the material.

Disclosure Statement: The following chapter, “Interlayer FFF Crosslinking Additives and Rate Analysis of Post-Deposition Reactions” is a direct write up of “Incorporating crosslinks in fused filament fabrication: Molecular insight into post deposition reactions” by the author and Dr. Mark Dadmun, first published by Elsevier in the journal Additive Manufacturing in December of 2020.

This article can be found by the following hyperlink: https://doi.org/10.1016/j.addma.2020.101746

Chapter 2. Interlayer FFF Crosslinking Additives and Rate Analysis of Post-Deposition Reactions

Abstract

3D printed objects suffer from intrinsic mechanical weakness due to low interlayer adhesion and defects that result in anisotropy in their mechanical properties. In this report, we examine the ability of a protocol to incorporate covalent bonds between layers to strengthen interlayer adhesion by depositing multi-amines between layers during the fused filament fabrication printing process. The multi-amines may then react with oxygenated functional groups on the deposited filament to form covalent crosslinks between layers. Determination of the interfacial fracture energy and infrared (IR) spectroscopy studies indicate the successful formation of covalent bonds and strengthening of the interlayer interface with a variety of multi-amines. More importantly, IR results also elucidate the relative rate of reaction of the amines with oxygenated functional groups found on the oxidized filament. These results show that the crosslinking reactions primarily occur shortly after deposition of the filament, i.e. at elevated temperatures. The data also show that the reactivity of the amines is not the prevailing factor in determining interfacial strength, as the aromaticity of the crosslinker plays a key role in creating a stronger interface. These results therefore provide important foundational understanding that can be used to apply this protocol to a variety of extrusion based additive processes and materials.

Introduction

Fused filament fabrication, or FFF, is an additive manufacturing method used in rapid object design and prototyping for thermoplastic materials. Since its conception in the 1980's, the format has expanded to numerous areas including the construction and automotive industries. The ability to generate larger complex objects with minimal waste has driven interest in developing FFF into a reliable and robust manufacturing method. Large-scale printers have been produced and continue to evolve with the goal of advancing the technology to compete with traditional industrial fabrication methods. Structural weakness and anisotropy that emerge from weak layer interfaces and structural defects remain limiting factors in the advancement of polymeric extrusion based additive technologies beyond the maker level. For instance, a car body produced by the Big Area Additive Manufacturing 3D printer exhibited poor interfacial adhesion during the print process. Talagani et al. developed an efficient method to determine problem areas in the print build where interlayer delamination is probable.[47]

The FFF print process begins with a CAD model of the desired structure, which is interpreted by the printer's onboard software to move a hot nozzle in the x and y directions above a heated bed surface.[48] Polymer filament is then extruded onto the heated bed to generate each layer with the nozzle moving upwards after layer completion at a pre-determined height value in the z-dimension and directed to deposit the next layer.[49] This process is repeated continuously for each layer until the object is fabricated. Inferior mechanical integrity of prints is linked to this layered build process, with mechanical strength dependent on direction of the applied force relative to build orientation (Figure 2.1a).[50] This weakening causes structural anisotropy, which is associated with minimal diffusion of thermoplastic between individual layers.[51-54] Moreover, the

bottom portion of prints are subjected to continuous heating from the heated bed with a thermal gradient emerging as the print increases in height along the z-axis. This gradient of thermal energy causes deposited material near the middle and end of prints to cool more rapidly from convection and prevents polymer chains from diffusing across the interlayer boundary to enhance isotropy. Therefore, each layer receives a varying amount of heat from the hot nozzle head as it is built. Cumulatively observed, the print object is subject to a complex thermal history that fluctuates at each layer with respect to the nozzle head, distance from the bed, and the temperature of the print environment (Figure 2.1b).

Previous experiments have focused on modifying physical print parameters to reduce anisotropic weaknesses. Raster mechanics and the resulting tensile property changes with raster width, angle, pattern, and spacing have been analyzed extensively.[55, 56] Other factors, such as layer height and the extrusion, bed, or air temperature have also been found to influence mechanical anisotropy.[48] Any decrease in anisotropy attained in these studies is due to variation in the amount of interfilament diffusion and the size of void spaces between filaments during the build process, but these factors fail to significantly limit anisotropy. Recent research has therefore shifted from altering these physical print parameters in favor of modifying the polymeric filament itself. Alterations of the printed thermoplastic include the inclusion of additives, such as graphene, microdiamond aggregates, or other reactive components to the filament.[20, 27, 53, 57]

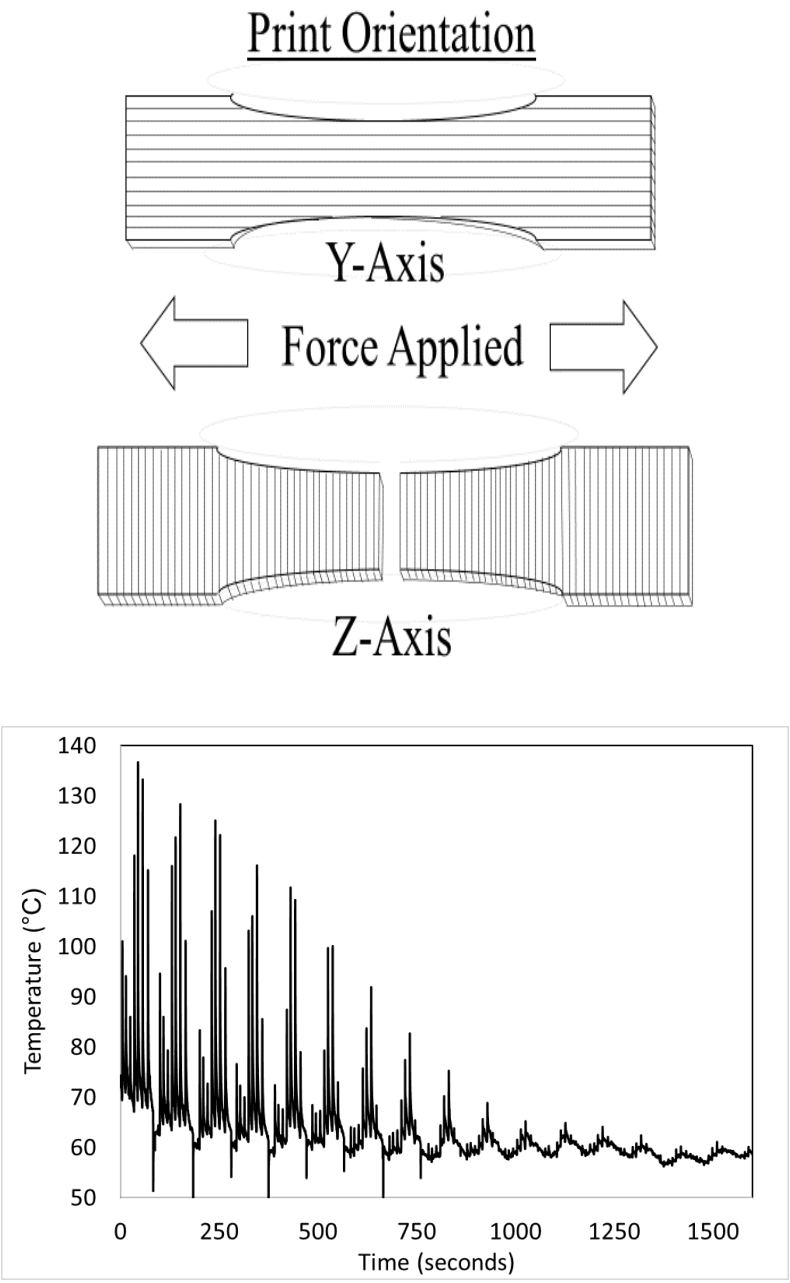


Fig. 2.1 a. Illustration of an FFF object's build orientation and physical response to an increasing uniaxial force. **b.** Thermal history of an individual layer in a sample cube as recorded via thermal camera.

ABS, or Acrylonitrile-Butadiene-Styrene, is a terpolymer and common material used in FFF for prototyping. The composition of the ABS can vary significantly among providers; however, two-thirds of the material usually consists of a styrene-co-acrylonitrile (SAN) copolymer matrix interspersed with polybutadiene (PB) domains. It is well established that, when heated at or above 100 °C in air, ABS oxidizes to form functional groups such as carbonyls, hydroxyls, and epoxides through reaction of butadiene double bonds with atmospheric oxygen.[58-60] In the process of filament creation and extrusion, ABS is consistently subjected to temperatures well above 100 °C, providing pathways to produce these oxidative groups at the surface of a printed object. These functional groups can then react with properly designed co-reactive molecules in deposition processes that are consistent with 3D printing. Moreover, the reaction of multi-functional molecules between filaments may form interlayer covalent bonds, providing a significant increase in interlayer adhesion of the printed object.

Amines are interesting candidates as such crosslinkers, as they readily react with ketones or aldehydes to produce imines.[61] Amines also react with epoxy resin oligomers to produce extensive crosslinks. Thus, in the current study, the formation of interlayer covalent bonds between oxygen containing functional groups on ABS filament that are formed during printing and multi-amines is examined as a rational method to strengthen inter-layer interfaces formed during FFF. The impact of amine structure, loading, and surface temperature on the success of the inter-filament crosslinking reaction are studied from both a mechanical and reactive rate perspective. These results presented below therefore provide insight that can be used to formulate and optimize crosslinking reactions between filaments and open new routes to fabricate more robust and isotropic materials by extrusion-based 3D printing in a scalable fashion.

Experimental

Materials

2.85 mm diameter ABS filament was purchased from Gizmo Dorks. Unmodified polybutadiene (5000 g/mol molecular weight), 4,4'-diaminodiphenyl methane (DADPM), 4,4'-diaminodicyclohexylmethane (DADCM), and pentaethylene hexamine (PEH) were purchased from Sigma-Aldrich and used without further purification. KBr windows were purchased from Pike Technologies. Solutions applied to the 3D printed structures during the printing process were generated by dissolving weight percentages of 5, 10, and 20 % crosslinker into 10 mL of acetone at room temperature. The molecular structure of each crosslinker is shown in Figure 2.2.

Interfacial Adhesion Determination

Interfacial adhesion experiments in this study monitored specific factors that influence the interlayer strength of the samples. Samples prepared using crosslinker solutions with concentrations from 0 to 20 wt% were first examined to illustrate how the interface is strengthened by increasing reactive crosslinker concentration. A second set of samples were examined to elucidate the impact of decreasing available thermal energy for the crosslinking reactions by increasing stop times between layer deposition. Samples tested under these criteria consisted of both unmodified and 5 wt% crosslinker. Lastly, to demonstrate the crosslinker's overall effectiveness on an entire printed structure, the tensile properties of samples printed with crosslinker deposited on every layer were monitored. In these studies, the tensile properties of the printed structure was determined both parallel and perpendicular to the print direction to document the impact of the incorporation of crosslinks on structural anisotropy of the printed parts.

Specimens were created from hollow cubes printed with a Lulzbot Taz 5 printer and ABS filament with diameter of approx. 2.85 mm and a nozzle head of 0.5 mm. Cubes consisted of 176 layers printed at 60 mm/s with a 0.3 mm layer height for a total object height of approx. 53 mm (Figure 2.3a). Print parameters for each cube included 210 °C extrusion temperature and a bed temperature of 110 °C to maintain similar thermal and build history for all samples. Crosslinker solutions were applied to the middle sixteen layers of each cube in a single counter-clockwise motion by soaking cotton swabs in the solution and 'painting' the solution onto the filament. By utilizing this swabbing technique, a thin film of crosslinker solution is delivered to the inter-filament interface. Reproducibility of interfacial adhesion values are consistent indicating a reasonably regular dosage of the crosslinker on each layer. Completed cubes were then cut at each face corner with a Dremel® rotary saw to yield individual plaques. The cube faces were then cut with a laser cutting system to create samples for Instron testing (Figure 2.3b). Shape and dimensions of the dual-cantilever beam samples were derived from previous literature used to test the interlayer strength of FFF objects by isolating the force of separation into a preset "crack" of approximately 3 layers wide that would separate specifically at the modified interface.[62, 63] To establish a statistically relevant adhesion strength for each crosslinker, a minimum of two cubes per solution were generated, which creates eight fracture energy samples. Specimens that examined the influence of print pause time on interlayer adhesion were created by first pausing the print at a layer, applying solution with the same method as other prints, waiting for a set amount of time, and then allowing the print to continue with the next layer. This process was applied to the central three layers in the middle sixteen that received crosslinker solution to allow the pause time to only affect the test interface.

The interfacial strength of each sample was determined with an Instron Model 5567 universal tensile testing device set with a 30 kN load cell. Samples were pulled apart at a rate of 2.1E-3 mm/s until failure at the test interface. Testing rates were kept at a low speed to accurately measure the fracture energy at the crosslinker modified interface and to prevent the unmodified layers of the samples from separating due to rapid onset of mechanical forces. Results generated by this experiment include sample displacement at break and the load at sample failure. This data were then used to calculate the interfacial fracture energy, as discussed in the results section of this study. Specimens that examined the influence of print pause time and the subsequent decrease in layer temperature on interlayer adhesion were created by first pausing the print at a layer, applying solution with the same method as other prints, waiting for a set amount of time, and then allowing the print to continue with the next layer. This process was applied to the central three layers in the middle sixteen that received crosslinker solution to allow the pause time to only affect the test interface. Pause times consisted of 0, 10, and 20 minutes between individual layer deposition. In additional studies of the mechanical properties experiment, a single cube was printed with an application of 10 wt% DADPM solution to every layer and subsequently laser cut into ASTM D638-V standard tensile dogbones with a set oriented parallel to the layer build and another transverse to the layer build. Young's modulus of the samples was then determined for the samples made from neat ABS and with added crosslinker by tensile tests completed at a rate of 1 mm/min.

Infrared Spectroscopy of butadiene oxidation

Polybutadiene was oxidized at 200 °C in open air for ten minutes in 2.5 g batches in a glass petri dish via hot plate. Solutions of oxidized polybutadiene with 10 and 30 weight percent crosslinker were formed in dichloromethane. These mixtures were then drop cast via syringe onto

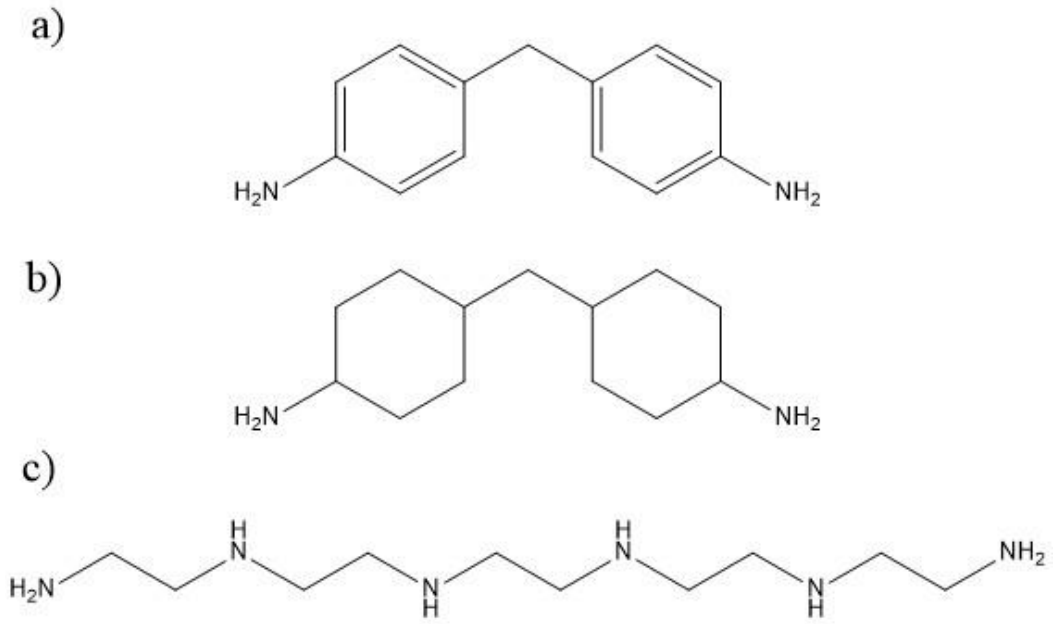


Fig. 2.2. Chemical structures of the crosslinkers used in this study **a.** 4,4-diaminodipheny methane, **b.** 4,4'-diaminodicylohexylmethane, and **c.** pentaethylene hexamine.

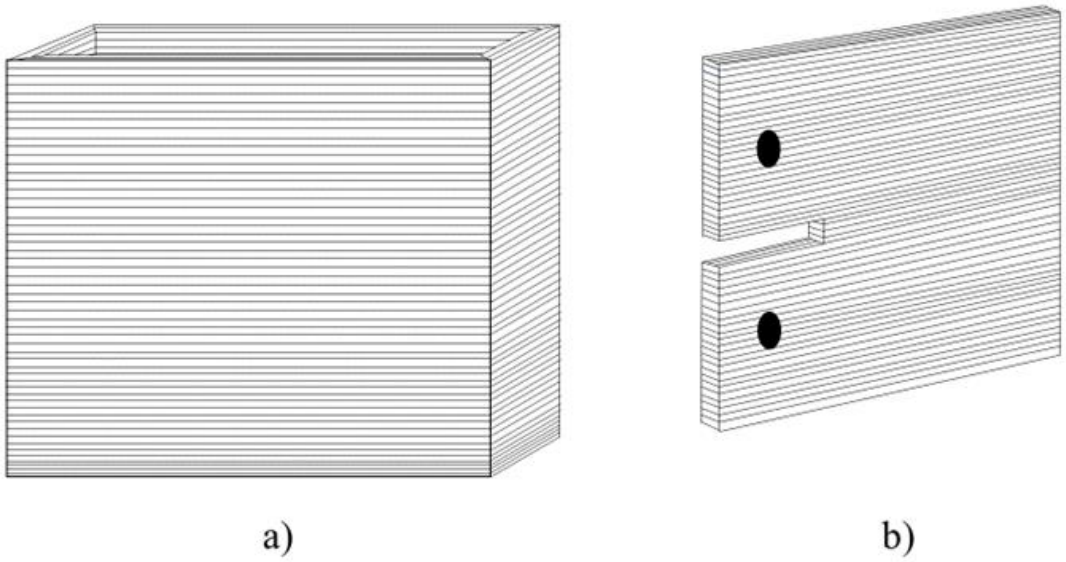


Fig. 2.3. a. Illustration of printed sample cube and **b.** Dual Cantilever beam sample machined from cube.

KBr windows, air dried at room temperature for 30 minutes, and annealed in a vacuum oven at 90 or 110 °C to mimic the thermal environment of a printed layer. Samples were then periodically removed at set time periods and IR spectra were obtained with a Thermo Scientific Nicolet iS50 FT-IR device at 64 scans with 0.4 cm^{-1} resolution.

Results and Discussion

Mechanical Testing and Quantifying Crosslink-Induced Isotropy

The impact of crosslinker addition on interlayer adhesion was determined by measuring the fracture energy of the inter-filament layers using a dual cantilever beam protocol as reported in the literature. Cube samples were printed and cut to fit a custom test geometry (Figure 2.4a). These samples were then loaded on an Instron machine where the force (kN) and displacement (mm) of the specimen monitored. The interfacial fracture energy, *G*, is then determined from Equation 2.1, where P is the load at sample failure, δ is the sample displacement at break, b is the sample thickness (4.5 mm), and A_0 is the initial crack length (15 mm). (Figure 2.4c).

$$G\ (fracture\ energy) = \frac{3P\delta}{2bA_0} \qquad \text{Equation 2.1}$$

Initial fracture energy measurements were completed with neat ABS samples to establish the baseline inter-filament adhesion present in the printed structure. Neat ABS samples failed along the interface with an average fracture energy of ~1.1 kJ/m^2. This value is consistent with results observed for neat ABS tested that is printed by FFF under similar conditions.[64] Crosslinker solutions of varying weight percent were then applied to the interfilament interface to document the ability of any crosslinking reaction to strengthen the inter-layer interface. The strength of the interface was monitored for the addition of 5, 10 and 20 weight percent solutions of crosslinker. The average fracture energy of printed specimens increases with the addition of the crosslinker, and increases with the crosslinker concentration, as shown in Figure 2.5a.

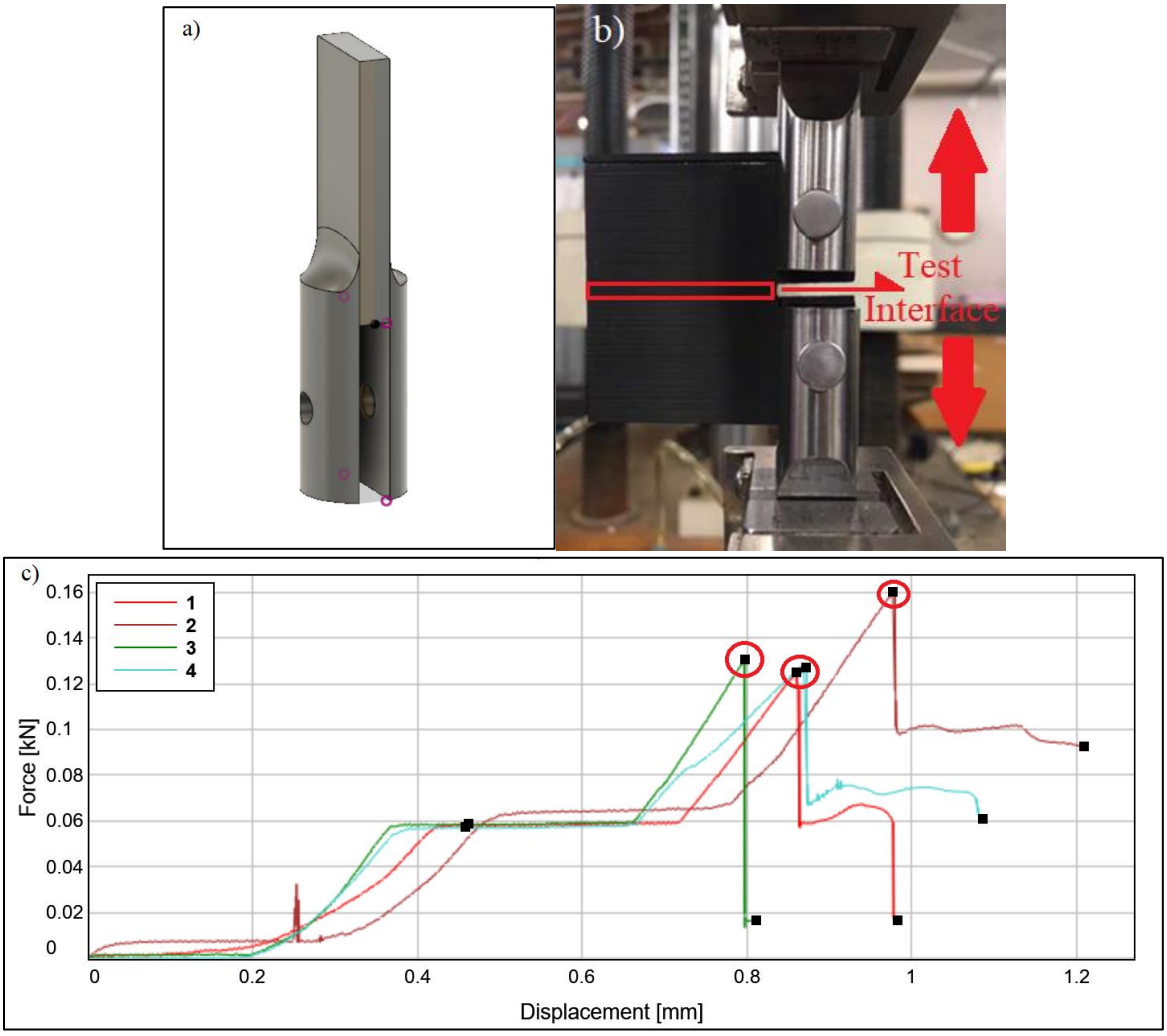
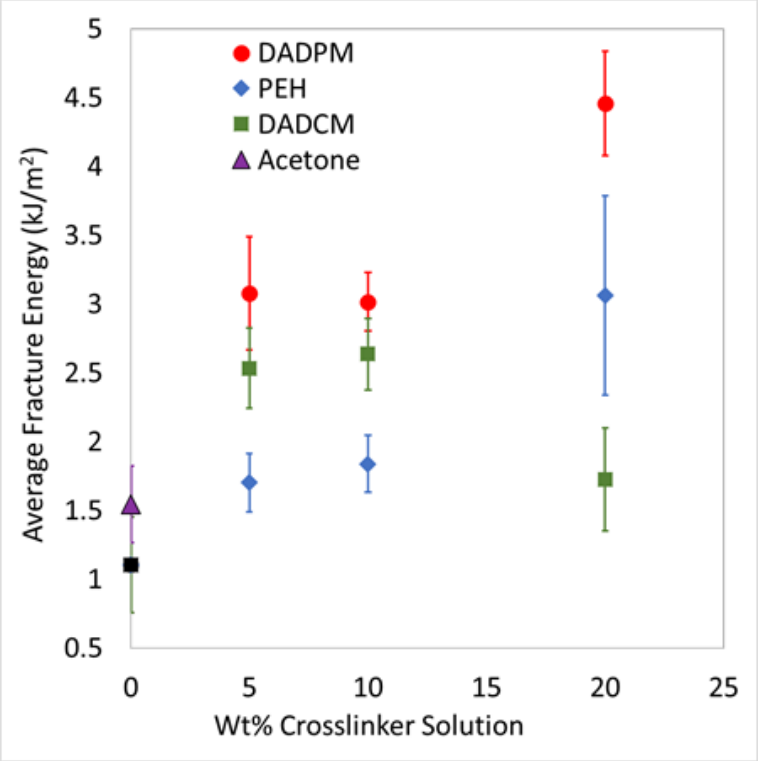


Fig. 2.4 a. 3D model of Instron grips for fracture energy tests **b.** Image of sample tested with Instron and **c.** Typical force vs. displacement curve of fracture energy tests.



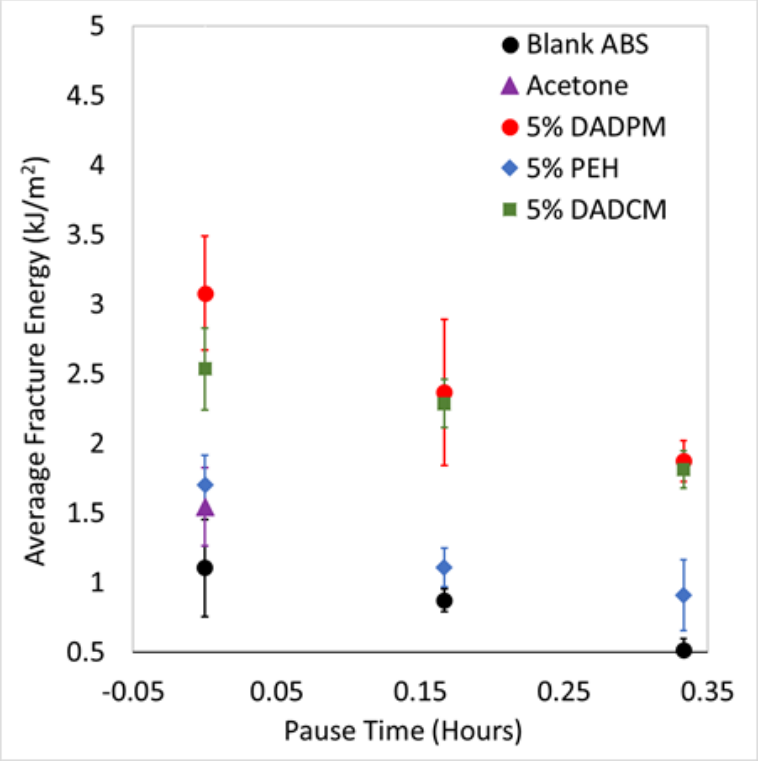


Fig. 2.5. a. Average fracture energy vs. interlayer crosslinker concentration **b.** Interfacial fracture energy as a function of print pause time.

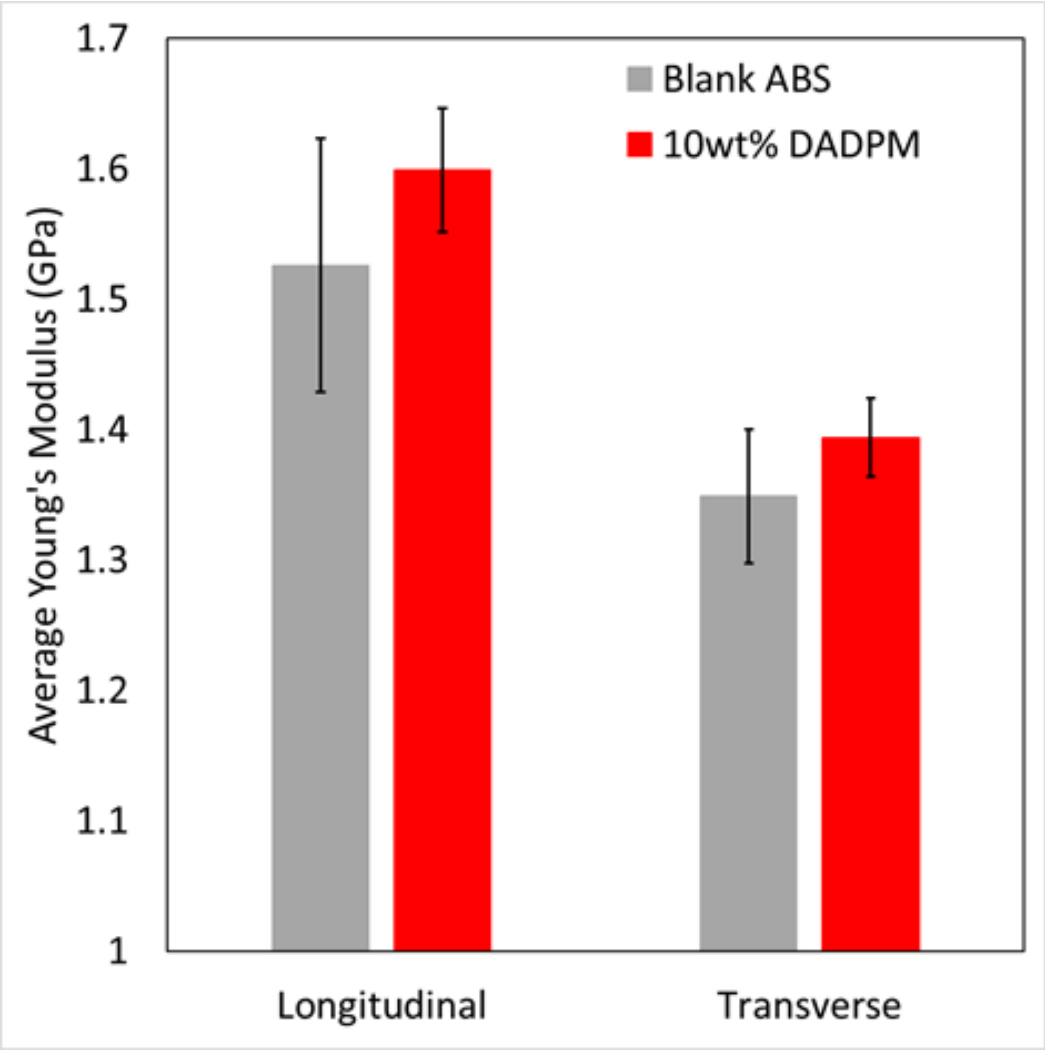


Fig. 2.6. Modulus of printed tensile dogbones with and without crosslinker applied to each layer.

The results in Figure 2.5a show that DADPM strengthens the interface most effectively, with marginal improvement from PEH until higher concentrations while DADCM strengthens the interface at lower loadings but is less effective at 20%. This is further evidenced by Figure 2.6 where the DADPM crosslinking improves the mechanical properties of the sample in both the longitudinal and transverse orientations, increasing the Young's modulus by approximately 7 and 5% respectively. Given that the PEH has five amines available for reaction with oxygenated functionalities, while DADCM and DADPM have two, it is clear that the number of reactive functionalities in the crosslinker molecule is not the most dominant factor impacting the success of crosslinking reactions. The fact that PEH is a less effective crosslinker is surprising as amine chemistry would suggest that PEH may react most readily with oxygenated functional groups due to its sterically unhindered structure, abundance of primary and secondary amines, and higher general nucleophilicity/basicity.[65, 66] The nucleophilicity of the PEH amines is also enhanced by the alkylic structure of the molecule, as opposed to the aryl nature of DADPM that limits its nucleophilicity by the electron-distributing mesomeric effect.

Adhesion Measurements with Varying Print Pause Time

As fused filament fabrication scales up to create larger structures such as cars and houses, the time to build a layer increases. A direct result of this scaling up is that the supporting layer may cool significantly by the time the next layer is deposited, weakening the interface. In order to examine the ability of this protocol to enhance interfacial adhesion on cooled beads, samples were fabricated with deliberate pause times between layers. The impact of incorporating crosslinkers between the paused layers on the interlayer adhesion was then monitored by similar interfacial adhesion measurements. Figure 2.5b. demonstrates the change in fracture energy of the modified interlayer interfaces with print pause time. Longer pause times allow the sample to cool more,

permitting filament to drop below the glass transition temperature, reducing interfilament diffusion and weakening the interface. As the pause time increases, the thermal energy available for the crosslinking reactions also decreases, potentially resulting in a decrease in interfacial adhesion in the crosslinked samples as well. It is interesting to note that the interfacial adhesion of the PEH modified interfaces decreases to values similar to unmodified samples with pause time. This result illustrates, again, that interfacial strengthening reactions are not strongly coupled to crosslinker reactivity. In fact, the DADCM and DADPM modified interfaces maintain fracture energies that surpass the strength of the un-paused, unmodified ABS interface for all pause times.

Reaction Kinetics via Infrared Spectroscopy

The interfacial adhesion results are consistent with the formation of interlayer crosslinks from the reaction of the multi-amine and the oxidized filament. To provide more insight into the impact of crosslinker structure on the kinetics of these reactions, infrared spectroscopy was used to follow the reaction of oxidized polybutadiene (Ox-PB) and the amine crosslinkers to model the reactions that occur in the printing process. Oxidized polybutadiene is chosen as previous studies of ABS oxidation has shown that the formation of oxidative functionalities at elevated temperature are the result of the reaction of the unsaturated moieties of the polybutadiene, and that similar oxidation processes do not occur in pure SAN material.[58, 59] Thus, we expect that the FTIR based reaction results presented will simulate the reactions that occur in the printed part between the amines and oxidative functional groups. The amines may react with a range of oxygenated functionalities. For instance, it is known amines react with hydroxyl groups, where the reactivity increases in proportion to the number and type of hydroxyl functionalities.[67] In more detail, hydroxyl groups that neighbor epoxides may reposition the methylene carbon for more entropically favorable nucleophilic attack from amines, providing one example of how the

oxidation of the butadiene in the ABS filament facilitates the formation of interlayer crosslinks by reaction with amines to strengthen interlayer interfaces as the object is built. By monitoring the direct reactions of the additives with oxidized polybutadiene under thermal conditions that mimic printed filament temperatures, a qualitative understanding of the impact of amine structure and reactivity on the formation of inter-filament crosslinks is obtained that can then guide the choice of crosslinker structure.

In these experiments, solutions of oxidized polybutadiene and each crosslinker at 10 or 30 weight percent in dichloromethane were dropped onto KBr discs. These films were then annealed at 90 or 110 °C for extended periods of time. The choice of annealing temperature was guided by measurements from an infrared camera (FLIR A35sc) that recorded the temperature of a single layer on a sample cube printed under the same conditions as the crosslinked samples. The IR thermal camera was placed within 1-2 ft of the printed sample cube. The temperature of the crosslinked layers were then recorded by the camera (Figure 2.7a) as a function of time with the same conditions as those observed in Figure 2.1b. Temperature measurements begin when a layer is deposited and end when the print was completed. The reported temperature of the crosslinked layers is the time average of the instantaneous temperatures that include temperature elevations due to proximity of the hot extruder during deposition of subsequent layers as shown in Figure 2.1b. Filament temperature averages are then plotted as a function of the print time. These results are shown in Figure 2.7b, which show that the deposited filament starts slightly above 110 °C and then drops to 90 °C in approximately four minutes. Thus, these temperatures mimic the thermal history and monitor the potential reaction during the first few minutes after bead deposition.

Peak assignments associated with crosslinker amine motion were obtained from IR spectra analysis of the pure materials. An in-depth description of DADPM's spectrum and subsequent

peak assignments has been reported in the literature.[68] Two peak pairs in the 3300-3415 cm^{-1} region were designated for the asymmetric and symmetric stretching of the primary amine's hydrogens (Fig. 2.8b). During sample annealing, the reaction progress of the primary amine was monitored from the relative decrease of the intensities of these peaks. Using DADPM peak assignments as a reference, the pure spectrum of DADCM and PEH were also analyzed and curve fitted for their individual amine moieties. Full peak assignments for each species are listed in Table 2.1. Drop-cast IR samples were then annealed at increasing annealing times and monitored for changes in peaks or the creation of new peaks associated with newly formed bonds by reaction of the crosslinker. In the DADPM mixtures, the formation of a secondary amine stretching peak (≈3380 cm^{-1}) was observed beyond two minutes of annealing at 110 °C as seen in Fig. 2.8a. DADCM mixtures generated a similar peak at approximately 3330 cm^{-1} signifying secondary amine creation. The growth of these secondary amine peaks are interpreted to indicate the formation of a crosslink between the amine and the oxidized polybutadiene matrix with annealing time. Further analysis of the time evolution of these peaks is then used to qualitatively monitor the reaction kinetics of the individual crosslinker molecules with oxidized polybutadiene in hopes of providing more insight into the driving forces that guide the interlayer strengthening observed above.

Qualitative Analysis of Reaction Kinetics

Possible reactions that will result in crosslink formation between filaments include the reaction of a primary amine with an oxygenated functional group and the subsequent reaction of a secondary amine to a different oxygenated functional group. Thus, the kinetics of the crosslinking reactions are modeled using equations that account for both these reactions.

$$\boldsymbol{Primary\ Amine\ Depletion} = k_1[PBOx]^x[-NH_2]^y \approx k_1'\,[-NH_2]^y \quad \text{Equation 2.2}$$

$$\boldsymbol{Secondary\ Amine\ Depletion} = k_2[PBOx]^x[-NH]^z \approx k_2'\,[-NH]^z \quad \text{Equation 2.3}$$

$$k'_1 + k'_2 = \boldsymbol{k'}\ (\textbf{Combined Pseudo Rate Constant}) \quad \text{Equation 2.4}$$

$$[PBOx]^x\ (\boldsymbol{Oxidized\ Polybutadiene})$$

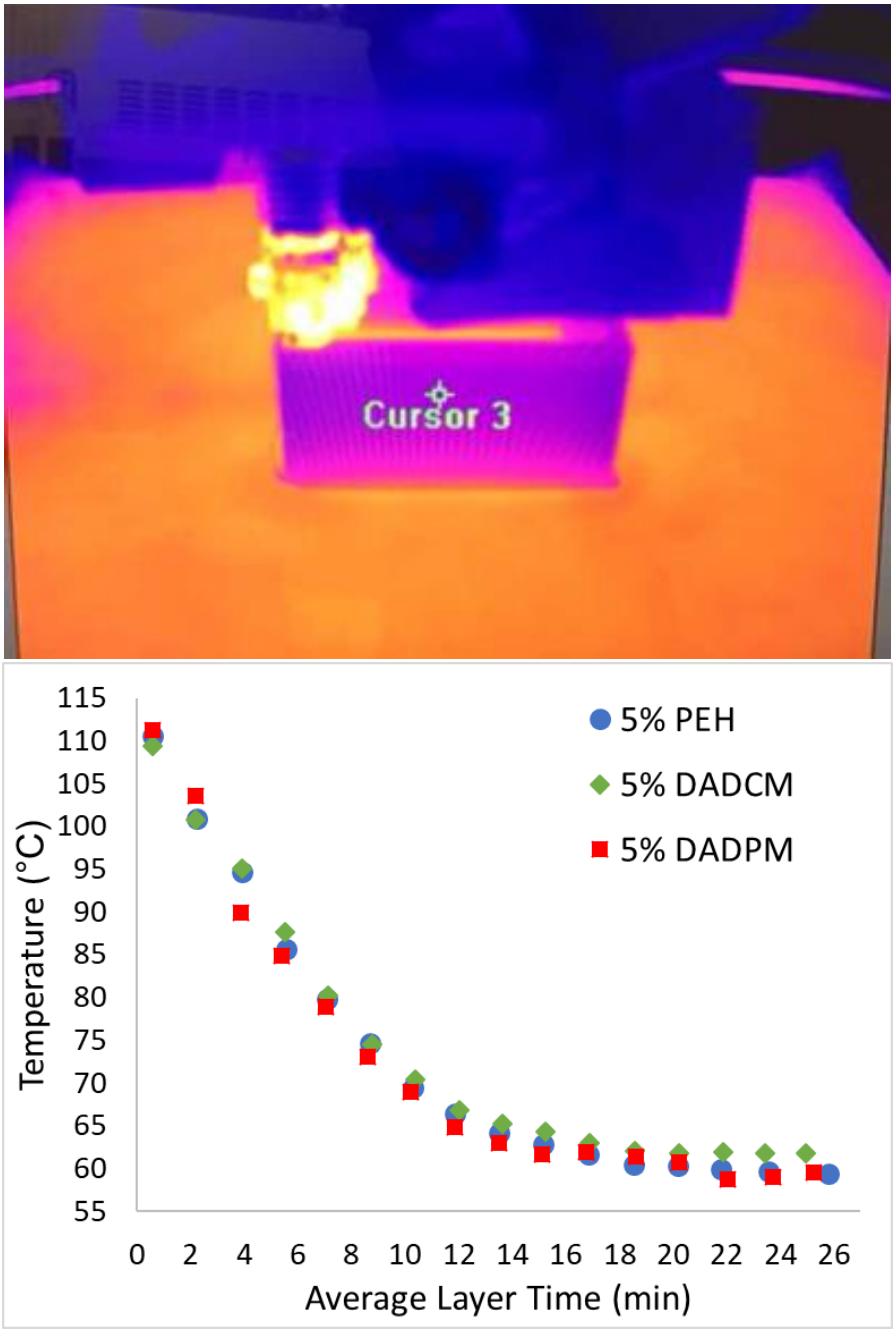


Fig. 2.7. a. Thermal imaging of a cube print, with identification of temperature measurement site (green crosshairs) and **b.** Averaged temperature of the designated layer as a function of the time after layer deposition.

Table 2.1
Infrared signal assignments for Oxidized Polybutadiene and Crosslinker

Species	Wavenumber (cm^{-1})	Assignment
Polybutadiene	3510	Free O-H Stretch
	3430	O-H Stretch H-Bonded to Carbonyl
	3270	O-H Stretch H-Bonded to Hydroxyl
4,4-Methylenedianiline	3444/3414	Asymmetric NH_2 Stretch
	3380	Secondary Amine Stretch
	3336/3317	Symmetric NH_2 Stretch
	3208	Aromatic C-H Stretch
Pentaethylene Hexamine	3359	Primary Amine Stretch
	3293	Secondary Amine Stretch
4,4'-Diaminodicyclohexylmethane	3348	Asymmetric NH_2 Stretch
	3290	Symmetric NH_2 Stretch

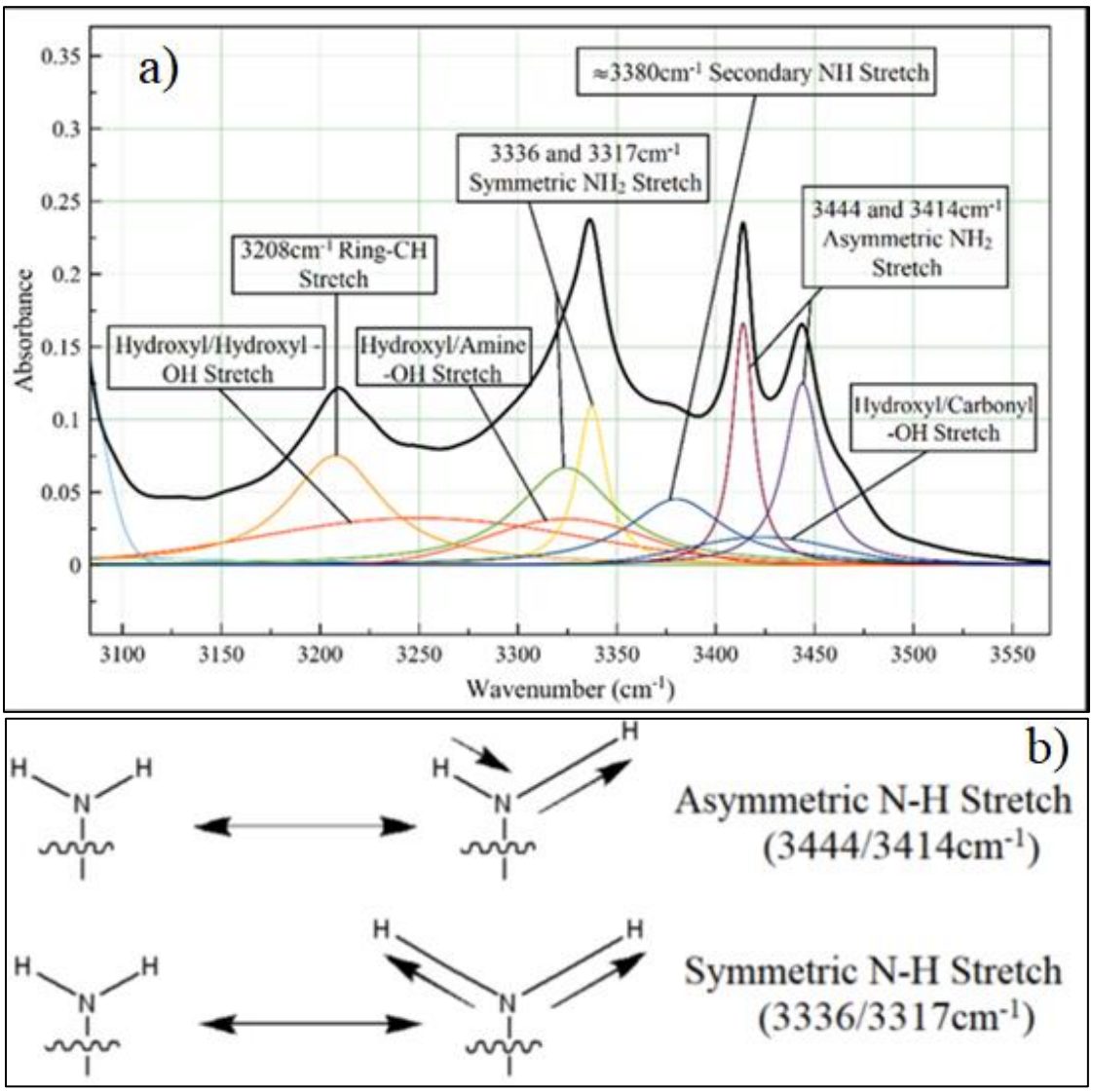


Fig. 2.8. a. Infrared spectra analysis and peak assignment for an oxidized polybutadiene/DADPM mixture and **b.** Atomic stretching and signal assignment of DADPM's primary amine.

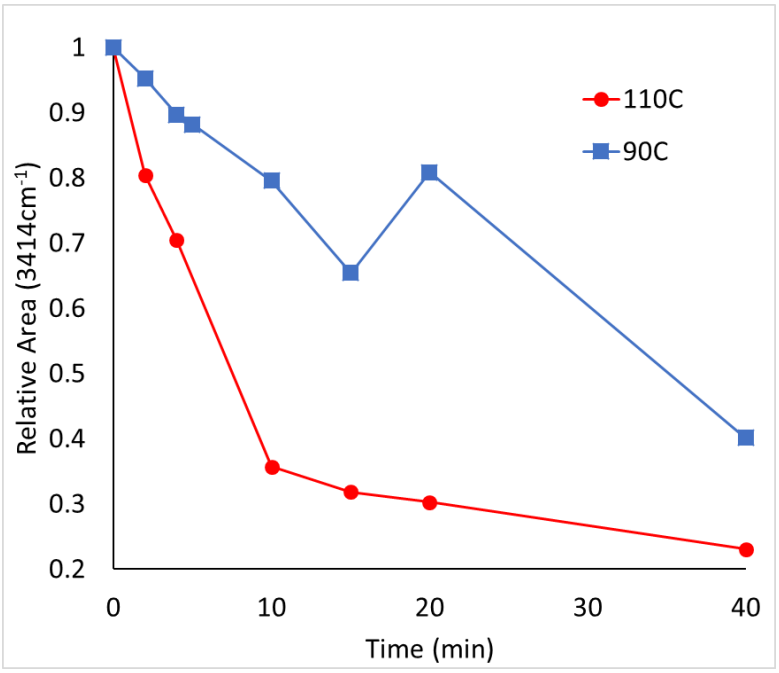
Though the exact amount of oxidative functional groups present in the polybutadiene is unknown, it is assumed to be relatively constant for a given oxidation process, and is thus combined with the reaction rate constant k_1 (k_2) to create a pseudo rate constant k_1' (k_2'). The area under the curve of the relevant peaks were then plotted as a function of annealing time. To monitor the reaction of primary amines, the asymmetric amine stretching modes designated by 3414 cm^{-1} (DADPM), 3348 cm^{-1} (DADCM), and 3359 cm^{-1} (PEH) were monitored. In the analysis of the infrared spectra, the pair of asymmetric amine signals were found to be consistently distinct from one another, allowing for a more reliable peak fit to monitor the reaction. Similar designations of secondary amine stretches; 3375 cm^{-1} (DADPM), 3330 cm^{-1} (DADCM), and 3293 cm^{-1} (PEH) were used to follow the reaction of secondary amines. Peak normalization was conducted by dividing the individual peak areas at given reaction times by the initial peak area prior to the heating.

Figure 2.9 shows the change in the amount of primary (2.9a) and secondary (2.9b) amines in the oxidized polybutadiene and 10% DADPM films with reaction time that are annealed at 90 °C and 110 °C. Figure 2.9a shows that the loss of primary amine in the reaction of DADPM and oxidized polybutadiene reaches steady state after approximately 5-10 minutes when annealed at 110 °C. However, annealing at 90 °C does not attain a steady state primary amine concentration even after 40 minutes. Inspection of Figure 2.9b shows that the concentration of secondary amines grows at early times, which is coincident with the loss of primary amine. The amount of secondary amine decreases as well at longer times, signifying the further reaction of the secondary amines with the oxidized polybutadiene until the primary amines are fully converted at around 40 minutes. The pseudo rate constant, k_1', for this primary amine reaction is then determined by taking an average slope of the data below 10 minutes (i.e. before steady state) for the data at 110 °C and for

the whole annealing time for the data at 90 °C. Similarly, the loss of secondary amine from 10 to 40 minutes for the sample annealed at 110 °C provides the pseudo rate constant k_2'. k_1' and k_2' can then be added to offer a qualitative total rate constant of the reaction ($k' = k_1' + k_2'$) between a given amine with oxidized polybutadiene. Figure 2.10 shows the same change in amine concentration with annealing time for the oxidized polybutadiene and 30% DADPM films, while Figure 2.11 shows the time evolution of the amine concentrations for the reaction of DADCM with oxidized polybutadiene and Figure 2.12 provides the same evolution of the reaction of PEH with oxidized polybutadiene. The pseudo rate constants k_1', k_2', and k' for these reactions are also derived from these plots as described above.

It is important to emphasize that these rate constants are only meant to provide insight into the relative reactivity of DADPM, DADCM, and PEH with oxidized polybutadiene. This analysis monitors the relative reactiveness of each crosslinker solely during the high temperature portions of a layer's thermal history (90-110 ºC). Thus, the clearly qualitative nature of the analysis provides insight into the underlying factors that control the relative rate of formation of crosslinks in the proposed 3D printing protocol only for these potential crosslinkers.

Figure 2.13 shows the change in k_1' and k_2' (2.13a) as well as k' (2.13b) for DADPM at 10% and 30% loading and both annealing temperatures. This data quantifies the extent to which the reaction of the primary amine is (significantly) faster than the secondary amine reaction rate, verifying that the reaction of the primary amine dominates the success of the crosslinking reactions. This data also quantifies how much faster the reaction of DADPM with oxidized polybutadiene is at 110 °C than at 90 °C and how changing the DADPM concentration impacts the



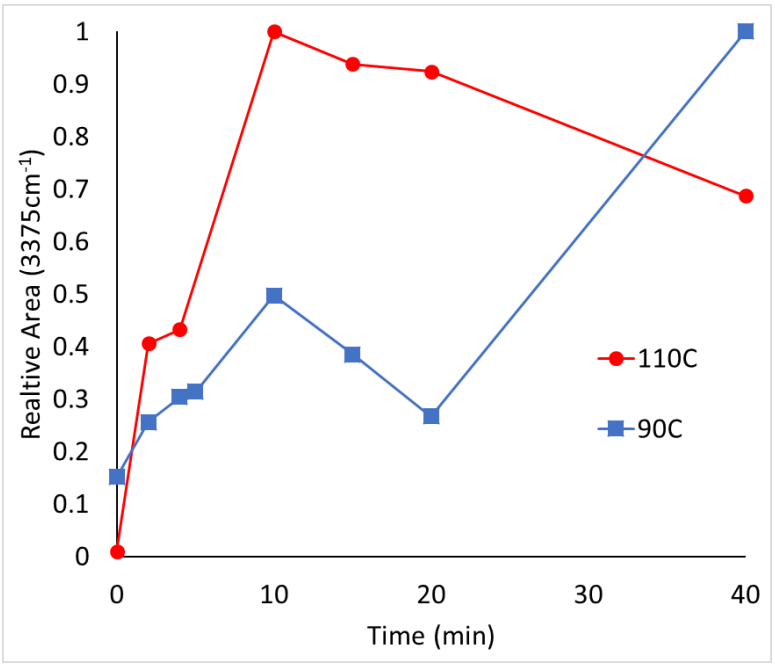


Fig. 2.9. a. Relative peak area of primary amines and **b.** Secondary amines as a function of annealing time for 10 wt% DADPM and oxidized PB.

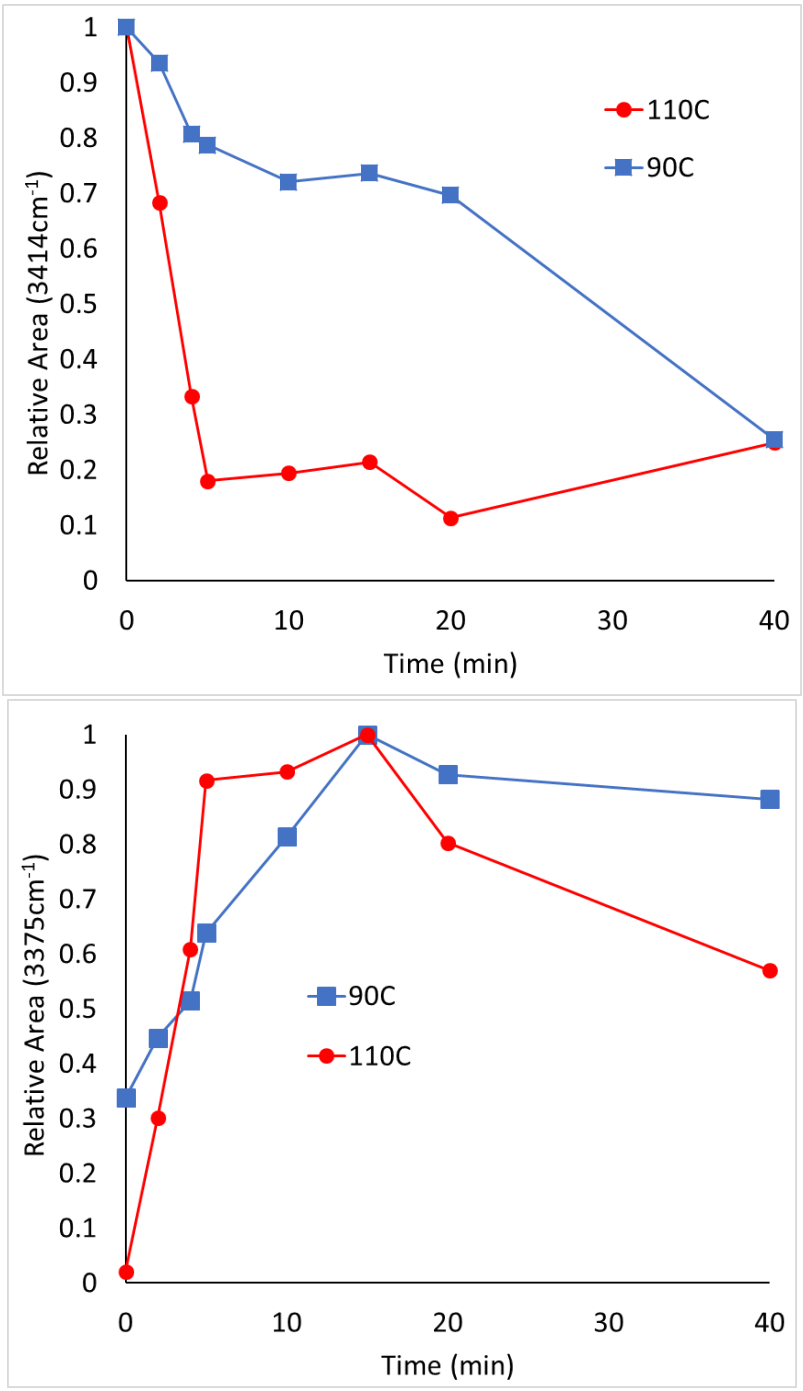


Fig. 2.10. a. Relative peak area of primary amines and **b.** Secondary amines as a function of annealing time for 30 wt% DADPM and oxidized PB.

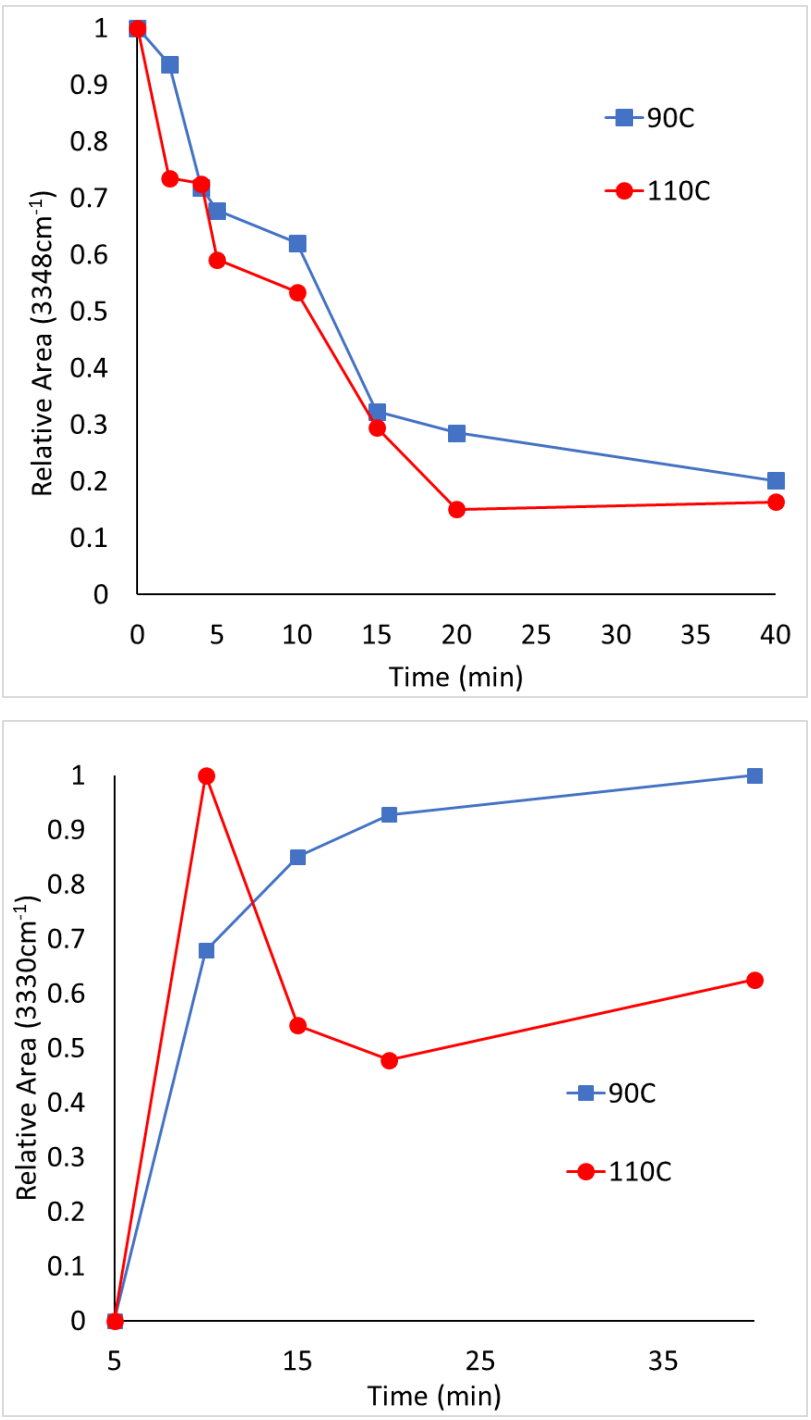
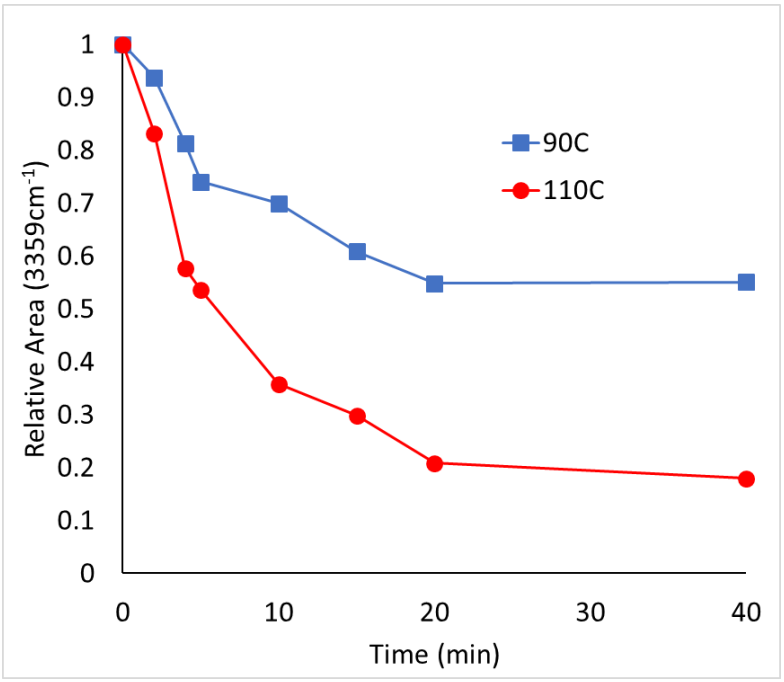


Fig. 2.11. a. Relative peak area of primary amines and **b.** Secondary amines as a function of annealing time for 10 wt% DADCM and oxidized PB.



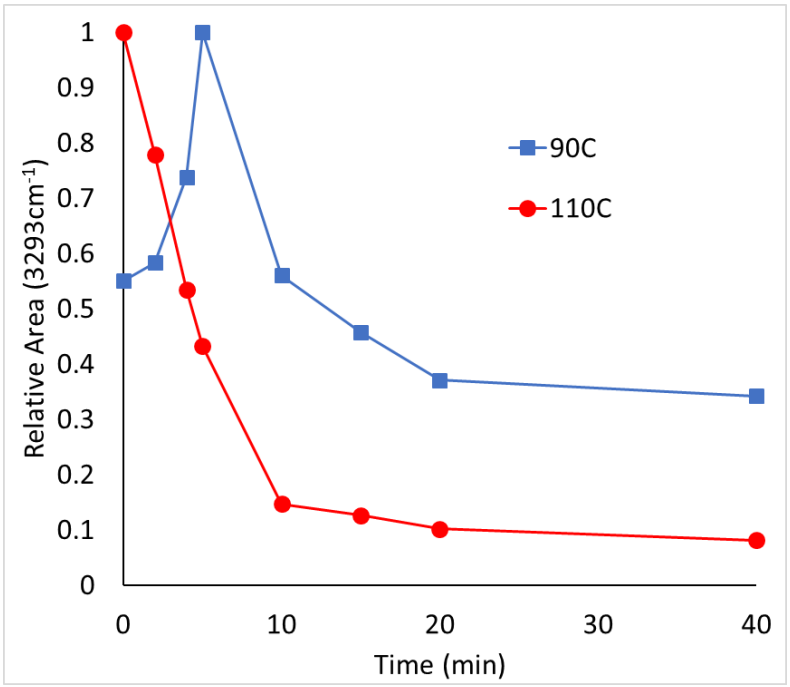


Fig. 2.12. a. Relative peak area of primary amines and **b.** Secondary amines as a function of annealing time for 10 wt% PEH and oxidized PB.

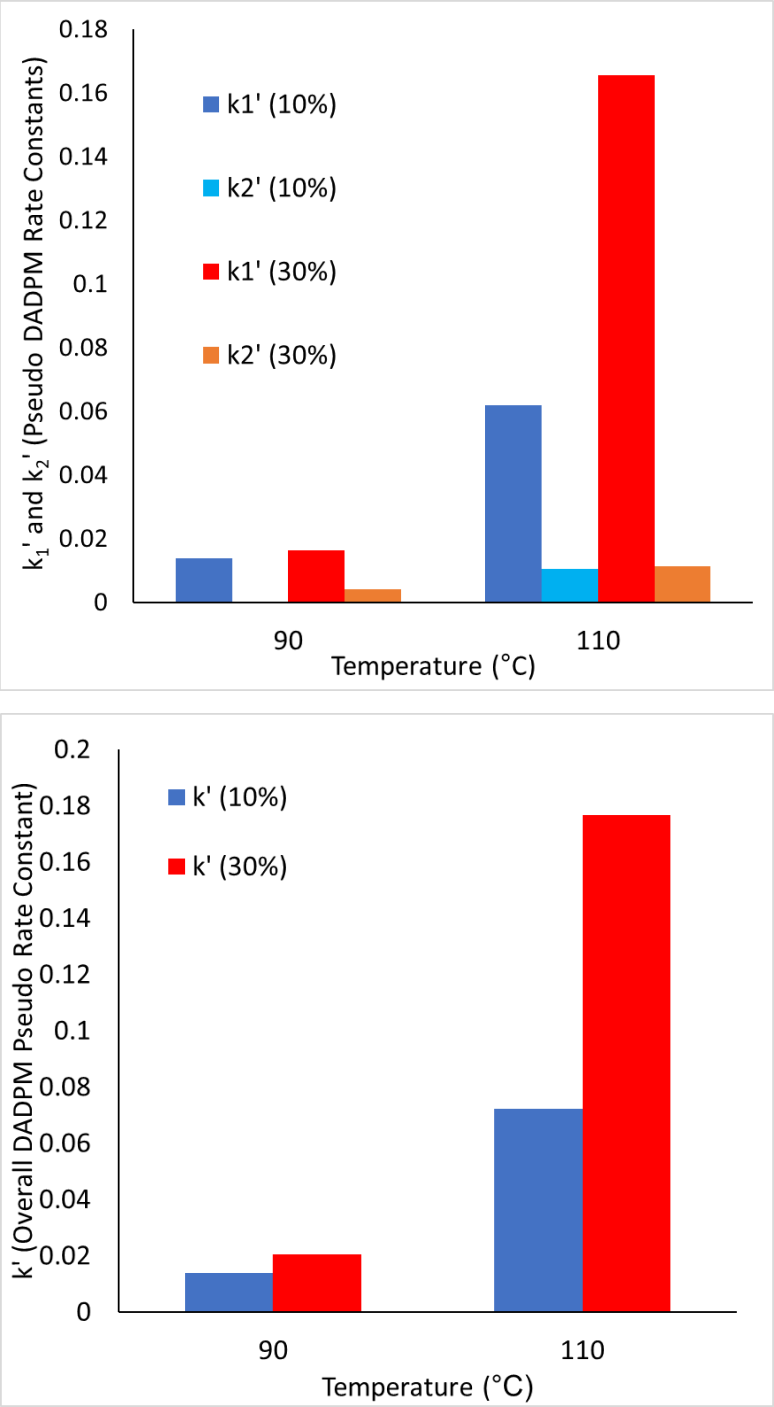


Fig. 2.13. a. Primary (k_1') and secondary (k_2') DADPM amine rate constants and **b.** Combined (k') DADPM reaction rate constants at different annealing temperatures.

reaction rate. Clearly most of the reaction between DADPM and oxidized polybutadiene occurs at elevated temperature, is between the primary amine and oxygenated functionalities, and is more efficient with higher amine loading.

Similar behavior is found for the reaction of DADCM and PEH with oxidized polybutadiene, except that the rate of reaction of DADCM with Ox-PB is less dependent on temperature. Figure 2.14 shows the pseudo rate constants of the primary amine reactions with Ox-PB (Fig. 2.14a), the reactions of the secondary amines with Ox-PB (Fig. 2.14b) and the overall reaction rate constants (Fig. 2.14c) for 10% amine loading. Inspection of these values leads to the interpretation that the reaction of the DADPM primary amine at 110 °C is significantly faster than other reactions, but that the reactions of DADCM is less dependent on temperature than that of PEH or DADPM. The reaction of the secondary amines of PEH with Ox-PB are more prevalent than in DADCM or DADPM, presumably because the PEH contains secondary amines in its structure, and thus is more available for reaction. These results are in general agreement with the general reactivity of aliphatic, cycloaliphatic, and aromatic amines as curing agents in epoxy thermosets. It is well known that primary amines react more rapidly with epoxy functionalities than secondary amines which matches well with the results of Figure 2.14.[69, 70] The primary amine reaction rate constant (k_1') of both DADPM and DADCM are consistently higher than the secondary reaction rate constant (k_2').

Correlation of these results to the interfacial fracture energy (Figure 2.5) leads to some interesting insights. Reaction of DADPM with the oxidized polybutadiene in the printed structure yield the strongest inter-layer adhesion, with DADCM exhibiting the next strongest at low amine loadings, and PEH providing significant interlayer strength at the highest loading. Combining knowledge of the interlayer thermal history during printing (Figure 2.7b) and the relative amine

reactivity with Ox-PB, we conclude that the amine-Ox-PB reactions occur in the first few minutes of the print process at elevated temperature. This is the condition where the DADPM reaction dominates over that of the other two amines. If the reaction between amine and Ox-PB occurred at lower temperature or the reaction of the secondary amines also significantly contributed to the interfacial strengthening, DADCM or PEH would show stronger interfaces. The fact that PEH shows significant strengthening of the interface at high loading suggests that the reaction of the secondary amine can become important at higher loadings.

These results also indicate that the inherent reactivity of the amine with the Ox-PB is not the dominant factor that controls the strength of the crosslinked interlayer interface. From amine chemistry, one would expect that the aliphatic amines would react more readily than their aromatic counter-parts, but it appears that the aromaticity of the amine conveys significant mechanical strength to the crosslinked interfaces. This observation is consistent with the use of these multi-amines as epoxy curing agents, where they react with epoxides to generate intermolecular crosslinks in a thermoset. Review of the epoxy literature documents how amine curing agents enhance the mechanical, thermal, and chemical resistance of epoxy thermosets, where aromatic structures provide thermosets with increased strength but require higher curing temperatures.[71, 72] The need for higher reaction temperatures is consistent with the qualitative kinetics in Figure 2.14, where DADPM reacts more readily at 110 °C. In an epoxy thermoset, cycloaliphatic amines also generate thermal resistance and strength with lower toxicity than aromatic compounds.[73] Although the physical improvements are less than with aromatic amines, cycloaliphatic amines are amongst the most used curing agents as they compromise higher reactivity than aromatics and more robust mechanical properties than aliphatic amines. This compromise is mirrored in the results of Figure 2.14a, where DADCM maintains primary amine reactivity under both annealing conditions while

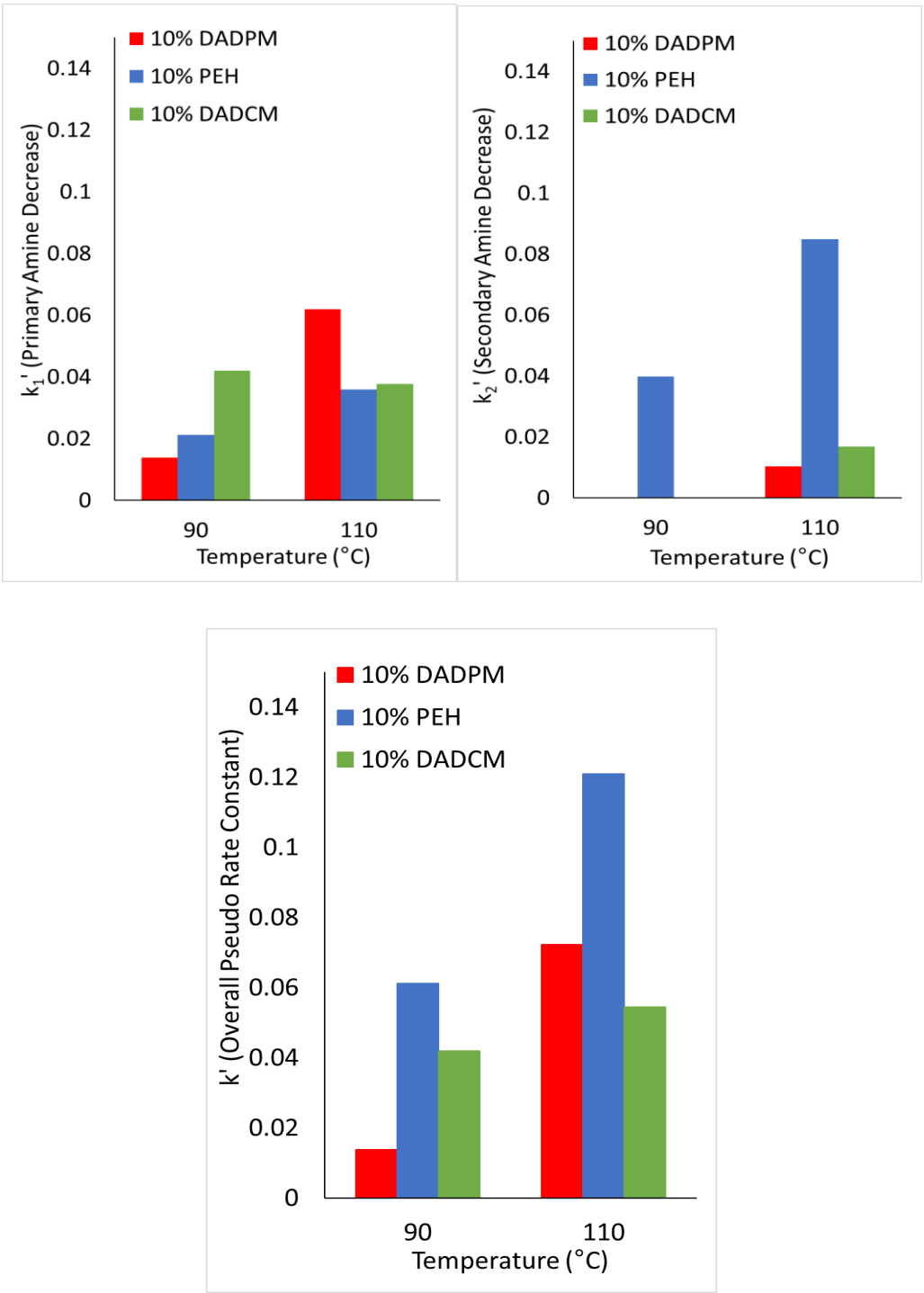


Fig. 2.14. a. Primary amine (k_1'), **b.** Secondary amine (k_2'), and **c.** Cumulative (k') pseudo depletion rate constants for each crosslinker species at set anneal temperatures.

generating consistent interfacial strengthening even when the available heat for the reaction is reduced with print pausing (Fig. 2.7b). Thus, the results above are consistent with the incorporation of aromatic and cycloaliphatic amines into epoxy resins suitable for more robust applications where mechanical strength is important, as the DADPM and DADCM form the most robust interfaces, particularly at lower amine loadings.

These results therefore indicate that the use of cycloaliphatic or aromatic crosslinking molecules at the interfilament interface provides optimal interfacial strengthening and reactivity that can mitigate structural anisotropy in 3D printed structures. The placement of the crosslinking molecules can be implemented immediately before the deposition of a filament, providing a pathway to utilize available thermal energy of the melted bead for the inter-filament reaction. Moreover, this protocol is scalable and readily implemented in most extrusion-based geometries, providing a novel addition to the polymeric 3D printing toolbox that will benefit the growth of 3D printing towards real world manufacturing technologies.

Conclusion

These results document a protocol to form covalent bonds between layers in fused filament fabrication printing. Multi-amines deposited between layers in an ABS cube fabricated by FFF during deposition exhibit interlayer interfaces with substantially improved interlayer fracture energy. This strengthening of the interlayer interfaces is attributed to the reaction of the amines with oxygenated functional groups that form by the oxidation of the ABS filament interface during the printing process. The extent of strengthening of the interface is correlated to the relative reactivity of various multi-amines with oxidized polybutadiene as determined by IR spectroscopy. This correlation indicates that the crosslinking reactions dominate at elevated temperature and thus occur quickly after a filament is deposited. Additional insight indicates that the reactivity of the

amine is not the principal factor controlling the strengthening of the interface, rather the aromaticity or cyclic structure of the crosslinker appears to be an important factor in creating robust interfaces. Higher loadings of crosslinker also improve interlayer fracture energy. These results therefore provide an underpinning for expanding this protocol to a broad range of materials and processes in extrusion based additive manufacturing.

Chapter 3. Nanoscale Additives and Irreversible Thermal Strain in Fused Filament Fabrication

Abstract

3D printing with Fused Filament Fabrication (FFF) is a production method that can potentially evolve to be suitable for large-scale manufacturing. One issue in scaling up the printing process is irreversible thermal strain caused by the layer-by-layer printing process. To evaluate the impact of nanoscale additives on irreversible thermal strain ($\boldsymbol{\varepsilon}$), 3D printed poly(lactic acid) (PLA) monoliths were annealed and monitored for changes in sample geometry. Samples with graphene and low molecular weight (LMW) 3-arm star PLA additives exhibit higher relative $\boldsymbol{\varepsilon}$ compared to samples printed from unmodified PLA. Accounting for the contribution of void space of the printed object to the measured strain, $\boldsymbol{\varepsilon}$, generates a more accurate measure of the strain that occurs within the filament, $\boldsymbol{\varepsilon_z^*}$. Evaluation of $\boldsymbol{\varepsilon_z^*}$ indicates incorporation of the LMW PLA into the filament increases the irreversible thermal strain in the printed object, while samples with pure PLA or the graphene blend maintain similar strain. By correlating the enthalpy of an experimentally observed endotherm near the glass transition to the release of strain ($\boldsymbol{\varepsilon}$), a connection between the molecular relaxation in the printed filament chains to the macroscopic dimensional changes in the various filament constructs is provided. Our interpretation of these relationships is that the addition of bulky graphene sheets increases filament viscosity and confines the polymer chain, which slows the chain relaxation. These nanoscale changes, along with increased thermal conductivity that creates a more homogeneous filament thermal history, appears to minimize irreversible thermal strain build up in these samples. The addition of LMW PLA to the filament has the opposite effect, where a lower filament viscosity appears to increase chain alignment and lead to an increase in macroscopic strain release. Cumulatively, our results demonstrate a relationship between filament viscosity, thermal conductivity, and the resulting

irreversible thermal strain that provides insight to rationally incorporate nanoscale additives to mitigate warpage in the printed part.

Introduction

Fused filament fabrication (FFF) is an additive manufacturing (AM) technique that is expanding from rapid object design and prototyping to robust product generation. A consistent issue for FFF and other layered deposition techniques is the accumulation of residual stresses during printing.[74-78] This buildup of residual stresses within a printed structure is a direct result of the cyclical thermal history of the structure during the deposition process. An FFF print consists of heating a polymer filament above its melting temperature in the extruder head, whereby the semi-molten material is deposited onto a heated surface as beads in two-dimensional layers as directed by the printer computer. With the completion of each layer, the printer moves the hot nozzle upwards a specific pre-determined height and deposits each subsequent layer until the object is completed. Throughout extrusion, molten FFF filament is subjected to shear stresses that may deform the polymer, where this molecular level deformation may be trapped in the printed structure as the deposited bead cools to the glassy state. When the cooled bead is subsequently raised above the glass transition (T_g), the polymer chains may rearrange towards thermodynamically stable states, however this occurs heterogeneously throughout the sample due to the complex and periodic thermal history of the print process. The generation of residual stress, then, is from variation in the thermal history of filament in the cooled, glassy state and the molten polymer being deposited as subsequent layers. This results in uneven distributions of residual stress throughout the layer-by-layer build process. Release of this uneven distribution of residual stress then manifests macroscopically as structural warpage, delamination, or cracking via irreversible thermal strain. Figure 3.1 illustrates this process by which the deformation and vitrification of deposited beads may subsequently contract when irreversible thermal strain is released.

Multiple factors may influence the irreversible thermal strain within a 3D printed object. These factors include build parameters, the printer and working thermal environments, and filament material characteristics. The impact of build conditions on print irreversible thermal strain and residual stress have been studied, including the raster angle, layer thickness, and nozzle speed, and have led to reduction in irreversible thermal strain in 3D printed objects.[24-26, 79-81] For instance, Kantaros and Karalekas demonstrated that the raster angle has a direct influence on the degree of residual stress in a print, with a 0º raster direction having consistently lower residual stresses and strains compared to 90º and 45º degree orientations. In addition, the effect of raster orientation on the observed residual strain was lower when the individual layer thickness was doubled from 0.25 mm to 0.5 mm. Peterson et al. conducted a similar study that determined the effect of layer thickness on irreversible thermal strain relief by monitoring the change in the size of printed samples as a function of annealing time above T_g.[75] By controlling the print layer thickness, it is possible to design 3D printed objects with targeted dimensional changes with annealing or to minimize the observed strain release.

Publications by our group show that using nanoscale additives such as low molecular weight (LMW) PLA and graphene additives reduces mechanical anisotropy of PLA structures fabricated by FFF. Levenhagen et al. showed that the addition of LMW PLA additives to PLA FFF filament improves the interdiffusion of polymer between layers during the print process, which in turn strengthens the interlayer interface and reduces anisotropy.[53, 82] The stronger interlayer interface creates a higher mechanical strength of the print when force is applied perpendicular to

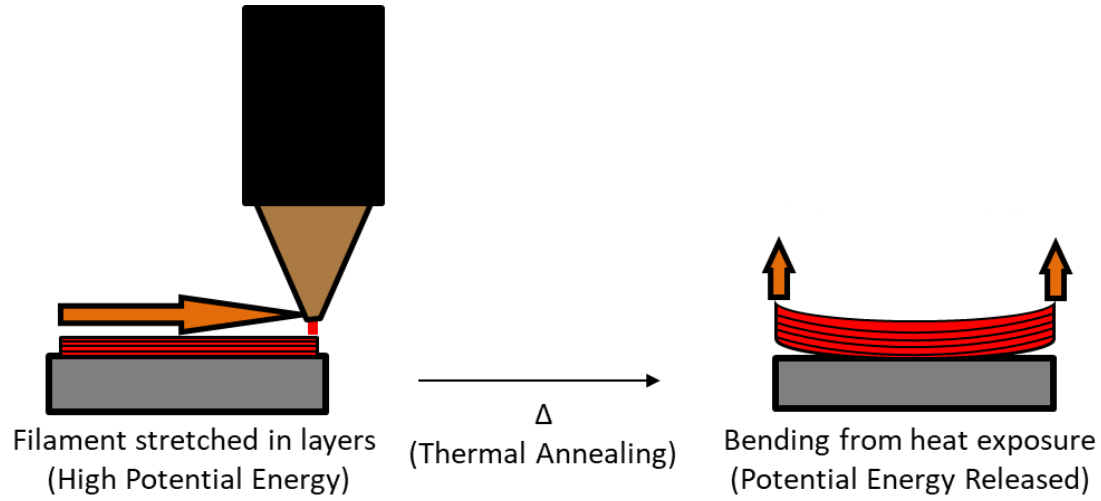


Fig. 3.1. Illustration of print warpage in an FFF process as established layers are cooled or thermally annealed.

the layered build. Despite these improvements, it is unknown what effects the low molecular weight additives have on the buildup of irreversible thermal strain during the 3D print process. Our group has also examined the effect of graphene addition to PLA filament on the mechanical and thermal properties of FFF objects. Rostom et al. demonstrated that graphene enhances the thermal conductivity of the polymer material in a similar way to carbon fibers.[27, 83, 84] The enhanced thermal conductivity results in more isotropic heat distribution in the printed object, which results in individual layers cooling more uniformly during the printing process to improve interlayer diffusion and reduce anisotropy.

The improvements in print mechanical properties with these nanoscale additives has led to the question of how their addition may change the buildup of irreversible thermal strain for PLA prints. The irreversible thermal strain in completed prints have internal stresses that are alleviated by annealing at temperatures above the filament's T_g.[26, 75, 78] By monitoring the deformation of printed objects at higher temperatures, it is possible to characterize the irreversible thermal strain in a printed object and the impact of material composition on said strain. To this end, 3D printed monoliths of filament with and without graphene and LMW PLA nanoscale additives were printed and isothermally annealed above T_g. The changes in sample length for each 3D axis were monitored as a function of annealing time. In addition, the amount of interfilament void space in the annealed samples was determined with scanning electron microscopy (SEM). Void space corrections provide a route to account for void space contraction that is captured in the macroscopic measurement and to focus on the change in the solid filament during irreversible thermal strain release. Lastly, differential scanning calorimetry provides molecular insight into the complex glass transitions of the filament and how nanoscale additives generate changes to this molecular environment. Results elucidate the different molecular characteristics of each additive

and their effects on the energetic requirements to allow for polymer chain diffusion at the microscopic level. This study also demonstrates that the presence of LMW PLA in the filament induces more irreversible thermal strain during the print process, while the presence of graphene hinders the strain release.

Experimental

Materials and Filament Composite Production

2.85 mm diameter PLA filament from GizmoDorks was used as the base material with no modifications. Modified filaments consisted of the base PLA filament with 0.5 wt% graphene and 0.5 wt% low molecular weight (LMW) 3-armed PLA. The 3-armed PLA in this filament refers to a 3-armed star shaped polymer with individual 11,000 g/mol arms to form a molecule with a molecular weight of 33,000 g/mol. The filament with the 3-arm star was available from a previously published study.[82] Reference 60 describes the 3-armed PLA synthesis and the filament generation process. To create homogenously dispersed graphene filament, a previously reported coagulation method was used.[85] In this process, 0.5 grams of graphene was added to 1 L dimethylformamide in a beaker to produce a 0.5 mg/mL solution. This solution was then sonicated for 24 hours to uniformly disperse the graphene. 50 grams of dried PLA pellets were then dissolved in the graphene solution at 65 ºC for 48 hours. PLA/graphene nanocomposite was then precipitated from the solution by mixing deionized water with the solution in a 200 mL/400 mL ratio and vigorously blending in a steel blender. Wet PLA/graphene nanocomposites were then air dried for 48 hours and further vacuum dried at 120 ºC for an additional 24 hours. Dry material was then powdered in a blender which was then crudely extruded via a Filabot screw extruder at 168 ºC.

The crude graphene filament was then pelletized and re-extruded with the same parameters to make the desired 2.85±0.1 mm filament.

Sample Printing, Thermal Annealing, and Sample Analysis

3D-printed monoliths were printed from the three filament types, pure PLA, PLA/LMW 3-armed star blends, and PLA/graphene nanocomposites. The monoliths were rectangular shapes with dimensions of 50 mm (Z) × 10 mm (Y) × 2 mm (X). 36 samples were analyzed for each filament type. The monoliths were printed with a nozzle temperature of 190 ºC and a bed temperature of 75 ºC using a Lulzbot Taz 5 FFF printer. Individual monolith layers were 0.3 mm thick, 100% infill, and a 0º parallel bead deposition pattern. Completed prints were cooled to room temperature before removal from the bed surface. Monolith dimensions were then measured with a set of engineering calipers and recorded prior to thermal annealing. Sample sets of 3 monoliths were then placed into a vacuum oven set at 85 ºC, and the dimensions of the monolith were measured as a function of annealing time.

The irreversible thermal strain, $\boldsymbol{\varepsilon}$, along each orthogonal monolith dimension was determined for each sample using Equation 3.1, where L_o and L_t are the monolith length in a set axis before and after annealing, respectively. The influence of graphene and LMW PLA on $\boldsymbol{\varepsilon}$ was determined by following the size of the monolith in each direction as a function of annealing time at 85 ºC. Monoliths dimensions were recorded to within 0.01 mm to obtain accurate recordings of the change in the size of the sample.

$$\boldsymbol{\varepsilon}\ (Irreversible\ Thermal\ Strain) = \frac{L_t - L_o}{L_o} \qquad \text{Equation 3.1}$$

The basis of this monolith analysis is derived from similar work conducted by Peterson et al.[75, 86]

Scanning Electron Microscopy and Void Space Analysis

Monoliths were placed into a liquid nitrogen bath to embrittle the polymer, allowing the samples to be cracked down the middle to expose interfilament void spaces that are imaged by electron microscopy. A diagram of this process is presented in Figure 3.2. Fracture surfaces were gold sputtered prior to imaging to prevent sample charging during SEM analysis. A Zeiss EVO MA15 electron microscope was used with a X80 magnification and a working distance of 9.5mm. Void space analysis was completed in three stages with ImageJ software as shown in Figure 3.3. In this process, the initial raw image is converted to black and white by adjusting threshold limits to isolate the void space. This image is then analyzed to determine the percent of the image that is occupied by void space. Images were taken for each annealing time step.

Glass Transition of Monoliths

Small amounts of polymer (approx. 5 mg) were cut from each monolith and placed into hermetically sealed aluminum sample pans. The thermal transitions of the monolith samples was determined with a TA Instruments Q2000 differential scanning calorimeter (DSC). DSC samples were first thermally equilibrated to 25 ºC and then heated at 5 ºC/min to a temperature of 200 ºC. This analysis was conducted for samples of each monolith at each annealing time. The glass transition and enthalpy near the glass transition of the filament was determined for each sample with TA universal software.

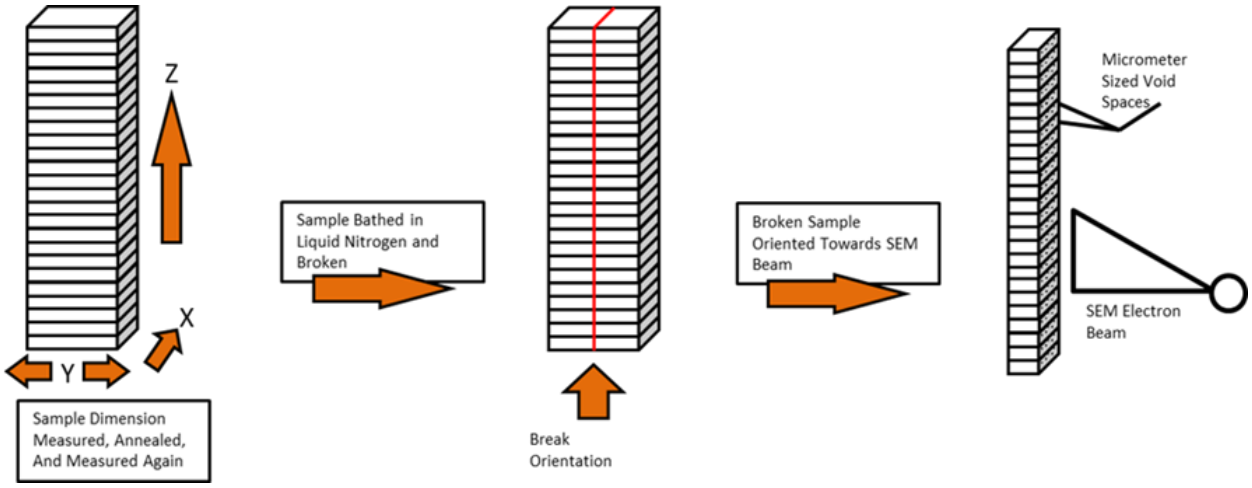


Fig. 3.2. Processing steps of dimensional analysis and SEM imaging for 3D printed monolith samples.

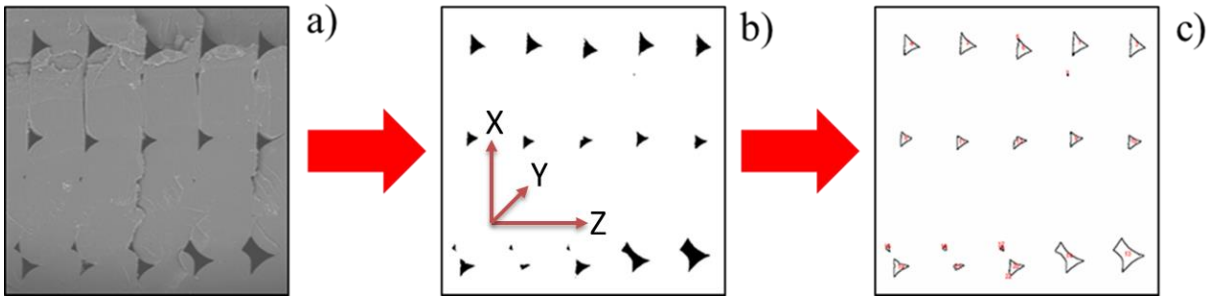


Fig. 3.3. Imaging stages of % area void space analysis consisting of **a.** raw images from SEM **b.** threshold filtration to isolate void spaces and **c.** pixel counting for area estimation.

Results

Additive Influence on Irreversible Thermal Strain (ε)

Unmodified PLA monoliths were the first samples to be printed and annealed to monitor the release of irreversible thermal strain, $\boldsymbol{\varepsilon}$, of the pure polymer filament in the printed monolith. Changes in the monolith length in the X, Y, and Z dimensions were recorded and $\boldsymbol{\varepsilon_i}$ is plotted for each direction as a function of annealing time in Figure 3.4. From these measurements, both the contraction and expansion of the sample in the Y and Z direction, respectively, are readily apparent. Within short annealing times of *ca.* 1-hour, significant deformation of the monolith is clearly observed. This suggests that the irreversible thermal strain within a sample is released rapidly. As observed in Figure 3.4a and 3.4b, a decrease in size in the Y dimension corresponds to a similar expansion in the Z direction. A potential molecular level picture of this transformation is illustrated in Figure 3.5 where individual beads in the print expand along the Z-axis while the elongated bead contracts in the Y-axis. Changes in the size of the monolith along the X-axis for all three materials were consistently near zero. For this reason, the change in size along the X-axis values were assumed to be a negligible factor in the observed monolith dimensional size.

Figure 3.4 clearly shows that both additives increase the observed amount of irreversible thermal strain released with annealing relative to the pure PLA sample. The data show that the maximum $\boldsymbol{\varepsilon}$ of *ca.* 0.075 and 0.05 occurs at 1.75 and 5 hours for the LMW PLA blends and graphene nanocomposite, respectively. The rate at which $\boldsymbol{\varepsilon}$ increases also varies with the filament composition, though the trend does not persist for annealing times longer than one hour. This macroscopic change with anneal time is consistent with molecules in the filament bead relaxing

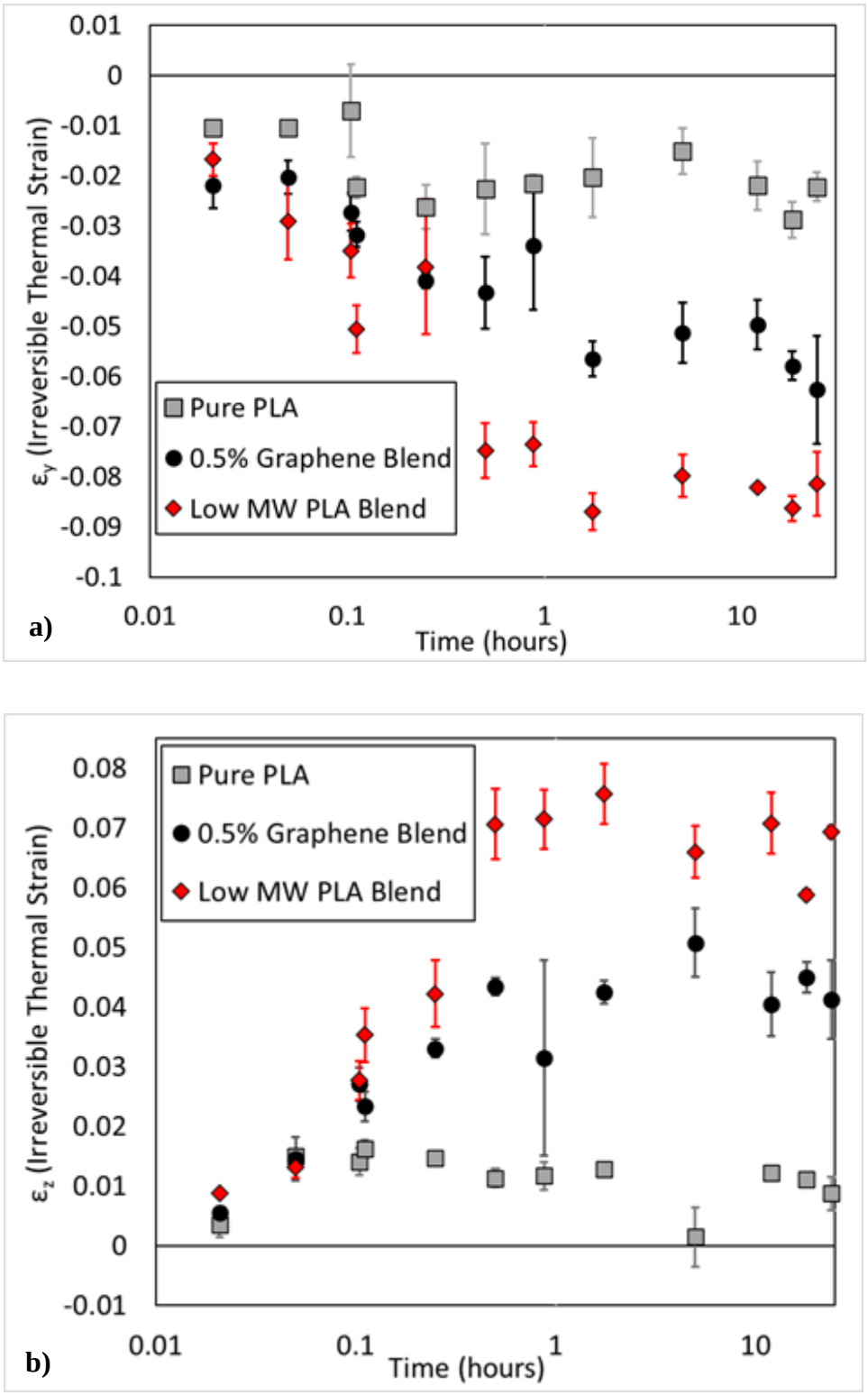


Fig. 3.4. Irreversible thermal strain (ε) of printed monoliths in the **a.** Y-axis direction and **b.** Z-axis direction with various filament additives.

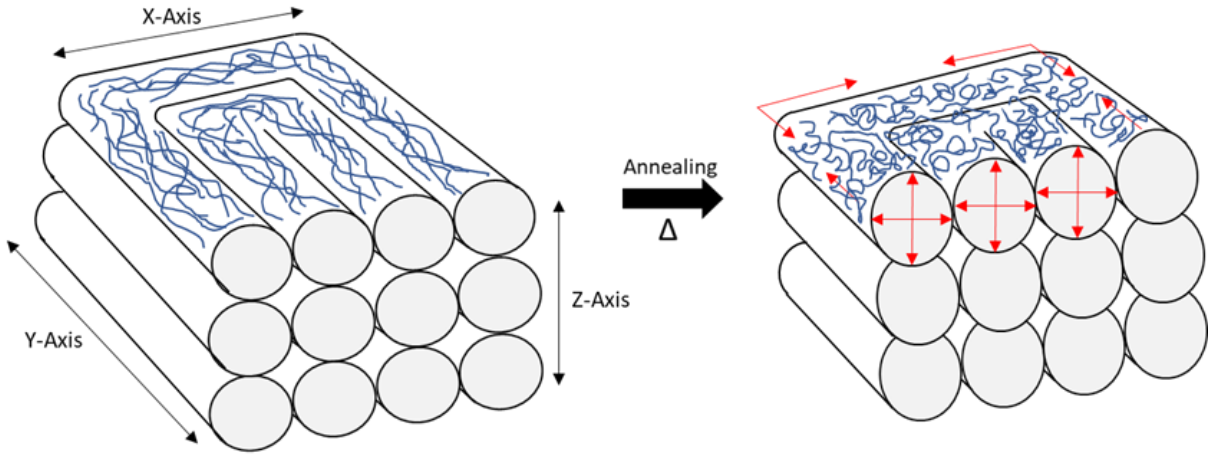


Fig. 3.5. Scanning electron microscopy images of 3D-printed monolith interfilament void space after **a-c)** 1.25 minutes and **d-f)** 24 hours of annealing at 85 ºC.

from being deformed along the y-axis during FFF deposition, to attain more isotropic states that are closer to thermodynamic equilibrium.

Although this data illustrates the effects of the nanoscale additives on the macroscopic size of the printed structure, this analysis monitors the change of the dimensions of the deposited filaments *and* the void space that resides between them. The internal structure of the monolith consists of deposited beads that change in size that follows the measured $\boldsymbol{\varepsilon}$, but also contains interfilament and interlayer void spaces that are likely to change in size as a result of irreversible thermal strain release as well. To focus our interpretation on the change in the deposited polymer and remove any artifacts from changes in void space, the contributions of the change in void space must be removed from the reported $\boldsymbol{\varepsilon}$ values. For this purpose, the percent void space in each monolith as a function of annealing time is monitored with SEM.

Void Space and Additional Strain Contributions

Figure 3.6 shows the SEM images of the cross sections of the annealed samples at the shortest and longest annealing time for each filament composition. Image contrast for each sample was adjusted to yield sharp borders between the filament material and the void spaces. The percent void space in each image was then determined via software analysis, and plotted as a function of annealing time in Figure 3.7. These results indicate that the filament with LMW PLA and the pure PLA exhibit the highest percentage of void space initially, which generally decrease with annealing. This result contrasts the change in void space of the graphene nanocomposite, where the percent void space in the sample does not change much initially, where it hovers around 1% until approximately 5 hours of annealing after which the void space expands to 2-2.5%. The decrease in void space is the result of the same microscopic process that generates the macroscopic change in size. Annealing samples above T_g releases deformed polymer chains from non-

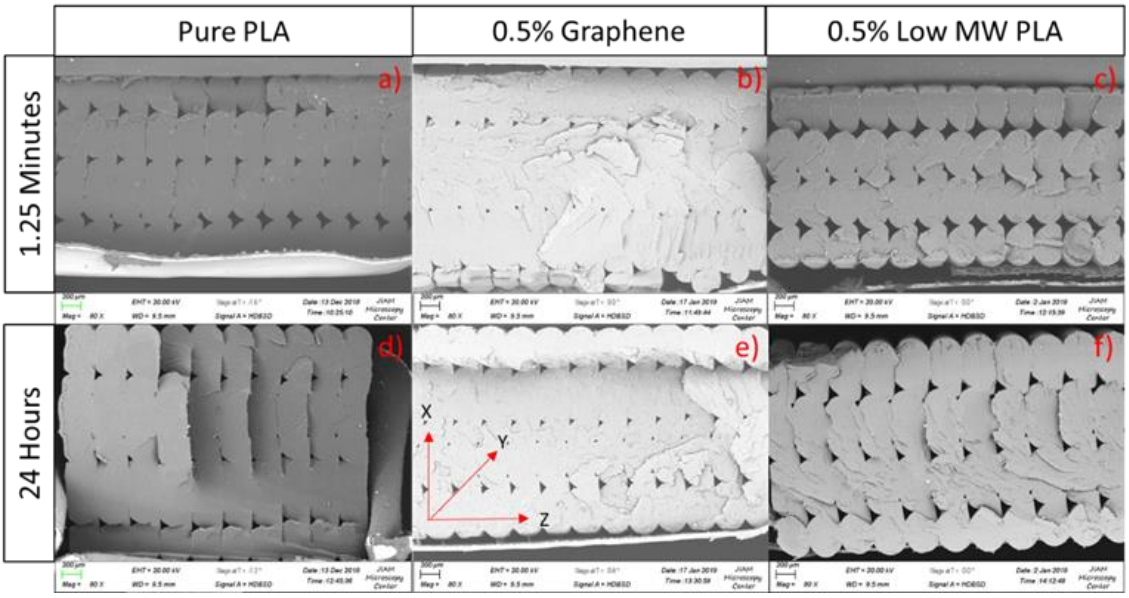


Fig. 3.6. Illustration of filament bead transformation in 3D printed monoliths before and after annealing.

equilibrium conformation and allows interfilament diffusion between the print layers, which decreases the void spaces as the bead expands in the X and Z directions. Although LMW PLA has been shown to enhance the diffusion of the polymer between filaments during print deposition, this effect does not appear to drastically increase the rate of the decrease in void space. One interpretation that is consistent with our original analysis is that the smaller LMW chains preferentially migrate to the filament bead interface during the printing process.[82] The rapid translation, therefore, limits the impact of the small chains on the amount of void space with further annealing. The graphene nanocomposite samples exhibit minimal void space that does not change much with annealing, which can be ascribed to the enhanced thermal conductivity provided by the additive.[27] Improved heat transfer during the print process extends the time above T_g, during the print process, which prolongs polymer diffusion for a given print condition. This results in a smaller amount of initial void space as observed in Figure 3.7.

To account for void space contributions in the irreversible thermal strain results (Fig. 3.4), the % area monolith void space (V) was calculated using Equation 3.2, where the SEM void space % is the calculated void space percentage as a function of annealing time. Equation 3.3 is then used to determine the void space adjusted irreversible thermal strain ($\boldsymbol{\varepsilon^*}$) of the monolith along the Z-axis. This equation removes the contribution of the void space to the macroscopic $\boldsymbol{\varepsilon}$ to emphasize the structural changes of the filament only and removes any convolution between the irreversible thermal strain induced filament expansion and void space changes. Figure 3.8 illustrates the change in Z-axis adjusted irreversible thermal strain of the three samples as a function of annealing time. It is interesting that correcting for the void space shows that the $\boldsymbol{\varepsilon^*}$ of the low M_w PLA blend effectively doubles with annealing. Moreover, the $\boldsymbol{\varepsilon^*}$ of the graphene nanocomposite and the pure PLA are very similar, while $\boldsymbol{\varepsilon^*}$ increases much more readily for the PLA with the LMW additive.

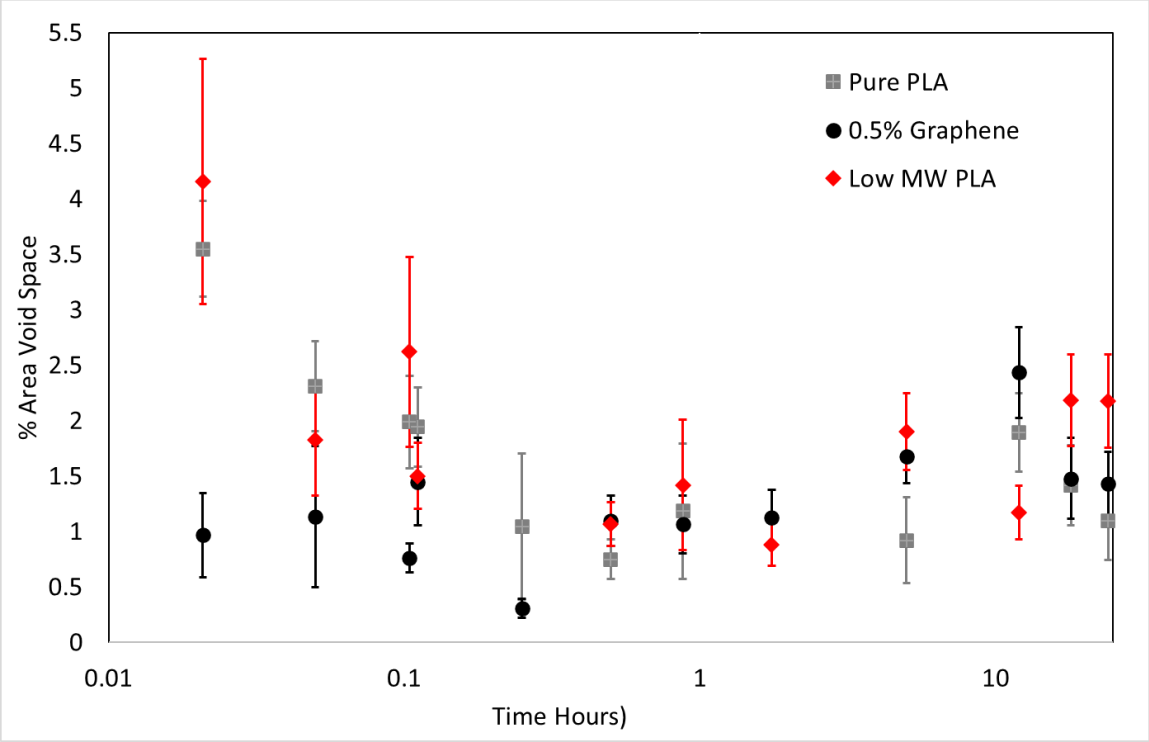


Fig. 3.7. Interfilament void space area changes within printed monolith samples as a function of annealing time.

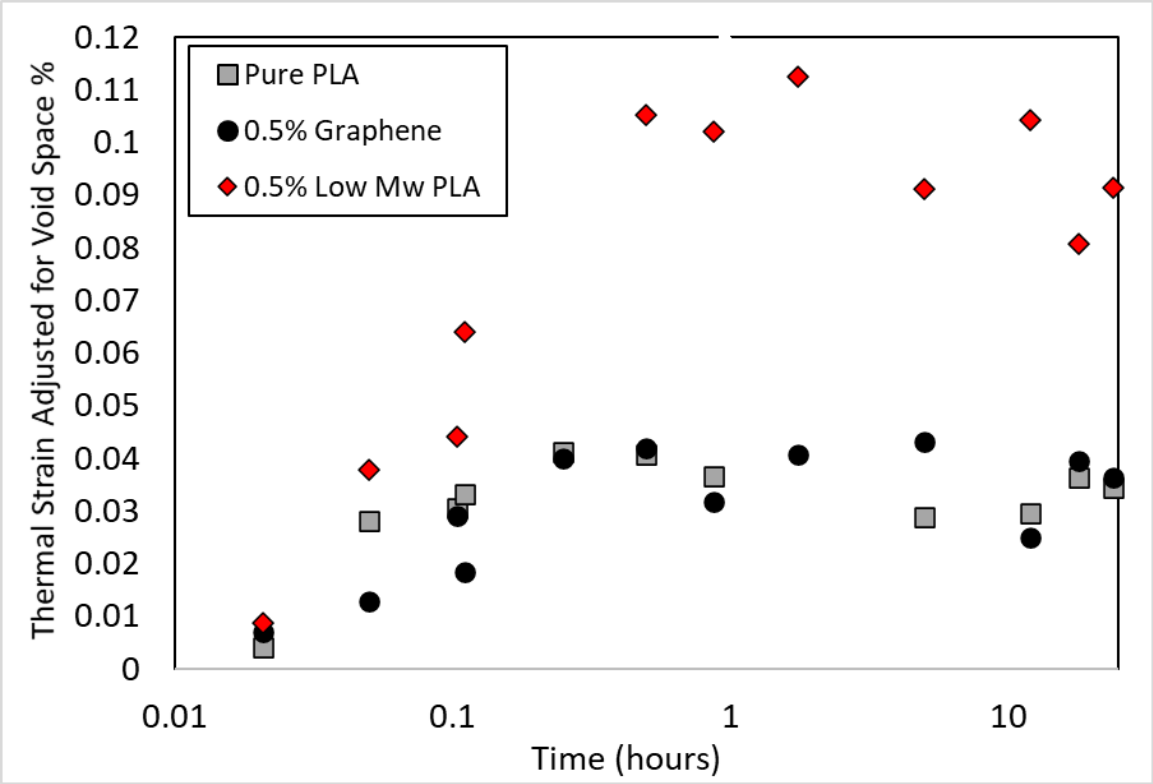


Fig. 3.8. Irreversible thermal strain (ε^*) of 3D printed monoliths in the z-axis direction adjusted for void space area.

$$\%\ Area\ Monolith\ Void\ Space\ (V) = \frac{SEM\ void\ space\ \%}{100} \qquad \text{Equation 3.2}$$

$$Adjusted\ Irreversible\ Thermal\ Strain\ (\boldsymbol{\varepsilon}^*) = \frac{[L_o \times (1-V_o)] - [(L_t \times (1-V_t)]}{[L_o \times (1-V_o)]} \qquad \text{Equation 3.3}$$

Filament Glass Transition Behavior

Differential scanning calorimetry provides insight into the thermal transitions of the printed polymer. For example, Figure 3.9 shows the DSC thermograms of pure PLA for a series of annealing times. Inspection of these curves establishes that the glass transition occurs in two steps and has a significant enthalpy associated with it. More precisely, the as-printed structure shows two T_gs, both between 55 and 60 °C, while the samples that are annealed up to thirty minutes show the separation of the two transitions. For these annealing times, the lower transition shifts to *ca.* 52-54 °C, while the higher transition remains just below 60 °C. The presence of two glass transitions indicates two conformational states of the polymer in the printed structures. Previous studies have demonstrated that the applied shear force of the deposition results in a distribution of polymer chain alignment, where the polymer near the surface of the filament is more aligned than those that reside in the center of the filament. At the bead center, polymer chains are not aligned as extensively at the surface and thus relax towards a more isotropic structure during the printing process, leading to a more isotropic bead center with thermal properties that are similar to the bulk polymer.[87, 88] Polymer that is closer to the filament surface is subjected to higher shear forces and faster cooling rates via conduction that prevent the shear aligned material from relaxing to more isotropic structures during the print process. This gradient of interfilament conformational states is consistent with the multiple T_gs observed in Figure 3.9. The isotropic bulk portion of the filament appears to undergo a T_g that manifests as the expected step function in the thermogram, while the

aligned chains near the filament surface require more thermal energy to relax, which manifests as a corresponding endothermic peak. Inspection of the size of the enthalpic peak provides insight into the barriers that exist for the transition from glassy to rubbery behavior for each sample, which is relevant to the release of irreversible thermal strain. For instance, a larger endothermic peak indicates a more deeply trapped polymer conformation, which must be freed to allow for the release of irreversible thermal strain. Thus, the enthalpy of the glass transition for each filament is plotted as a function of annealing time in Figure 3.10.

The enthalpy associated with the glass transition decreases for each filament as annealing time increases. The pure and LMW PLA modified filaments exhibit initial enthalpies of approximately 0.01 J which generally decrease with annealing over 24 hours to very low values, 0-0.003 J. The size of the endotherm decreases quickly (within minutes) for the LMW PLA filament, which we ascribe to the plasticizing effects of the LMW PLA additive. This is consistent with previous work by Levenhagen et al, which report that PLA filaments with multi-armed PLA additives have lower viscosities.[82] The polymer chains in the lower viscosity blend are more mobile, providing efficient routes to release irreversible thermal strain. This, in turn, results in more complete release of the irreversible thermal strain during annealing, which manifests in Figure 3.8 as higher contraction of the filament along the shear strain and greater bead expansion as aligned chains relax. It appears this enhanced relaxation process results in a larger change in the size of the monolith with annealing and a drastic reduction in the required glass transition enthalpy.

Conversely, graphene filament requires twice the energy to undergo the glass transition, which may be attributed to an inhibition of the polymer dynamics by the larger graphene sheet. The addition of graphene and sheet-like materials has been shown to slow polymer dynamics by acting as obstructions that reduce overall motion of the polymer.[89] Polymers in graphene

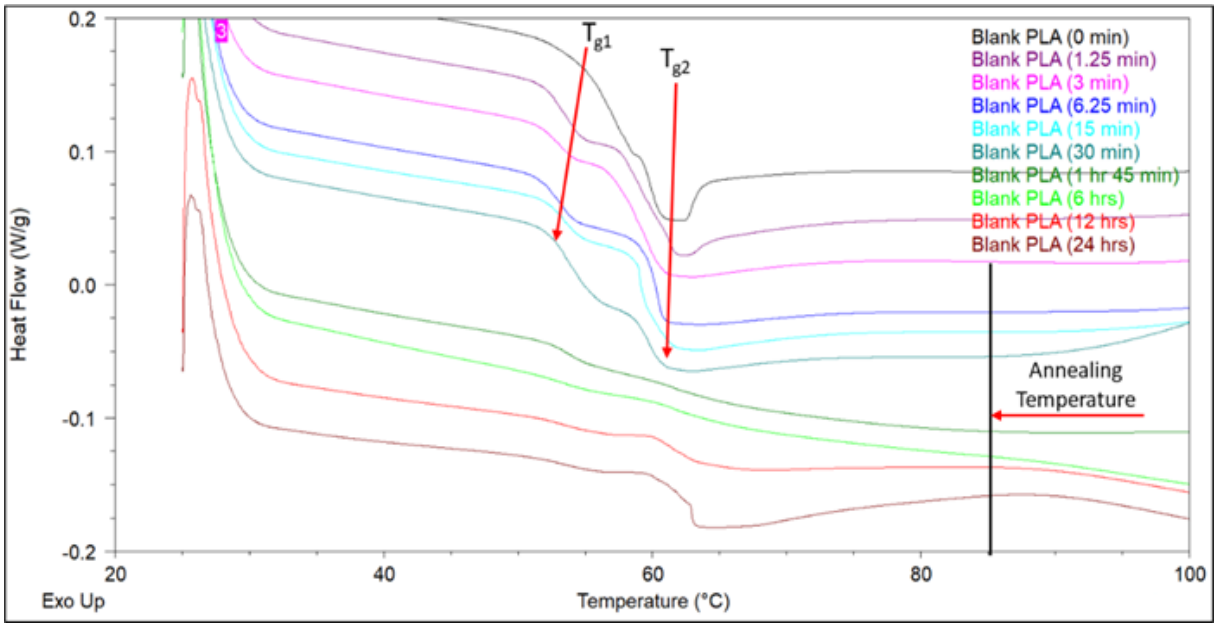


Fig. 3.9. Calorimetry scans for pure (listed here as "blank") PLA monoliths after set annealing times.

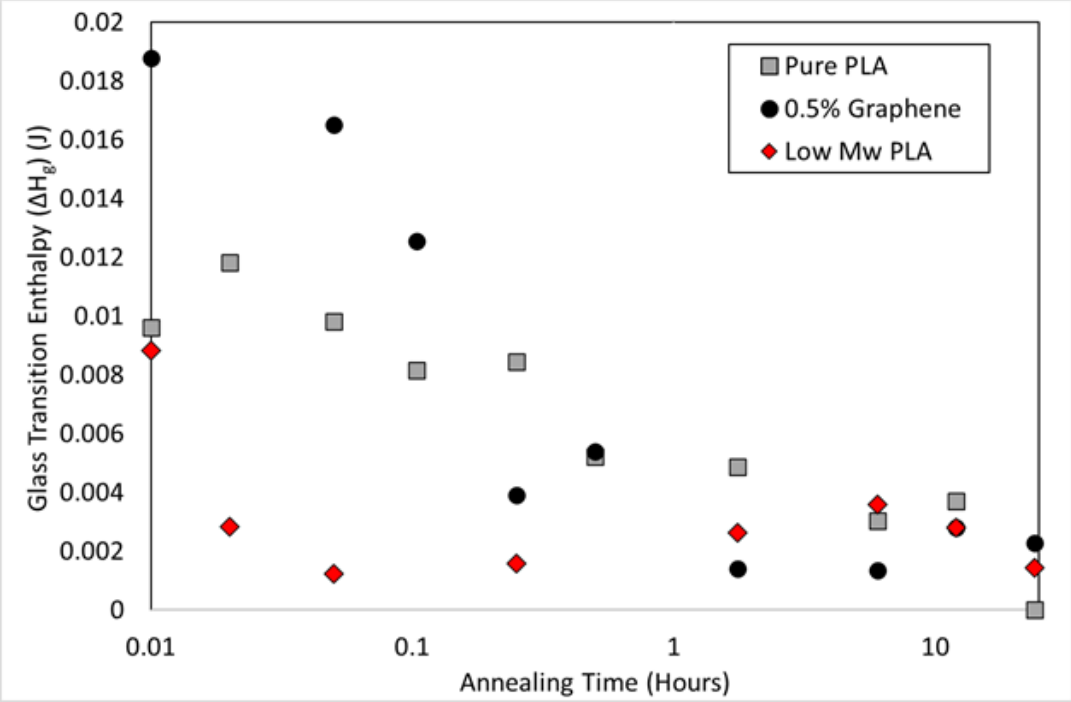


Fig 3.10. Measured enthalpy of the glass transition endotherm as a function of monolith annealing time.

nanocomposites are often attracted to the surface of the individual graphene sheets by non-covalent interactions, where these interactions drive the formation of aggregates of aligned chains parallel to the orientation of the sheet.[90-93] Under such aggregated conditions, PLA chains would require additional thermal energy to overcome the attractive forces of the graphene sheets to undergo the glass transition. The increased enthalpy required to undergo the glass transition corresponds to the slower and less efficient relaxation of deformed polymer chain conformations. This, in turn, manifests macroscopically as similar irreversible thermal strain as pure PLA with annealing but with a higher energetic barrier to induce it.

Discussion

The amount of irreversible thermal strain in a printed object clearly changes with material composition, including the incorporation of nanoscale additives. To obtain an accurate approximation of change in dimensions of the filament bead, the contribution of the void space to the macroscopic dimension that is monitored must be accounted for. This is accomplished by SEM image analysis. The corrected strain measurements then more accurately monitor the irreversible thermal strain in the filament of the printed structure, but do not provide insight into the molecular level processes that contribute to these macroscopic observations. Conversely, the enthalpy associated with the glass transition is correlated to the energetic barriers to polymer chain motion when transitioning from a glass to a rubber. Thus, this data provides insight into the molecular environment of the polymer matrix and the change in polymer dynamics generated by the additives, which in turn offers a foundation to understand the macroscopic irreversible thermal strain results. Towards this goal, a plot of the enthalpy associated with the glass transition as a function of the void space adjusted thermal strain is presented in Figure 3.11 to illustrate this relationship.

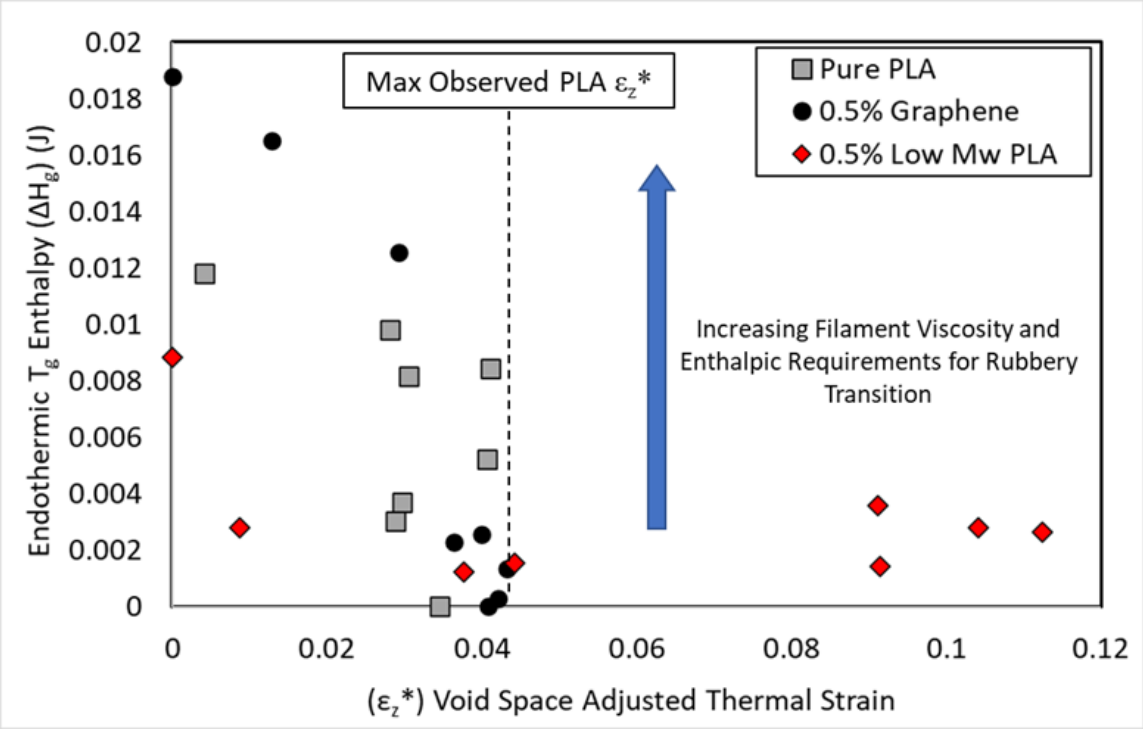


Fig. 3.11. Endothermic glass transition enthalpy as a function of Z-axis monolith thermal strain adjusted for void space.

This plot provides a correlation of how the local polymer dynamics are altered by the addition of the nanoscale additive (as monitored by the T_g enthalpy) to the amount of irreversible thermal strain in each printed object, and its release with annealing at elevated temperature. Graphene is a bulky nanoparticle that can sterically hinder polymer dynamics and increases filament viscosity. Macroscopically, however, the addition of graphene does not change the amount of irreversible thermal strain in the printed sample, which limits the benefits of the otherwise enhanced mechanical properties of this material. This is interpreted to indicate that the graphene confines the deformed chains, requiring more thermal energy to release the strain. At the same time, increase in PLA thermal conductivity by addition of graphene improves heat distribution throughout the printing process, resulting in a more uniform thermal environments, enhanced mechanical properties of transverse printed objects, and reduced amounts of irreversible thermal strain release in the final printed part. The improved thermal conductivity and slowing of polymer chain dynamics, therefore, appears to be the dominant mechanism that controls the build up of irreversible thermal strain in the PLA-graphene nanocomposites over the molecular level confinement or potential alignment correlated to the presence of the graphene.

Conversely, the addition of LMW PLA molecules leads to a higher amount of irreversible thermal strain in the final printed structure. Invoking the correlation between molecular alignment and release of irreversible thermal strain illustrated in Figure 3.5, this would imply that the printing of filament with LMW PLA, and a lower viscosity, aligns the PLA molecules more than in the neat PLA print. It is interesting that this differs from the predictions of Mcllroy and Olmsted in their computational study of the deformation of amorphous polymers during FFF printing. In this work, they estimate the extent of chain orientation, deformation, and disentanglement during the FFF extrusion and deposition process.[94] Most relevant for our studies, their results show that there

is no change in disentanglement (and alignment) with a change in polymer molecular weight. Thus, this computational work predicts that the sample with PLA with LMW should be similarly aligned on the molecular level in the FFF deposition process as in the pure PLA sample. However, the residual strain measurements clearly show differences in the warpage of the pure PLA sample and those fabricated with LMW additives. We have ongoing neutron scattering experiments to examine the change in molecular orientation of these samples to test the proposed relationship between molecular alignment and measured residual strain.

Cumulatively, these results demonstrate that the amount of irreversible thermal strain that accumulates in an FFF printed object is altered by the presence of nanoscale additives, but the manner in which the irreversible thermal strain varies is crucially dependent on the nature of the nanoscale additive. In the case of the addition of graphene, the increase in viscosity and thermal conductivity of the filament leads to a more homogeneous shear and thermal history of the sample, which inhibits the development of irreversible thermal strain. At the same time, the confinement of the polymer near the nanoparticle appears to require additional thermal energy to release the irreversible thermal strain. On the other hand, the lowering of the viscosity of the filament by the addition of the LMW PLA molecules appears to enhance molecular orientation of the polymer chains, which corresponds to an increased amount of irreversible thermal strain in the printed object.

Conclusion

Our research efforts have monitored the effects of various nanoscale additives on the irreversible thermal strain (ε) in objects printed by fused filament fabrication (FFF) with PLA by measuring the release of this strain with annealing. Printed monolith samples formed from filament with graphene and LMW 3-arm star PLA additives displayed more irreversible thermal strain

relative to unmodified PLA samples. The measured ε are a combination of the amount of void space in the monolith as well as the changes in the filament dimensions. Removing the contribution of the void space to the macroscopic measurements provides a more accurate quantification of the changes in the filament structure with annealing. Monitoring the release of this corrected strain, ε_z^*, shows that the addition of LMW PLA enhances the amount of irreversible thermal strain while the amount of strain in the sample with graphene is consistent with that of the pure PLA monolith. Calorimetric analysis of each printed structure displayed complex glass transition behavior with multiple T_g's and an associated endotherm. Correlating the release of the irreversible thermal strain to the enthalpy of endotherms near the glass transition provides a method to connect the molecular relaxation in the printed filament bead to the macroscopic dimensional changes. The observed relationships are interpreted to indicate that graphene within the PLA slows the chain relaxation, increasing the energy requirement to transition polymer to the rubbery state and release the irreversible thermal strain that develops during printing. Conversely, the addition of LMW PLA lowers the viscosity and appears to increase chain alignment, which manifests as an increase in the macroscopic strain in the printed structure. Ultimately, these results demonstrate that the addition of nanoscale additives will alter the amount of irreversible thermal strain present in an object printed by FFF. The addition of impenetrable anisotropic graphene sheets that increase viscosity and thermal conductivity creates a more homogeneous thermal history and molecular confinement that minimizes the buildup of irreversible thermal strain, which in turn limits the benefits of enhanced mechanical properties. This relationship between viscosity, thermal conductivity, and the resulting strain release provides a mechanism to incorporate nanoscale additives in objects created by FFF with modified mechanical and chemical properties and controlled strain release, providing progress towards 3D printing as a potential manufacturing technology.

Chapter 4. Immiscible Blend Changes Induced by Telechelic Oligomers and Biphasic Interface Copolymers

Abstract

In this work, the immiscible polymer blend of poly (ethylene oxide) (PEO) and poly(bisphenol-A-co-epichlorohydrin) (PBAE) is reactively compatibilized with telechelic oligomers to form multiblock copolymer interfacial modifiers. Blend mechanical properties improved with reactive compatibilization by the formation of copolymer at the biphasic interface. More importantly, the results indicate that optimization of this process requires a balance of three molecular-level processes that emerge in the reactive compatibilization of a crystalline polymer blend. Increased loading of telechelic results in the plasticization of the blend by excess telechelic, which decreases the Young's modulus. This plasticization effect can be mitigated by limiting the loading of reactive telechelics to less than *ca.* 0.5 to 1 weight percent (wt%). The presence of excess oligomer also impacts the extent of PEO crystallinity, where an increase in crystallinity is found with increased oligomer concentration, which in turn results in a higher modulus. Plasticization and change in PEO crystallinity couple to the reactive formation of multi-block copolymer compatibilizer during mixing to direct the final properties of the phase separated polymer blend. The competitive or cooperative relationship between PEO crystallization and the reactive compatibilization is then elucidated. Ultimately, each molecular process occurs throughout the blend formation process and exert varying influence on the blend mechanical properties. Plasticization lowers the blend modulus and occurs throughout the blend preparation process, but also enhances PEO crystallization. The detrimental mechanical effects of plasticization can be limited by keeping target oligomer composition to *ca.* 0.5 to 1 wt%, by presumably leaving very little unreacted oligomer after reactive processing. Thus, resulting in a system that exhibits only the reinforcing effects of blend compatibilization and PEO crystallization. The insight provided by these studies offers a more complete fundamental picture

of the opportunities for reactive compatibilization of crystalline polymer blends, which is relevant for plastics recycling.

Introduction

Polymer blends offer a material construct that offers control and tunability in the properties of commodity products. Industrially, mixing two polymers to create a new material with targeted properties is advantageous because it is achieved with available process equipment. Formation of blends is also cheaper and more rapid than research into new polymer species or polymerization techniques.[95] By varying the volume fraction of each polymer, the thermomechanical properties of a blend can be tailored to fulfill specific material engineering requirements. These composition-induced variations range from modulus enhancements to the blend's thermal properties.[96-99]

Most polymers do not mix into miscible materials, due to their low entropy of mixing. Thus, blending most polymer pairs will produce an immiscible and phase separated material with poor thermomechanical properties. Usually, the mechanical properties of phase separated blends, such as rigidity and tensile strength, are inferior to that of the original homopolymers. One reason for this is that entanglement of polymers across the interface in immiscible polymer blends is minimal. With the only forces left to strengthen the polymer-polymer interface being non-covalent interactions, the result is a phase separated mixture with poor elasticity, rigidity, or toughness.

Polymer blending is also significant for plastics recycling, where products that would normally enter landfills through municipal waste streams are converted into usable materials. Separating polymers in the waste stream by chemical composition, crystallinity, and compatibility is an important but time-consuming process that makes polymer recycling less efficient and scalable. The unfortunate reality, therefore, is that the polymers that emerge from the waste stream consist of a mixture of components. These mixtures most often form phase separated polymer blends with substandard properties. Moreover, most polymers in the waste stream (polyethylene,

polypropylene, poly(ethylene terephthalate) are crystalline polymers, and therefore developing ways to improve and control the properties of crystalline polymer blends is needed.[100, 101]

The morphology and assembly of phase separated polymer blends depends on the thermal and shear history of the blend, where the reduction in the biphasic surface area drives the minor phase polymer to form larger domains via droplet coalescence.[102-104] A depiction of minor phase droplet coalescence for a heterogeneous blend is illustrated in Figure 4.1a. Extensive research has focused on improving the properties of phase separated polymer blends by the addition of a polymeric interfacial modifier as a compatibilizer.[105, 106] A common compatibilizer is a copolymer that consists of monomers that are compatible with both blend components. When added to the blend, the copolymer migrates to the biphasic interface to potentially lower interfacial tension, increase entanglements across the biphasic interface, and minimize droplet coalescence. As demonstrated in both simulations and experimental blend work, the effectiveness of an added copolymer as a compatibilizer is influenced by a number of factors. These parameters include the compatibilizer molecular weight, the number and length of block segments, and the sequence distribution of the monomers in the copolymer.[97, 105-110] Numerous copolymer architectures have been examined as blend compatibilizers, from diblock copolymers to alternating and random copolymers. Previous research by Eastwood and Dadmun shows that a particularly effective copolymer sequence distributions for compatibilization are multi-block copolymers with monomer blocks that are of sufficient length to entangle with the chains of their respective homopolymer phase.[44, 45]

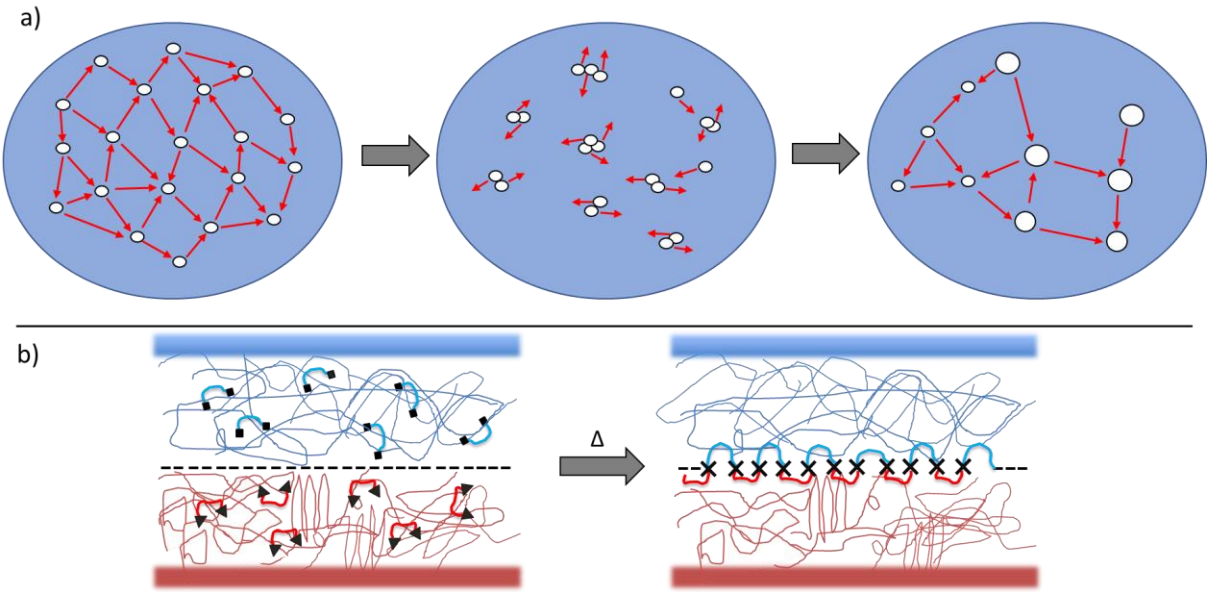


Fig 4.1. Diagrams of minor phase droplet coalescence in an immiscible polymer blend **a)** and the formation of blocky copolymer from the reaction of telechelic oligomer end groups at the biphasic interface **b).**

Compatibilizing copolymers can be introduced into a blend by different methods. The first requires that copolymer be made in a separate reaction and then added to the blend during melt mixing. The second compatibilization technique utilizes reactive components that are added to the pre-mixed blend composition that diffuse to the biphasic interface during mixing and react to form the compatibilizer.[46, 111, 112] Previous research in our group has demonstrated that the reaction of reactive oligomer species, or telechelics, is an effective reactive processing protocol. In this process, the telechelics diffuse rapidly in the blend during the high temperature melt mixing to form a copolymer at the biphasic interface via the reaction of end-chain functional groups (Figure 4.1b).[113, 114] The rate of copolymer formation in this reactive processing scheme is influenced by several factors, including end-chain functional group reactivity, oligomer migration from bulk homopolymer to the interface, and the number of entanglements or crowding of copolymer chains at the interface.[46, 112, 115, 116] It has also been shown that larger chain length oligomers have slower rates of reaction compared to smaller chains due to their slow diffusion to the biphasic interface.[112] These results therefore show that the formation of multi-block copolymers by the reactive processing of telechelics act as an effective compatibilizer of heterogeneous polymer blends.

The results reported here extend our knowledge of the utility and limitation of reactive compatibilization to improve the properties of phase separated crystalline polymer blends. Previous work by O'Brien et. al. demonstrated the importance of excess reactive telechelic in the compatibilization of crystalline polymer blends, where the plasticization of the blend by unreacted telechelic impacts polymer crystallinity and blend mechanical properties.[114] This study was conducted at a fixed telechelic loading, 10 wt%, and did not examine lower telechelic loadings. In another study, Ashcraft examined the reactive compatibilization of amorphous polymer blends with variable telechelic concentration. These studies demonstrate that excess unreacted telechelic

accelerates, rather than inhibits, droplet coalescence.[113] Therefore, the purpose of this research is to generate a more complete understanding of how telechelic loading impacts the reactive compatibilization of crystalline polymer blends and identify the optimal oligomer concentration needed to create samples with the improved mechanical properties.

This research effort also examines the impact of the telechelic end group reactivity on blend compatibilization. Orr et al. determined the reaction rates of various functional end group pairs in the reaction of end-functionalized polymers to form block copolymers. These results showed that the most rapid reaction involves primary amines and cyclic anhydrides.[117] Although these functional groups have the fastest reaction rates, this reaction has limitations that make it less suitable for commercial applications. A more scalable and tolerant reaction, though slower, is the formation of ester linkages from the reaction of carboxylic acid and epoxy groups, often used in commercial resins. Previous studies suggest that this reaction is sufficiently fast to compatibilize amorphous polymer blends but has not been studied in the more complex process of compatibilizing crystalline polymer blends. Thus, in these studies, the use of poly(ethylene oxide) (PEO) and Poly(bisphenol-A-co-epichlorohydrin) (PBAE) telechelic oligomers with carboxylic acid and epoxy end groups, respectively, to reactively compatibilize the crystalline blend of their respective homopolymers is examined.

Experimental

Materials

Homopolymer, reactive, and unreactive oligomeric PEO were purchased from Sigma Aldrich as white powders. PEO polymers consisted of a 100,000 g/mol weight-average molecular weight (M_w) species, and two oligomer PEO species of 3,000 g/mol M_w. The reactive PEO oligomer chains were set with carboxylic acid functional groups while the unreactive versions

were only functionalized with hydroxyl group chain ends. Opaque 50,000 g/mol M_w PBAE pellets were obtained from Alfa Chemistry, while the 4,000 g/mol number-average molecular weight (M_n) epoxy terminated PBAE was obtained from Sigma Aldrich. The structure of the reactive telechelics, including their respective end group functionalities, is presented in Figure 4.2.

Blend Dogbone Sample Production and Mechanical Property Testing

The ratio of homopolymers in the blend remained constant at 70:30 PBAE:PEO by weight (abbrev. wt%). As reported in previous work, this blend composition is miscible at the melt mixing temperature of 150 ºC, but phase separated at lower temperature.[114] Blends containing approximately 0.5 to 10 wt% oligomer were added to the blend with a 1:1 molar ratio of PBAE-epoxy to PEO-carboxy to allow for reactive blending. Total sample mass for each blend placed into the melt extruder was approximately 1 gram. Blend samples were generated by continuous mixing in a high temperature ATLAS laboratory extruder over a period of 15 minutes at 150 °C. Extruder temperature was then elevated to ≈200 °C for a short period before rapid extrusion of the blend into an ASTM D638 compliant stainless-steel dogbone mold. Dogbone samples were left at room temperature in closed glass vials for set periods of time between extrusion and subsequent mechanical analysis. The tensile properties of each dogbone sample was measured with an Instron Model 5567 Universal Tester, with a 30 kN load cell at a rate of 10 mm/min until sample failure. An illustration depicting the experimental procedure of this study is illustrated in Figure 4.3.

Differential Scanning Calorimetry and % Crystallinity Methods

Thermal properties for each sample were obtained with a TA Instruments Q-2000 Differential Scanning Calorimeter. Samples consisted of 5 mg of dogbone material that was placed

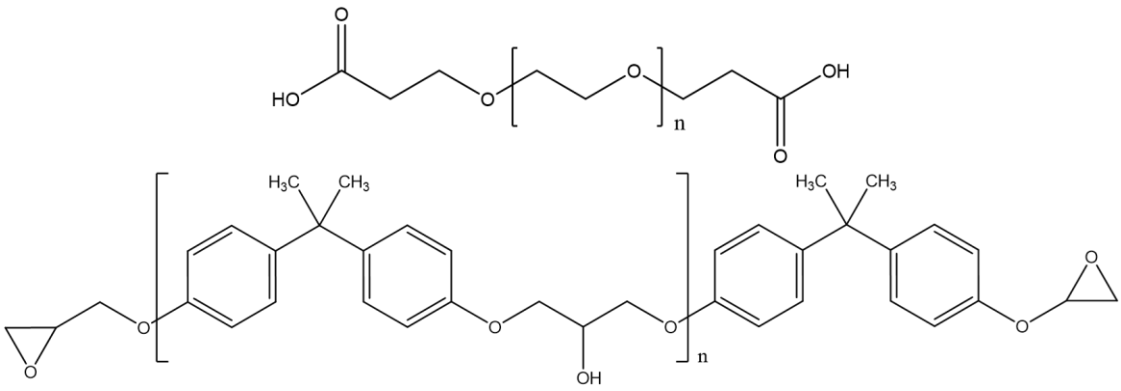


Fig. 4.2. Molecular structures of both the homopolymer and oligomer species used in this study with paired end chain functional groups, PEO **(top)**/ PBAE **(bottom).**

.

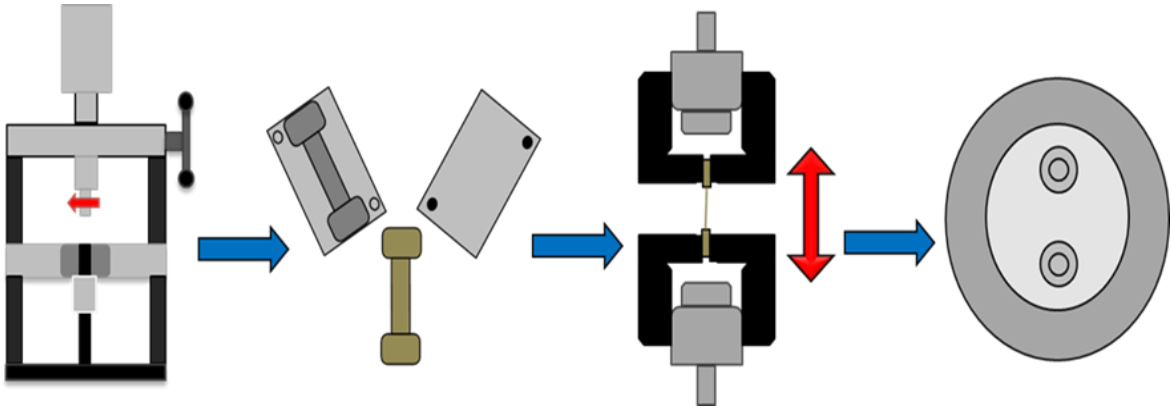


Fig. 4.3. 70/30 PBAE: PEO blend tensile sample generation and analysis via melt mixing and extrusion, dogbone mold setting, tensile analysis, and calorimetry.

into hermetically sealed aluminum sample pans and heated at 5 °C/min from -10 to 200 °C. Since PBAE is an amorphous polymer and the T_g of PEO is ca. -60 ºC, the calorimetry scans of each blend contained only the melt endotherms of the PEO phase.[32] In order to determine the percent crystallinity of PEO in the blends, the area of the melt endotherm, ΔH_f^{obs}, was divided by the melt enthalpy of 100% crystalline PEO (ΔH_f^o). The equation for % crystallization of PEO in our samples is shown in Equation 4.1.

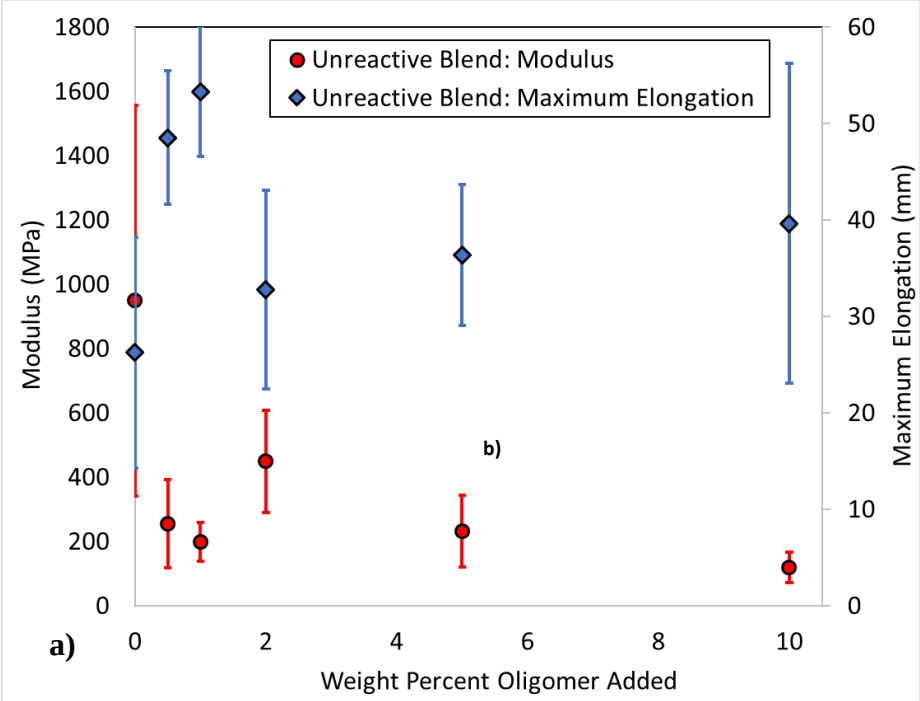
$$\% \, Crystallization = \frac{\Delta H_f^{obs}}{\Delta H_f^{\circ}} \times 100\% \qquad \text{Equation 4.1}$$

The enthalpy of fusion for a pure crystalline PEO sample was obtained from the literature as a constant of 197 J/g.[118]

Results and Discussion

Blend Mechanical Properties with Increasing Oligomer Concentration

The initial experiments determined the tensile properties of blends that contain 0.5 to 10 wt% reactive telechelic. The molecular weight (M_w and M_n) of the telechelics are exactly 3 to 4 kg/mol, and the known entanglement molecular weights of PEO and PBAE are *ca.* 1600 and 1780 g/mol respectively.[119, 120] Entanglement of the blocks formed from the reactive telechelic with each homopolymer is a crucial process in the effective compatibilization of the blends. Therefore, employing telechelics of these molecular weights of sufficient entanglement between the compatibilizer and the homopolymers.[44, 45] Blends were created with oligomers containing reactive and unreactive end groups to verify the importance of the formation of multi-block copolymers on the compatibilization process. Figure 4.4 shows the modulus and maximum elongation of blends containing both reactive and unreactive telechelic oligomers as a function of telechelic loading.



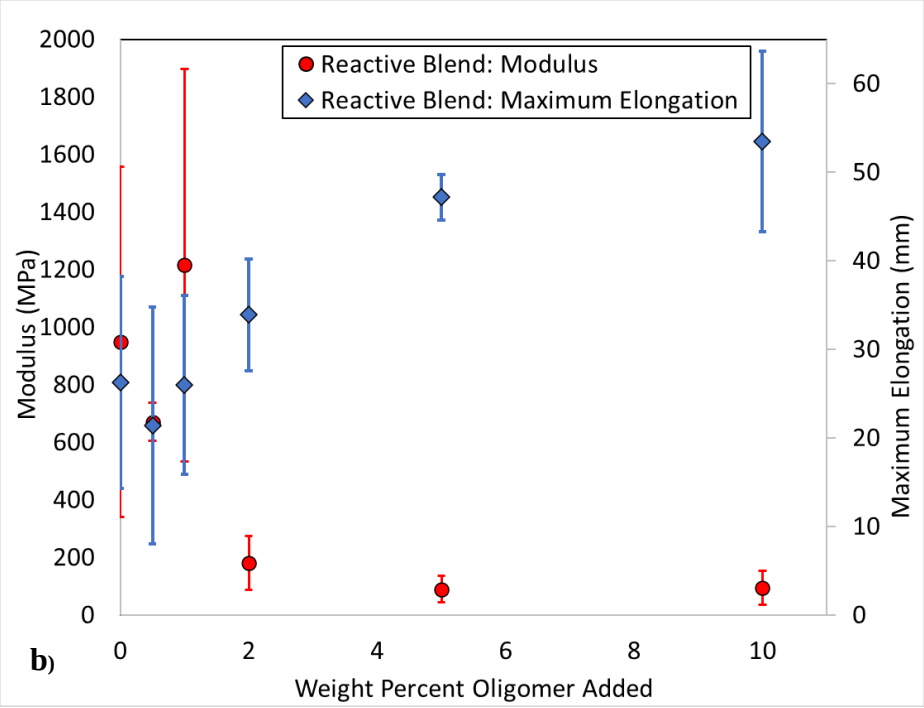


Fig. 4.4. Modulus and maximum elongation values versus **a)** reactive and **b)** unreactive wt% telechelic oligomer for a 70/30 PBAE: PEO blend.

The modulus of the blends containing unreactive oligomer decreases with increased oligomer loading while also exhibiting an increase in the blend's maximum elongation. In comparison the blends containing reactive telechelics shows an initial increase in modulus at low telechelic loading (≤ 1 wt%), followed by a decrease. Similarly, the maximum elongation initially decreases at low telechelic loadings (≤ 1 wt%) but increases at higher telechelic loadings.

The increase in modulus of the reactive blend at low oligomer loading indicates that the PEO and PBAE telechelics react to form compatibilizers that stabilize the biphasic interface. This molecular level strengthening decreases beyond 2 wt%. The increased elongation and decreased modulus in the unreactive blends and ≥ 2 wt% in the reactive blends can be attributed to the plasticization of the blend from unreacted oligomer.[114] In the reactive blend at higher telechelic loadings, unreacted oligomers become plasticizers, leading to softening of the blend and decreased stiffness. These results therefore demonstrate that to minimize the impact of unreacted telechelics, the desired telechelic concentration is below approximately 2 wt%. These results also demonstrate the viability of the carboxyl/epoxy end chain reaction as sufficiently fast for use in the reactive compatibilization of polymer blends. Though the reactive rates are not as rapid as other functional groups, the copolymer formation under the mixing time is sufficiently fast to improve the properties of the polymer blend. As demonstrated below, copolymer formation and compatibilization is only one of several molecular processes that contribute to blend mechanical properties.

Impact of PEO Crystallinity on Blend Properties

Like any crystalline polymer, the extent of crystallinity in PEO will impact its mechanical properties. As in most polymers, increasing crystallinity usually correlates to increased modulus and decreased extension at break. These property variations are similar to those that are expected

from increased blend compatibilization, and therefore it is important to provide information that provides insight into the relative importance of reactive compatibilization and PEO crystallinity on the reported tensile properties. To clarify the relative importance of PEO crystallization on the mechanical properties, the mechanical properties of the blend samples are correlated to the PEO crystallinity for blend samples with ≤ 2 wt% oligomer as a function of time after extrusion. The modulus and elongation as a function of time after extrusion is presented in Figure 4.5.

The moduli of the blends with reactive oligomer are below that of the pure blend for most of the annealing procedure. However, at the longest annealing time, 96 hours, the moduli of the blends with reactive oligomer surpass the modulus of the pure blend. At the longest annealing time, the moduli decrease with telechelic oligomer loading, 0.5 wt% > 1.0 wt% > 2.0 wt %. In fact, the modulus of the 0.5 wt% telechelic blend is twice that of the unmodified blend. The decrease in blend stiffness with increasing reactive telechelic is correlated to the plasticization due to unreacted telechelic. As the reaction between telechelics is minimal at room temperature, this data demonstrates that another molecular level change, i.e., PEO crystallization, contributes to the observed increase in mechanical stiffness and is dependent on the amount of telechelic oligomer in the blend.

PEO Crystalline Changes and Blend Molecular Interactions

At room temperature, PEO is above its T_g of *ca.* -60 ºC, meaning the chains are sufficiently mobile to crystallize. The rate of crystalline formation is assumed to be enhanced by the plasticization of the polymer matrix by the telechelic. Therefore, for a given thermal history, the sample with more excess telechelic should correlate to a sample with more PEO crystallinity. This increased crystallinity then leads to increased stiffness, observed as an increase in the blend modulus. This sets up an interesting coupling, where the plasticization by excess telechelic softens

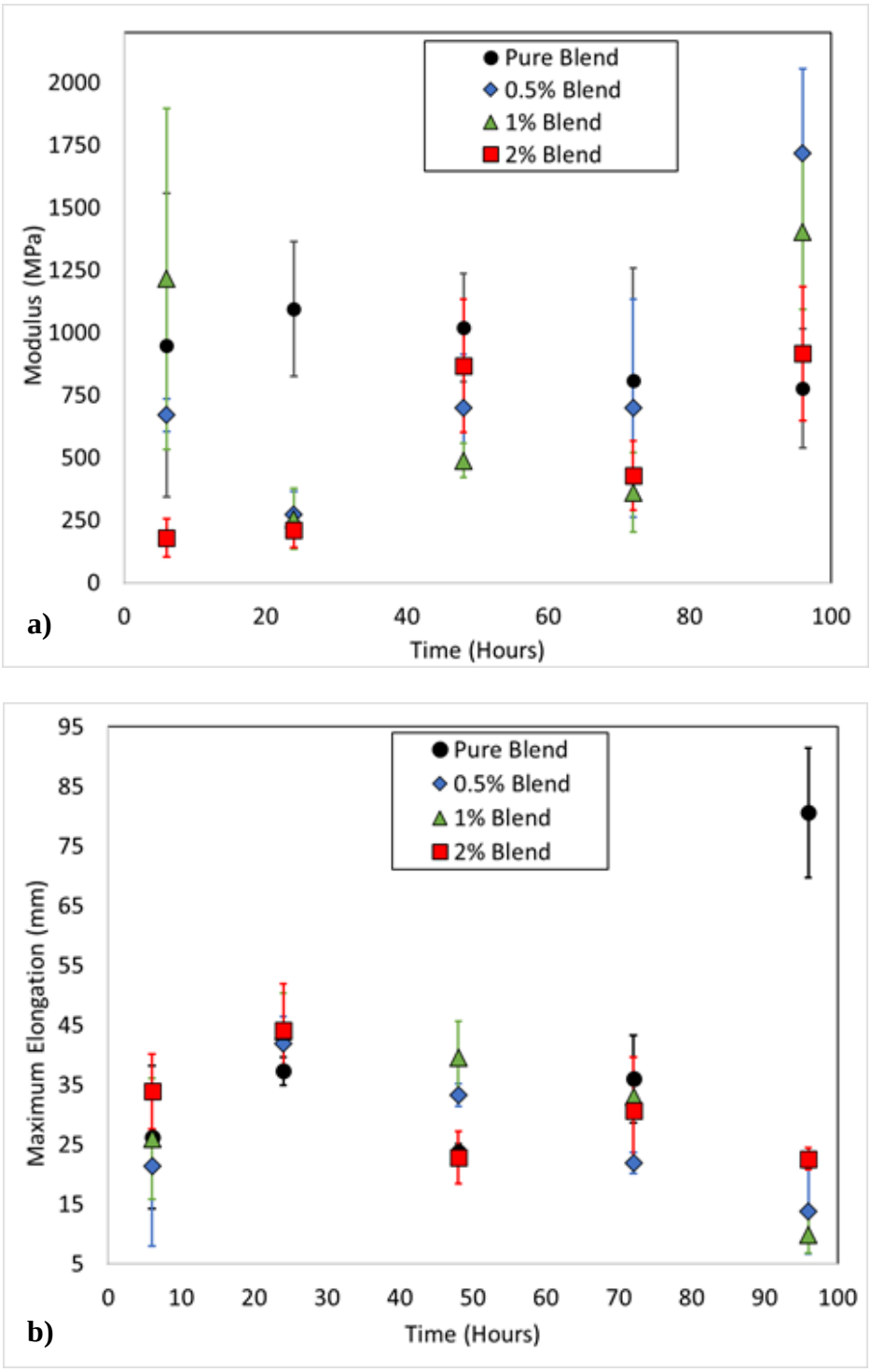


Fig. 4.5. a) Modulus and **b)** Maximum Elongation values of 70/30 PBAE: PEO tensile samples with ≤ 2 wt% reactive telechelics as a function of wait time at room temperature.

the material, which may be counterbalanced by increased PEO crystallinity that will make the material more rigid. Thus, the mechanical improvements driven by increased crystallization, will compete with the softening due to plasticization, where it appears the plasticization effects dominate at higher telechelic loading. To more thoroughly quantify these contributions of PEO crystallization to the tensile properties of the blends, the extent of PEO crystallinity in each blend was determined as a function of time after extrusion.

The enthalpy of PEO melting in the blends of interest was determined in a series of DSC experiments. Example calorimetry scans for the 0.5 wt% telechelic blend is shown in Figure 4.6. The enthalpy of melting of PEO in each blend was then converted to % PEO crystallinity with Equation 4.1. The percent PEO crystallinity values for each blend studied is plotted as a function of time after extrusion in Figure 4.7. Every blend, regardless of telechelic concentration, shows an increase in the amount of crystalline PEO as time after extrusion increases. For blends containing 0 to 1 wt% of telechelic, the PEO crystallization rate is relatively unchanged from that of the pure blend. The trend, however, does change for the 1 wt% sample, where 96 hours after extrusion, the crystalline content increases from 4% to *ca.* 9%. For the samples with 2 wt% telechelic, the rate of crystallization increases further, where the amount of crystalline PEO is double or triple that of the pure blend. This rapid increase in crystallinity in the 2 wt% telechelic is consistent with the plasticization of the blend by unreacted oligomer. Thus, it appears that for this mixing procedure, unreacted telechelic impacts PEO crystallinity if the telechelic loading is $\geq$ 1 wt%, but not when the telechelic loading is less than ~ 1 wt%. Although the analysis shows that PEO crystallinity changed with time in these polymer blends, it is still not clear whether the compatibilization of the blend by the reactive processing or the change in PEO crystallinity is the dominant factor in determining the variation in tensile properties. To determine how these processes compete or

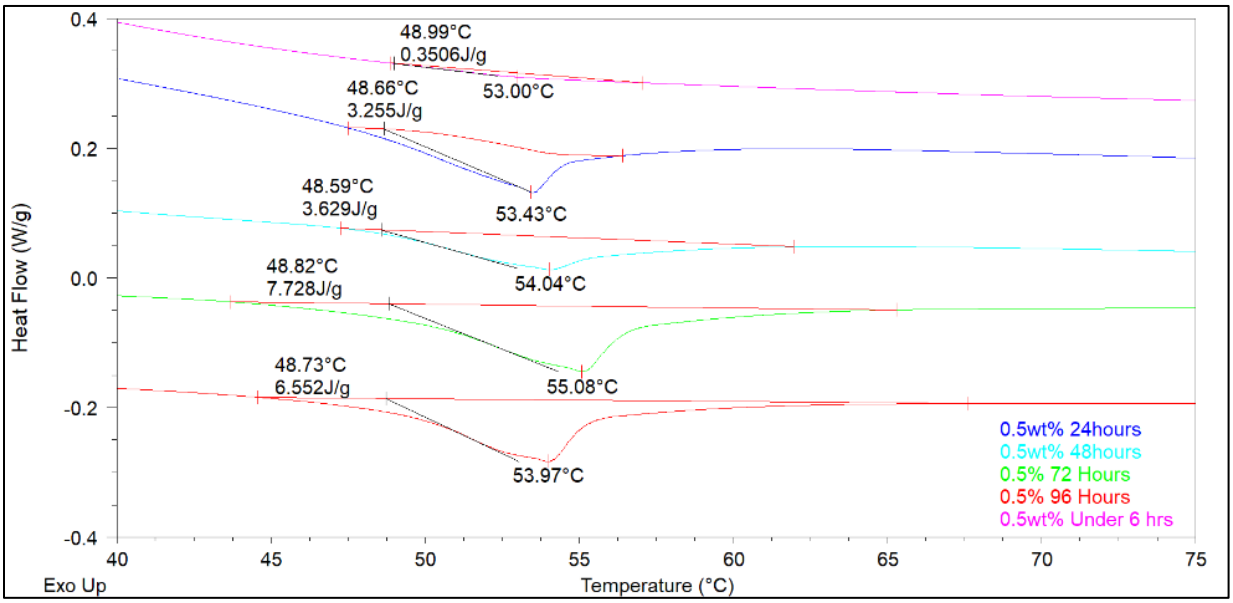


Fig. 4.6. Calorimetry scans of a 70/30 PBAE: PEO blend with 0.5 wt% reactive telechelic oligomers at increasing time spans at ambient temperature and the subsequent PEO phase melt enthalpy measurements.

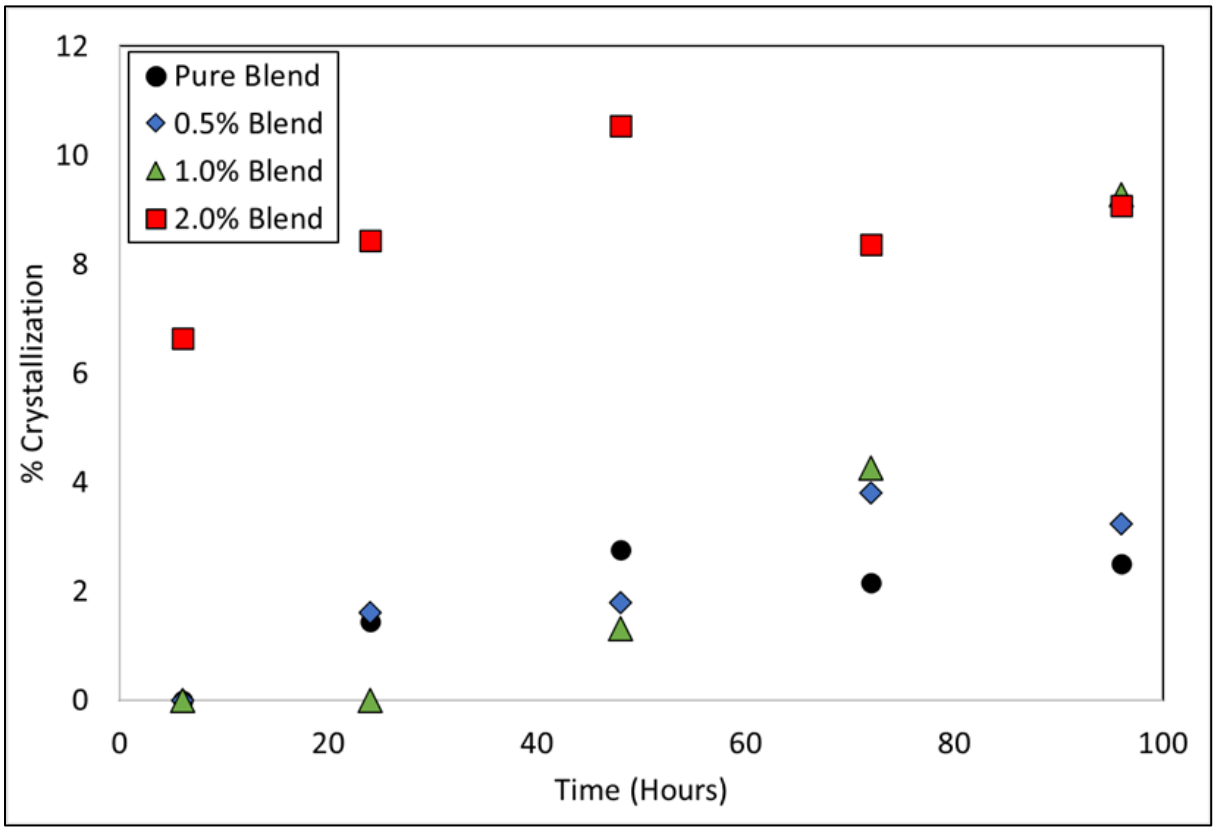


Fig. 4.7. Calculated % PEO crystallinity for 70/30 PBAE: PEO blends with 0 (Pure) to 2 wt% reactive telechelic oligomers as a function of ambient temperature wait time.

behave synergistically in the blend, the correlation of blend mechanical properties to the PEO crystallinity must be clarified. Thus, a plot of the modulus of the blends as a function of PEO crystallinity, is presented in Figure 4.8.

Figure 4.8 shows that the blend moduli varies with oligomer addition. The pure blend shows little change in PEO crystallinity and little variation in its modulus. At the highest telechelic loading, 2 wt%, blends show significant PEO crystallinity (> 7%), but moduli that are about the same or less than that of the pure blend. We interpret this trend to signify that the plasticizing effect of excess telechelic dominates the mechanical properties in these samples. If the PEO crystallinity dominated the mechanical behavior of these samples, the moduli would exceed that of the pure samples. The 0.5 and 1.0 wt% telechelic blends appear to exhibit a transition, at low PEO crystallinity a short time after extrusion, where the modulus of these blends is less than that of the pure blend with similar PEO crystallinity. However, there are samples, at longer time after extrusion, where the modulus is significantly higher than that of the pure blend with similar % crystallinity. For these samples, it appears that there is another factor that improves the polymer moduli, which we ascribe to the compatibilization of the blend by the reactive formation of copolymeric interfacial modifiers. The fact that these improved properties are only observed in the samples with 0.5% and 1.0% telechelic is consistent with the interpretation that there is little excess unreacted telechelic oligomers in the 0.5% and 1.0% telechelic samples (Figure 4.7).

Thus, there are three molecular level processes that must be considered in the successful reactive compatibilization of crystalline polymer blends, the formation of compatibilizer, PEO crystallization, and blend plasticization by excess unreacted oligomer. During the blend formation process, the growth of crystalline domains within the PEO phase leads to a steady increase in blend modulus. At longer crystallization times, cooperation of PEO crystallinity and compatibilization

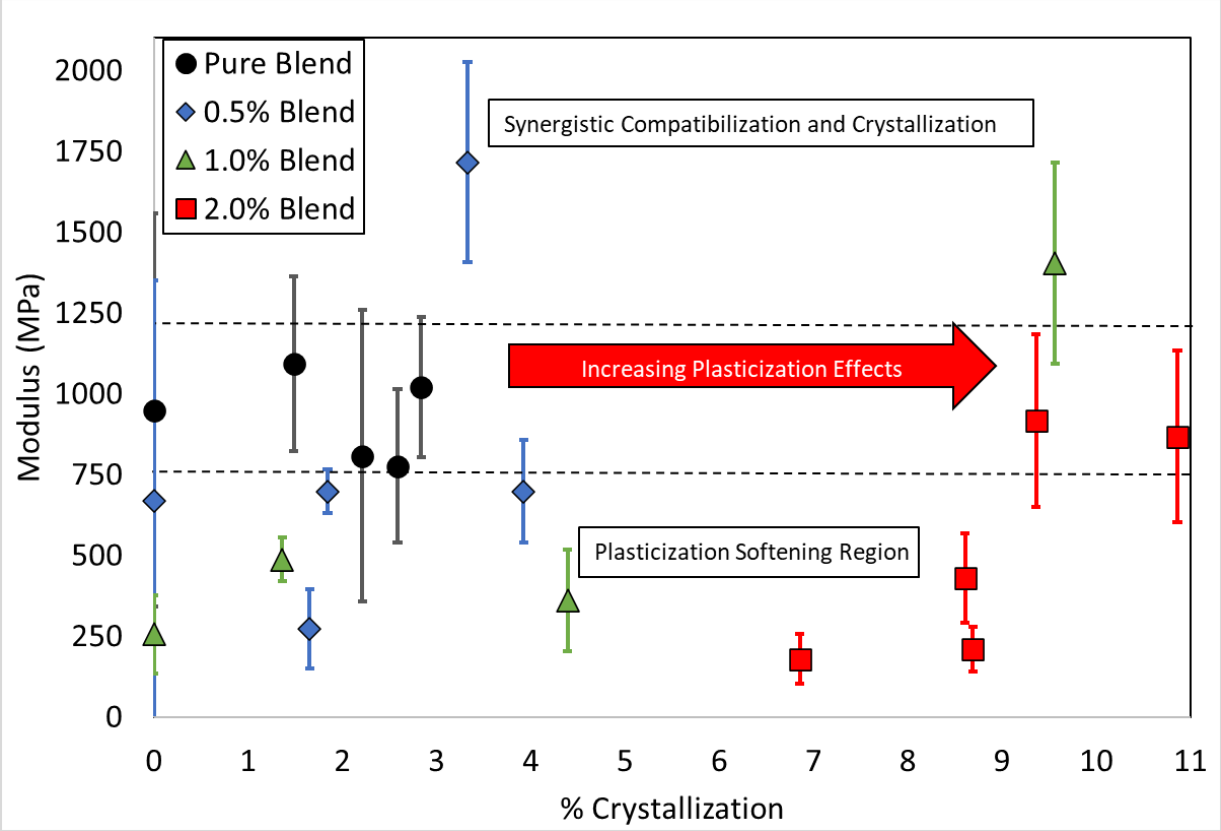


Fig. 4.8. Changes in modulus vs. % PEO crystallinity for 70/30 PBAE: PEO blends with 0 (Pure) to 2 wt% reactive telechelic oligomers.

generates a mechanically strong material, potentially forming a blend with a higher modulus than that of the uncompatibilized pure blend. However, at higher telechelic loadings, between the 1 and 2 wt% in these studies, the observed mechanical improvements are dominated by the plasticization of the sample by excess unreacted telechelic oligomer. This transition is documented in Figure 4.8, where the 2 wt% telechelic sample never attains a modulus that exceeds that of the pure blend, even with higher PEO crystallinity. Thus, the optimum oligomer composition to realize strengthening of the compatibilization and crystallization processes but minimize the potential plasticization of the telechelic oligomer is less than *ca.* 1 wt%.

Therefore, these results indicate there is a need to understand and balance the molecular processes that impact the properties of a crystalline polymer blend that is reactively compatibilized and is crucially dependent on the loading of the telechelic oligomer. To illustrate the complex interplay between these molecular processes, Figure 4.9 is a diagram that links the relationship and contribution of each process to the mechanical properties of a reactively compatibilized crystalline polymer blend. Interestingly, each molecular process appears to impact the blend properties at different stages of the blend formation process. Plasticization occurs throughout the blend formation process and acts as both beneficial and antagonistic to blend properties. Compatibilization, which is dominant during the mixing at elevated temperatures, competes with plasticization at early times. On the other hand, diffusion of the oligomers to the biphasic interface is likely enhanced by the lowered matrix viscosity from plasticization. Faster oligomer diffusion to reaction sites should induce faster rates of copolymer formation. PEO crystallization occurs at later times in the blend formation process. The % PEO crystallinity is greatly enhanced with plasticization at higher telechelic loadings, i.e., 2 wt%. Moreover, at these loadings the plasticization dominates the blend properties over the effects of increased crystallization and

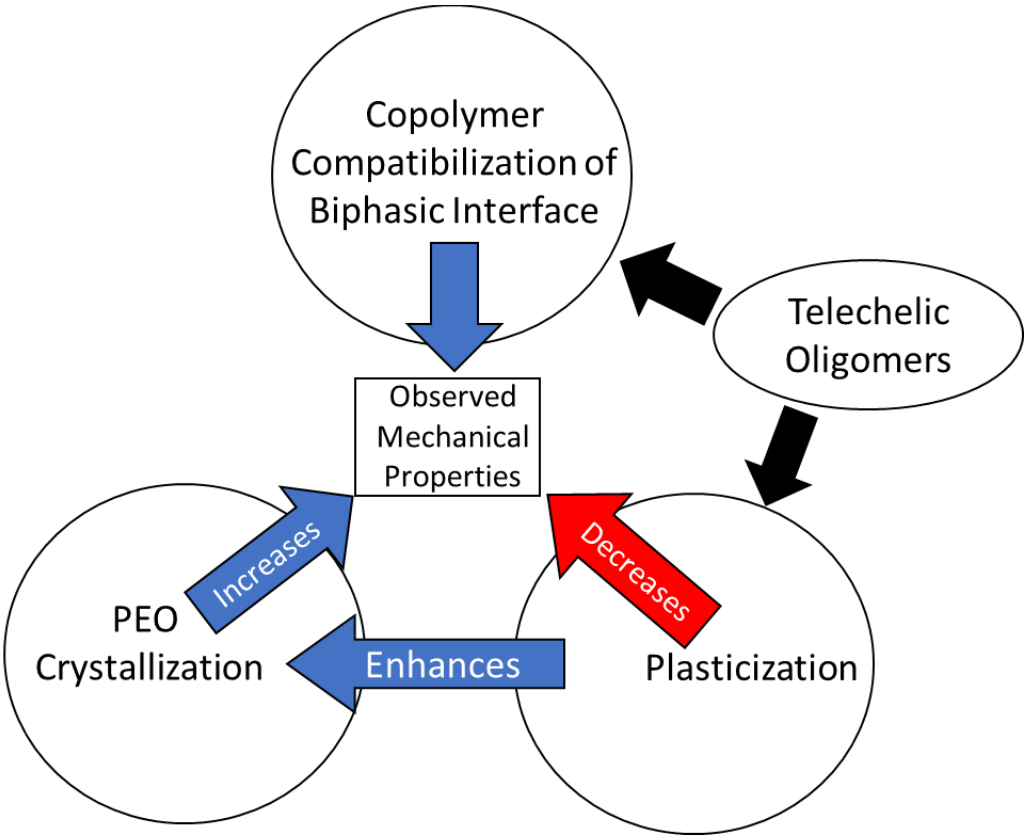


Fig 4.9. Diagram of molecular interactions in a 70/30 PBAE: PEO blend with telechelic oligomers at low loadings and the observed mechanical properties.

compatibilization to soften the material. Plasticization occurs in each blend at early times before the telechelics react, but can be mitigated at longer times if all the telechelic reacts and there is no excess after reaction. Thus, in designing successful reactive compatibilization of crystalline polymer blends, identifying an optimal loading of telechelic oligomer is crucial. This target composition will optimize beneficial compatibilization and crystallization processes and minimize plasticization. In the crystalline polymer blends studied here, the optimal oligomer loading is between 0.5 to 1 wt% to create compatibilized polymer blends with optimal properties.

Blend Morphology and Predictive Models

One limitation of these experiments and results is that the blend morphology has not been clearly identified, as it is known that the mechanical properties of phase separated blends can vary with morphology. Although the morphology of these samples has not been identified, previous work by our group suggests that it should form a spherical, isotropic rubbery phase dispersed into a continuous glassy phase. This conjecture is based on work in our group by Ashcraft et. al., that examined the morphology of a blend containing 10 wt% polyisoprene and 90 wt% polystyrene that is compatibilized with multiblock copolymers.[113] Figure 4.10, taken from Ashcraft's paper, shows the spherical morphology of the minor phase that is dispersed throughout the continuous polystyrene phase. Both polyisoprene and PEO have sub-0 ºC glass transition temperatures and are thus rubbery at room temperature, while the polystyrene and PBAE major phase are below their T_g and thus glassy at room temperature. An important distinction to make concerning the PEO minor phase is that, based on the results in Figure 4.7, the crystalline domains do not exceed 10 % of the total PEO content. Thus, we expect the minor phase in our blends to be mostly rubbery with such low crystallinity, but to also vary in modulus as the % crystallinity changes. From the similar composition between the blends and the distribution of rubbery material within a glassy

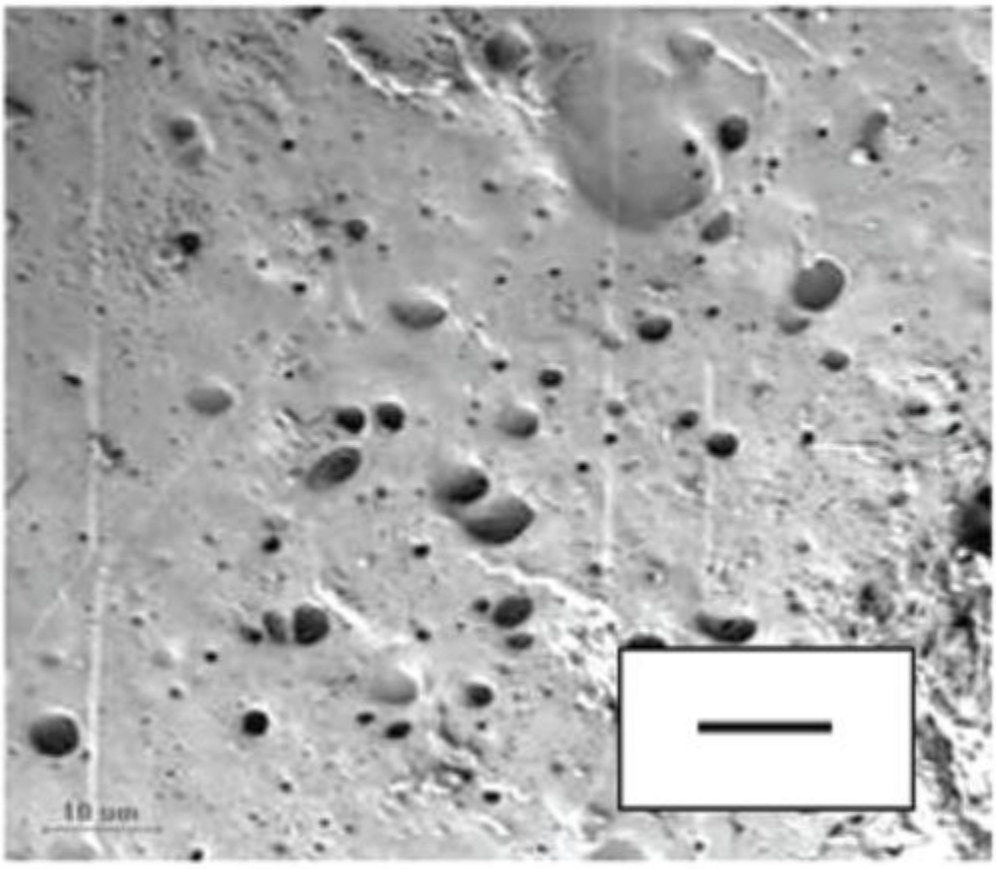


Fig. 4.10. SEM image of a 90:10 wt% Polystyrene/Polyisoprene blend compatibilized with telechelic oligomers (image from Ashcraft et. al.).[113] Scaling bar of image is 10 μm.

matrix, we expect that our samples will have a similar spherical blend morphology.

Predictive models exist to correlate the mechanical properties of a polymer mixture to the mechanical properties of the individual components. The morphology of blends with co-existing glassy and rubbery phases have been modeled by the Voight and Reuss models, which predict the composition dependence of mechanical properties of a blend.[121] The Voight or "parallel" model, (Equation 4.2), models a blend where the dispersed phase, the continuous phase, and the biphasic interface are parallel to a mechanical load, which equates to the equal deformation of each phase. As a result, the Voight model represents an upper mechanical property limit. Similarly, the Reuss or "series" model, (Equation 4.3), assumes the blend domains are arranged in consecutive series with the biphasic interface transverse to the applied force. Because the mechanical properties of a series assembly between blend components is dominated by the adhesion of the biphasic interface, this model sets the lower limit for the mechanical properties of the blend.

$$E_b = \varphi_r E_r + (1 - \varphi_r) E_g \qquad \text{Equation 4.2}$$

$$E_b = \left(\frac{\varphi_r}{E_r} + \frac{1-\varphi_r}{E_g}\right)^{-1} \qquad \text{Equation 4.3}$$

$$\varphi_r = \frac{V_r}{V_r + V_g} \qquad \text{Equation 4.4}$$

In Equations 4.2-4.4, the subscripts of *b*, *r*, and *g*, refer to the blend, the rubbery PEO minor phase, and the glassy PBAE major phase respectively, while E refers to the Young's modulus of the blend and its components and φ_r is the volume fraction of the PEO minor phase within the blend (Equation 4.4). While the calculation of mechanical property limits with the Voight/Reuss models works well to set a predictive distribution of experimental polymer blend behavior, the models assume that stress is continuous across the biphasic interface and that the exact phase morphology does not influence the model's prediction.

There also exist a number of more complex predictive models that account for the impact of specific structural characteristics of the blend morphology on mechanical properties.[122, 123] For instance, the Kerner model predicts the mechanical properties of a blend that is macroscopically isotropic and homogenous with a spherical minor phase morphology.[124, 125] The individual spheres are assumed to be bonded to the matrix phase with perfect adhesion so that displacement of the sample is continuous when stress is applied. Minor phase particles are modeled to be randomly isolated from one another and embedded within individual "shells" of matrix material that are surrounded by a continuous phase that has the mean properties of the entire blend The original form of Kerner's model predicts the composition dependence of the shear modulus (G_b), which can be adapted to a tensile geometry by the correlation of Young's modulus (E_b) to shear modulus (G_b) which requires knowledge of Poisson's ratio (ν_b) (Equation 4.5).[126]

$$E_b = 2(1 + \nu_b)G_b \qquad \text{Equation 4.5}$$

When stress is applied to a material, the Poisson effect is the tendency of the material to undergo an expansion or contraction in the direction orthogonal to the applied force. The ratio of the strain in the direction of the applied force (ε_L or $\varepsilon_{Longitudinal}$) to the strain perpendicular to this force (ε_{tr} or $\varepsilon_{transverse}$) is known as Poisson's ratio (Equation 4.6).

$$\nu_b = -\frac{\varepsilon_{tr}}{\varepsilon_L} \qquad \text{Equation 4.6}$$

For most polymers, Poisson's ratio is between 0.25 and 0.35 depending upon the molecular characteristics of the material. It is heavily influenced by the packing density of the polymer, or the arrangement of repeat units of the polymer chains. With increasing packing density, Poisson's ratio decreases relative to more amorphous materials. For this reason, we speculate that the PEO minor phase will have a lower Poisson's ratio compared to that of the PBAE phase, due to the

PEO's inherent crystallinity as shown in our results in Figure 4.7. Incorporating the relationship in Equation 4.5, the proper form of the Kerner model for tensile properties is (Equation 4.7).

$$\frac{E_b}{E_g} = \gamma \frac{(1-\varphi_r)E_g + \beta(\alpha-\varphi_r)E_r}{(1+\alpha\varphi_r)E_g + \alpha\beta(1-\varphi_r)E_r} \quad \text{Equation 4.7}$$

This form of the Kerner model is a simplification that uses the parameters α (Equation 4.8), β (Equation 4.9), and γ (Equation 4.10) to combine the dependence of the Young's modulus on the Poisson's ratios of the glassy PBAE phase (ν_g) and the rubbery PEO phase (ν_r).

$$\alpha = \frac{2(4-5\nu_g)}{(7-5\nu_g)} \quad \text{Equation 4.8}$$

$$\beta = \frac{(1+\nu_g)}{(1+\nu_r)} \quad \text{Equation 4.9}$$

$$\gamma = \frac{(1+\nu_b)}{(1+\nu_g)} \quad \text{Equation 4.10}$$

Given that we expect our blends examined here to exhibit this morphology, the Kerner model will probably be the most relevant to these studies. Therefore, the important parameters that we will need to determine experimentally to use the Kerner model to estimate the composition dependence of the Young's modulus of the blend using Equation 4.7 include the Young's modulus, and Poisson's ratio for each component in the blend.

Similarly, the Davies model (Equation 4.11) predicts the properties of co-continuous blend morphologies and assumes the blend is macroscopically isotropic and homogeneous.[127]

$$E_b^{1/5} = E_r^{1/5}(\varphi_r) + E_g^{1/5}(\varphi_g) \quad \text{Equation 4.11}$$

Amongst the various models that have been used to correlate the structure of blends with co-continuous morphologies to mechanical properties, the Davies model is the most consistent and does not have the limitations that persist in other models, such as the percolation limit.[122]

It is important to note that these models operate under the assumption that stress transfers between phases of the polymer blend continuously, which is inconsistent with the weak adhesive behavior between individual phases in uncompatibilized phase separated blends where polymer chains of the distinct phases do not entangle. For this reason, it is expected that the measured mechanical properties of the uncompatibilized blends will be lower than those predicted from the models. Conversely, in the compatibilized samples where interfacial strengthening is achieved via the formation of multiblock copolymer, the biphasic interface will support stress transfer between phases, thus the measured mechanical properties will approach the model prediction with increased compatibilization. Ultimately, although these predictive tools can help build the correlation between the blend morphology and the resulting mechanical properties, it is still necessary to obtain additional experimental evidence that supports the models. The most immediate way to accomplish this goal will be to conduct a series of imaging experiments with transmission electron microscopy (TEM), scanning electron microscopy (SEM), or atomic force microscopy (AFM). Previous compatibilization studies conducted by Ashcraft et. al. demonstrated that, with the proper solvent, the minor phase domains can be removed from a sample via solubilization.[113] The empty spaces left behind can then be imaged via SEM methods to conclusively determine the morphology of the minor phase as a function of annealing time and compatibilization.

Conclusion

In this series of experiments, we have examined the processes that impact the reactive compatibilization of a crystalline polymer blend with telechelic oligomers. The results show that three competing molecular level processes impact the successful reactive compatibilization of the blend – the interfacial modification of the blend, polymer crystallization and plasticization of the blend by unreacted oligomer. Reactions of telechelics at the biphasic interface occur rapidly after

mixing and extrusion, however, oligomers that do not become part of a compatibilizing copolymer chain at the biphasic interface remain as plasticizers in the blend that lower the Young's modulus. Moreover, the PEO in the blends crystallizes, a process that is accelerated in plasticized samples. The complex relationship between the molecular level processes of PEO crystallization, blend compatibilization, and plasticization was then fully elucidated by correlating the extent of PEO crystallinity to the modulus of the samples to identify those samples that exhibit enhanced moduli for a given extent of PEO crystallinity, which is ascribed to reactive compatibilization. Similarly, those samples that exhibited lower moduli for a given PEO crystallinity are attributed to the plasticization of the sample by unreacted oligomer.

Therefore, to obtain the optimum blend properties, a target oligomer composition is needed to maintain the desired balance of these molecular processes. The results of this study indicate that the target concentration of telechelic oligomers to effectively reactively compatibilize a crystalline polymer blend is between 0.5 and 1 wt%. Above oligomer concentrations of 0.5 to 1 wt%, a weak material with poor mechanical properties is generated by the plasticization of unreacted telechelic oligomers. These studies also show that the reaction of carboxylic acid and epoxy telechelic end groups is sufficiently rapid to form copolymer within the time of melt mixing, and was shown to be sufficiently fast to compatibilize the blend and improve the blend mechanical properties.

These studies therefore provide important fundamental information that is needed to design effective reactive compatibilization of crystalline polymer blends. With this foundation, a broad range of crystalline polymer blends can be rationally compatibilized by this reactive compatibilization scheme and processed to attain targeted mechanical capabilities both industrially and via recycling.

Chapter 5. Conclusions and Future Work

Conclusions

The accumulation of work in this dissertation has led to a number of important developments in both the additive manufacturing and polymer compatibilization fields. Analysis of various multi-amine solutions applied in situ to the interlayer interface of an FFF print demonstrated various improvements to print isotropy and overall mechanical integrity. By analyzing chemical crosslinker kinetics changes based on print thermal history and amine concentration, it was shown qualitatively that the reactivity of the amine material is not the primary factor influencing the increase in print mechanical strength but rather the overall presence of aromaticity within the molecular structure. Continuing the trend of FFF analysis, the effects on print irreversible thermal strain from the addition of nanoscale additives to the filament was investigated. Results indicate that, although nanoscale additives change the amount of irreversible thermal strain released, the most accurate measurement of these strain effects can only be obtained once the contributions of the changing interfilament void space are removed. With a more accurate estimation of irreversible thermal strain, the combination of these results with calorimetry experimentation demonstrates that the strain within a printed object is most heavily influenced by changes in the filament viscosity, molecular confinements, bead chain alignments, and plasticization effects generated by an additive's specific molecular properties. Lastly, our foray into the compatibilization of crystalline polymer blends with telechelic oligomers revealed an important interplay relationship of three molecular level processes and how they are directly influenced by the oligomer concentration. By utilizing a target additive composition, the detrimental effects of oligomer plasticization can be minimized while maximizing the inherent mechanical performance of the blends by a synergistic relationship between the blend crystallinity and the compatibilization of the biphasic interface.

Multi-amine additives and Interfilament FFF Crosslink Reactions

Our results document a method to generate interlayer covalent bonds in FFF-based additive manufacturing printing. Multi-amines placed at different solution concentrations between the layers of an ABS sample during filament deposition produced interlayer connections that greatly improve the interlayer fracture energy. This strengthening of the interlayer interface is attributed to amine reactions with oxidation-produced functional groups present on the polybutadiene portions of ABS filament during the printing process. The amount of interface strengthening was then correlated to the relative reactivity between each multi-amine and oxidized polybutadiene as determined by infrared analysis. This measured correlation demonstrated that the interlayer crosslink reactions have the fastest reaction rates at higher temperatures and thereby occur immediately after filament deposition. In addition, further analysis revealed that amine reactivity is not the principal factor governing the interlayer interface strength. On the contrary, it was the presence of aromatic or cyclic structures within the crosslinker that appear to have the most impact when generating more robust print interfaces. It was also shown that with higher loadings of crosslinker, there is a marked increase in the interlayer fracture energy. Cumulatively, these experiments and results provide a baseline to expanding this crosslinking method to several additive manufacturing materials and processes.

FFF Strain (ε) Variations with Nanoscale Additives

Experiments with nanoscale additives and their effects on the irreversible thermal strain ($\boldsymbol{\varepsilon}$) in FFF objects was successfully carried out by measuring the release of this strain with the annealing of printed PLA samples. Monoliths printed from PLA filaments that contain graphene or LMW 3-arm PLA additives had consistently higher irreversible thermal strain values compared

to unmodified PLA subjects. Irreversible thermal strain results measured herein are a combination of changes to the both the print's interfilament void spaces and the overall filament uniaxial dimensions. By removing the input of changing void space from the macroscopic measurements, a more accurate and quantified change in filament structure with annealing was presented. Evaluation of the corrected strain release value (ε_z*) demonstrated that the presence of LMW PLA within the filament generates higher amounts of strain, while the addition of graphene material to the filament keeps irreversible thermal strain to a level consistent with unmodified PLA. Calorimetry experimentation and analysis of each monolith type resulted in an observation of complex filament glass transition behavior with multiple transition steps and a large endotherm. A method of bridging the measured dimensional changes to the molecular level chain relaxation within the filament beads was thereby achieved. Our interpretation of these results elucidates that the use of graphene within PLA leads to slower chain dynamics and relaxation, which thereby increases the required thermal energy to transition the filament between glass and rubbery states and subsequently induce irreversible thermal strain developed throughout the print process. The addition of LMW PLA to the filament, however, generates lower material viscosity and may lead to an increase in filament chain alignment, which then produces an increased amount of irreversible thermal strain within the monolith. Overall, our experimental results show that nanoscale additives within PLA filament will alter the degree of irreversible thermal strain present in an object printed by FFF. A more homogeneous filament thermal history and increased molecular confinements is achieved from addition of the bulky two-dimensional graphene sheets that minimize residual strain buildup as a whole. A method to incorporate nanoscale additives while factoring in the complex connections between filament viscosity, thermal conductivity, and the observed irreversible thermal strain was achieved in this study, and ultimately provides further

scientific understanding that will progress additive manufacturing as a large-scale production technology.

Crystalline Polymer Blend Compatibilization

In our compatibilization experiments, we have determined the various molecular processes and their relationships that influence the reactive compatibilization of a crystalline polymer blend with telechelic oligomers. Cumulatively, the results specify and demonstrate the presence of three competing molecular level interactions that impact a completed blend compatibilization. These molecular processes include the polymer crystallization, plasticization via excess unreacted oligomer, and modifications to the blend's biphasic interface. Telechelic reactions at the biphasic interface quickly occur throughout the high temperature melt and extrusion phase. However, oligomers that do not become integrated into a compatibilizing copolymer chain via the reactive processes remain as plasticizers that decrease the Young's modulus of the blend. In addition, the PEO phase of the blend crystallizes with time, which can then be accelerated by samples with sufficient amounts of the plasticizing oligomer. The complex interplay of these blend dynamics was then better understood when the degree of PEO crystallinity in the blend was correlated to the blend modulus to determine samples with increased mechanical performance with a set amount of PEO crystallinity that is then attributed to the reactive compatibilization. Conversely, samples with lower moduli values at set PEO crystallinity were theorized to be weakened by plasticization from the unreacted oligomers.

In order to achieve optimum blend properties, a target oligomer concentration should be used to directly influence the necessary balance of the three competing molecular interactions. Our experimental results demonstrate that this target telechelic composition is between 0.5 to 1wt% when reactively compatibilizing a crystalline polymer blend. When this target composition is

surpassed, the polymer blend is weakened by plasticization effects from the unreacted excess oligomers. This study also demonstrates that the utilization of telechelics with carboxylic acid and epoxy end chain functionalities is sufficiently reactive with high enough reaction rates to form copolymer to improve blend mechanical properties and stabilize the biphasic interface within the relatively short time frame of melting and extrusion. These cumulative results provide foundational information that can be used to design competent reactive compatibilization schemes for crystalline polymer blends. A wide array of different crystalline blends now have the potential to be compatibilized via the logical steps generated from this baseline study to achieve tailor-made mechanical properties in both industry and recycling environments.

Summary

The initial overarching goal of this research has been to develop a molecular level understanding of the mechanisms and dynamics that produce two of FFF's biggest weaknesses that limit the method's full manufacturing potential. This process began with an investigation of print anisotropy, and the capabilities of multi-functional reactive additives to elicit an improved mechanical change as a result of interlayer covalent crosslinks that were generated by the complex, fluctuating thermal environment within a printer. With the success of these experiments from the addition of multi-amine crosslinkers, the research shifted focus towards understanding the complex factors associated with a print's irreversible thermal strain and how these can be influenced by the addition of nanoscale additives. Cumulative results indicated that nanoscale additives change the amount of irreversible thermal strain released from a print and that the magnitude of said strain is changed by modifying various molecular level factors of the filament. These filament characteristics include the viscosity and, theoretically, the overall amount of chain alignment that is generated within a filament bead during the deposition process. As a result of

these successful experimental endeavors, the complex changes in print anisotropy and irreversible thermal strain are made much clearer and have been provided with potential chemical interventions to limit their contribution to a print's thermomechanical validity.

Once these AM-based studies were concluded, and in the hopes of improving the efficiency with which the complex stream of waste polymers can be recycled from municipal sources, the next scientific task was to further our understanding of in situ reactive compatibilization of crystalline polymer blends with the use of telechelic oligomers. To this end, our experiments determined a complex molecular relationship between blend compatibilization, plasticization from unreacted oligomers, and crystallization of the PEO phase during processing. In order to bypass the blend weakening effects of plasticization while benefiting from compatibilization and crystallization, a target oligomer composition is needed when the additives are placed into the crystalline polymer blend. This optimal telechelic concentration, which we determined to be between 0.5 to 1 weight percent of the blend's composition, is crucial for future polymer recycling efforts as they are explored further in both industry and the recycling sectors.

Future Work

Our experiments and results presented above illustrate the potential for various nanoscale additives to improve 3D printing and polymer recycling at the molecular level via changes to polymer dynamics and interpolymer chemical reactions. Although the results have helped to illuminate very specific weaknesses within these methods, further experimentation can be used to improve these polymer systems. We will briefly discuss these potential studies for future reference below.

Interlayer Crosslinker Reactions with Various Filament Backbones Functionalities

It has been demonstrated in our experiments that, by placing multi-amine additives between the individual layers of a printed structure, the mechanical anisotropy of an FFF object can be reduced by chemical means. Our results have also determined that these reactions are the most viable when the thermal energy of the printed layer is at the highest point, immediately after deposition, and only by reacting with functional groups present on the backbone of the oxidized polybutadiene component of ABS filament. FFF is not limited solely to ABS materials, however, and there is a wide array of polymer filaments with unique chemical functionalities that are present in the repeating chain units. With these different functionalities comes the potential for additional interlayer crosslink reactions that could feasibly be produced under the conditions of an FFF print. Filaments such as nylon and PLA contain both amide and ester functionalities in each monomer segment, which would make both of these polymers ideal candidates for further interlayer reaction experiments.

In addition to analysis of different filament types, it would also be beneficial to investigate the direct influence of print parameters on the rate of these crosslink reactions. In the qualitative analysis of the crosslinker kinetics, it was determined that higher ambient print temperatures following filament deposition leads to faster reaction rates. The available thermal energy for the reaction also depends upon the continuous flow of heat via conduction with the heated bed surface which, if set to higher temperatures, may impact the rate at which the crosslinker formation occurs. Therefore, a series of experiments utilizing amines similar to DADPM with oxidized ABS filament at different nozzle and bed temperatures should elucidate how the reaction rate and any subsequent changes in mechanical performance are influenced from an increase in the available thermal energy.

Chain Alignment Effects on Interfilament Entanglement and Strain (ε)

As discussed in our study of nanoscale additives in PLA filament, we interpret the data to indicate that the amount of irreversible thermal strain that is generated within a print can be directly influenced by the additive's ability to induce additional chain alignments on the outer portion of the filament bead. To narrow this research focus and provide empirical evidence to support this claim, a series of small angle neutron scattering (SANS) experiments have begun as a collaboration between the National Institute of Standards and Technology and our research group. Preliminary results have been completed utilizing various polymethylmethacrylate (PMMA) and deuterated PMMA filament compositions, and ultimately an anisotropic scattering pattern was observed for each printed sample. This pattern is consistent with polymer chains aligned within a printed filament bead. Overall, the results indicate that SANS is a useful and innovative way to measure polymer chain alignment within FFF samples. Since these preliminary results were compiled, we have generated a new set of similar FFF monolith samples for experimentation. This new set of neutron scattering experiments will be used to measure how the interfilament chain alignment is changed when the sample material is annealed under similar conditions to our original irreversible thermal strain study. We also project that this experimental process will be the beginning of a much broader, more comprehensive study that will correlate the various printing parameters (i.e., nozzle temperature, print bed temperature, layer thickness, etc.) to the extent of molecular alignment within printed objects.

Dual Crystalline Polymer Blends and Reactive Compatibilization

The analysis and results in our PEO:PBAE experiments demonstrate that reactive compatibilization and mechanical improvements are possible for a mixed morphology polymer blend with both amorphous and crystalline phases. Although our findings on the molecular

interplay of plasticization, crystallization, and compatibilization as it is influenced by the specific telechelic concentration is important for the recycling of waste stream polymers, there is still one specific blend type that is unavoidable if all polymer materials are to become truly recyclable by reactive compatibilization methods. The polymer dynamics of blends that consist of two crystalline materials is still a massive research endeavor that is being investigated by polymer science today. Perhaps the most prominent example of this blending experimentation is the combination of polypropylene and polyethylene, which constitute an enormous portion of the polymer material that is found in municipal waste. For this reason, the study of reactive compatibilization to form multiblock copolymers with in-situ telechelic oligomers should be expanded into blends made from pairs of crystalline polymers to study how the original molecular dynamics and relationships discussed in this dissertation are changed under these conditions.

References

1. Lalegani Dezaki, M.; Mohd Ariffin, M. K. A.; Hatami, S., An overview of fused deposition modelling (FDM): research, development and process optimisation. *Rapid Prototyping Journal* **2021,** *27* (3), 562-582.
2. Leary, M., *Design for additive manufacturing*. Elsevier: Amsterdam, Netherlands ;, 2020.
3. Belaid, H.; Nagarajan, S.; Teyssier, C.; Barou, C.; Bares, J.; Balme, S.; Garay, H.; Huon, V.; Cornu, D.; Cavailles, V.; Bechelany, M., Development of new biocompatible 3D printed graphene oxide-based scaffolds. *Materials Science and Engineering: C* **2020,** *110*, 110595.
4. Li, Y.; Gao, S.; Dong, R.; Ding, X.; Duan, X., Additive Manufacturing of PLA and CF/PLA Binding Layer Specimens via Fused Deposition Modeling. *Journal of Materials Engineering and Performance* **2018,** *27* (2), 492-500.
5. Chesser, P.; Post, B.; Roschli, A.; Carnal, C.; Lind, R.; Borish, M.; Love, L., Extrusion control for high quality printing on Big Area Additive Manufacturing (BAAM) systems. *Additive manufacturing* **2019,** *28* (C), 445-455.
6. Roschli, A.; Gaul, K. T.; Boulger, A. M.; Post, B. K.; Chesser, P. C.; Love, L. J.; Blue, F.; Borish, M., Designing for Big Area Additive Manufacturing. *Additive manufacturing* **2019,** *25* (C), 275-285.
7. Auras, R., *Poly(lactic acid) synthesis, structures, properties, processing, and applications*. Wiley: Hoboken, N.J, 2010.
8. Dechy-Cabaret, O.; Martin-Vaca, B.; Bourissou, D., Controlled Ring-Opening Polymerization of Lactide and Glycolide. *Chemical reviews* **2004,** *104* (12), 6147-6176.
9. Peters, E. N., Plastics: Thermoplastics, Thermosets, and Elastomers. John Wiley & Sons, Inc: New York, 2002; pp 335-355.
10. Ding, Q.; Li, X.; Zhang, D.; Zhao, G.; Sun, Z., Anisotropy of poly(lactic acid)/carbon fiber composites prepared by fused deposition modeling. *Journal of applied polymer science* **2020,** *137* (23), 48786-n/a.
11. Lee, C. S.; Kim, S. G.; Kim, H. J.; Ahn, S. H., Measurement of anisotropic compressive strength of rapid prototyping parts. *Journal of Materials Processing Technology* **2007,** *187-188*, 627-630.
12. Ziemian, C.; Sharma, M.; Ziemian, S., Anisotropic mechanical properties of ABS parts fabricated by fused deposition modelling. *Mechanical engineering* **2012,** *23* (10.5772), 2397.
13. Coogan, T. J.; Kazmer, D. O., Bond and part strength in fused deposition modeling. *Rapid Prototyping Journal* **2017,** *23* (2), 414-422.
14. Fan, C.; Shan, Z.; Zou, G.; Zhan, L.; Yan, D., Interfacial Bonding Mechanism and Mechanical Performance of Continuous Fiber Reinforced Composites in Additive Manufacturing. *Chinese Journal of Mechanical Engineering* **2021,** *34* (1), 21.
15. Sun, Q.; Rizvi, G. M.; Bellehumeur, C. T.; Gu, P., Effect of processing conditions on the bonding quality of FDM polymer filaments. *Rapid Prototyping Journal* **2008,** *14* (2), 72-80.
16. Bakir, A. A.; Atik, R.; Ozerinc, S., Mechanical properties of thermoplastic parts produced by fused deposition modeling:a review. *Rapid Prototyping Journal* **2021,** *27* (3), 537-561.
17. Torrado, A. R.; Shemelya, C. M.; English, J. D.; Lin, Y.; Wicker, R. B.; Roberson, D. A., Characterizing the effect of additives to ABS on the mechanical property anisotropy of specimens fabricated by material extrusion 3D printing. *Additive Manufacturing* **2015,** *6*, 16-29.
18. Wach, R. A.; Wolszczak, P.; Adamus-Wlodarczyk, A., Enhancement of Mechanical Properties of FDM-PLA Parts via Thermal Annealing. *Macromolecular materials and engineering* **2018,** *303* (9), 1800169-n/a.

19. Dul, S.; Fambri, L.; Pegoretti, A., Fused deposition modelling with ABS-graphene nanocomposites. *Composites Part A: Applied Science and Manufacturing* **2016,** *85*, 181-191.
20. Waheed, S.; Cabot, J. M.; Smejkal, P.; Farajikhah, S.; Sayyar, S.; Innis, P. C.; Beirne, S.; Barnsley, G.; Lewis, T. W.; Breadmore, M. C.; Paull, B., Three-Dimensional Printing of Abrasive, Hard, and Thermally Conductive Synthetic Microdiamond−Polymer Composite Using Low-Cost Fused Deposition Modeling Printer. *ACS Appl. Mater. Interfaces* **2019,** *11*, 4353-4363.
21. Ye, W.; Wu, W.; Hu, X.; Lin, G.; Guo, J.; Qu, H.; Zhao, J., 3D printing of carbon nanotubes reinforced thermoplastic polyimide composites with controllable mechanical and electrical performance. *Composites Science and Technology* **2019,** *182*, 107671.
22. Shaffer, S.; Yang, K.; Vargas, J.; Di Prima, M. A.; Voit, W., On reducing anisotropy in 3D printed polymers via ionizing radiation. *Polymer (Guilford)* **2014,** *55* (23), 5969-5979.
23. Li, Q.; Zhao, W.; Niu, B.; Wang, Y.; Wu, X.; Ji, J.; Li, Y.; Zhao, T.; Li, H.; Wang, G., 3D printing high interfacial bonding polyether ether ketone components via pyrolysis reactions. *Materials & Design* **2021,** *198*, 109333.
24. Carneiro, O. S.; Silva, A. F.; Gomes, R., Fused deposition modeling with polypropylene. *Materials & Design* **2015,** *83*, 768-776.
25. Turner Brian, N.; Gold Scott, A., A review of melt extrusion additive manufacturing processes: II. Materials, dimensional accuracy, and surface roughness. *Rapid Prototyping Journal* **2015,** *21* (3), 250-261.
26. Kantaros, A.; Karalekas, D., Fiber Bragg grating based investigation of residual strains in ABS parts fabricated by fused deposition modeling process. *Materials & Design* **2013,** *50*, 44-50.
27. Rostom, S.; Dadmun, M. D., Improving heat transfer in fused deposition modeling with graphene enhances inter filament bonding. *Polymer Chemistry* **2019,** *10*, 5967-5978.
28. Park, D. W.; Roe, R. J., Effect of added block copolymer on the phase-separation kinetics of a polymer blend. 2. Optical microscopic observations. *Macromolecules* **1991,** *24* (19), 5324-5329.
29. Rigby, D.; Lin, J. L.; Roe, R. J., Compatibilizing effect of random or block copolymer added to binary mixture of homopolymers. *Macromolecules* **1985,** *18* (11), 2269-2273.
30. Flory, P. J., Thermodynamics of High Polymer Solutions. *The Journal of Chemical Physics* **1942,** *10* (1), 51-61.
31. Huggins, M. L., Some Properties of Solutions of Long-chain Compounds. *The Journal of Physical Chemistry* **1942,** *46* (1), 151-158.
32. Hiemenz, P. C.; Lodge, T., *Polymer chemistry*. Second edition. ed.; CRC Press: Boca Raton, FL, 2007.
33. Sanchez, I. C., Chapter 3 - Statistical Thermodynamics of Polymer Blends. In *Polymer Blends*, Paul, D. R.; Newman, S., Eds. Academic Press: 1978; pp 115-139.
34. Dadmun, M., Effect of Copolymer Architecture on the Interfacial Structure and Miscibility of a Ternary Polymer Blend Containing a Copolymer and Two Homopolymers. *Macromolecules* **1996,** *29* (11), 3868-3874.
35. Datta, S.; Lohse, D. J., *Polymeric Compatibilizers*. Hanser Gardner Publications: 1996.
36. Pellegrini, N. N.; Sikka, M.; Satija, S. K.; Winey, K. I., Segregation of a Random Copolymer from Miscible Blends. *Macromolecules* **1997,** *30* (21), 6640-6644.
37. Anastasiadis, S. H.; Gancarz, I.; Koberstein, J. T., Compatibilizing effect of block copolymers added to the polymer/polymer interface. *Macromolecules* **1989,** *22* (3), 1449-1453.

38. Heikens, D.; Barentsen, W., Particle dimensions in polystyrene/polyethylene blends as a function of their melt viscosity and of the concentration of added graft copolymer. *Polymer* **1977,** *18* (1), 69-72.
39. Fayt, R.; Jérôme, R.; Teyssié, P., Molecular design of multicomponent polymer systems. II. Emulsifying effect of a poly(hydrogenated butadiene-b-styrene) copolymer in high-density polyethylene/polystyrene blends. *Journal of Polymer Science: Polymer Physics Edition* **1981,** *19* (8), 1269-1272.
40. Shull, K. R.; Kramer, E. J.; Hadziioannou, G.; Tang, W., Segregation of block copolymers to interfaces between immiscible homopolymers. *Macromolecules* **1990,** *23* (22), 4780-4787.
41. Brown, H. R.; Deline, V. R.; Green, P. F., Evidence for cleavage of polymer chains by crack propagation. *Nature* **1989,** *341* (6239), 221-222.
42. Brown, H. R., Effect of a diblock copolymer on the adhesion between incompatible polymers. *Macromolecules* **1989,** *22* (6), 2859-2860.
43. Dai, C.-A.; Jandt, K. D.; Iyengar, D. R.; Slack, N. L.; Dai, K. H.; Davidson, W. B.; Kramer, E. J.; Hui, C.-Y., Strengthening Polymer Interfaces with Triblock Copolymers. *Macromolecules* **1997,** *30* (3), 549-560.
44. Eastwood, E. A.; Dadmun, M. D., Compatibilization of poly(vinyl chloride) and polyolefin elastomer blends with multiblock/blocky chlorinated polyethylenes. *Polymer* **2002,** *43* (25), 6707-6717.
45. Eastwood, E. A.; Dadmun, M. D., Multiblock Copolymers in the Compatibilization of Polystyrene and Poly(methyl methacrylate) Blends: Role of Polymer Architecture. *Macromolecules* **2002,** *35* (13), 5069-5077.
46. Schulze, J. S.; Moon, B.; Lodge, T. P.; Macosko, C. W., Measuring Copolymer Formation from End-Functionalized Chains at a PS/PMMA Interface Using FRES and SEC. *Macromolecules* **2001,** *34* (2), 200-205.
47. Talagani, F.; DorMohammadi, S.; Dutton, R.; Godines, C.; Baid, H.; Abdi, F.; Kunc, V.; Compton, B.; Simunovic, S.; Duty, C.; Love, L.; Post, B.; Blue, C., Numerical Simulation of Big Area Additive Manufacturing (3D Printing) of a Full Size Car. *Sampe Journal* **2015,** *51*, 27.
48. Ahn, S.-H.; Montero, M.; Odell, D.; Roundy, S.; Wright, P. K., Anisotropic material properties of fused deposition modeling ABS. *Rapid Prototyping* **2002,** *8* (4), 248-257.
49. Bellini, A.; Guceri, S., Mechanical characterization of parts fabricated using fused deposition modeling. *Rapid Prototyping* **2003,** *9* (4), 252-264.
50. Es-Said, O. S.; Foyos, J.; Noorani, R.; Mendelson, M.; Marloth, R.; Pregger, B. A., Effect of Layer Orientation on Mechanical Properties of Rapid Prototyped Samples. *Materials and Manufacturing Processes* **2000,** *15* (1), 107-122.
51. Agrawal, G.; Wool, R. P.; Dozier, W. D.; Felcher, G. P.; Zhou, J.; Pispas, S.; Mays, J. W.; Russell, T. P., Interdiffusion of polymers across interfaces. *Journal of Polymer Science Part B: Polymer Physics* **1996,** *34* (17), 2919-2940.
52. Bellehumeur, C.; Li, L.; Sun, Q.; Gu, P., Modeling of Bond Formation Between Polymer Filaments in the Fused Deposition Modeling Process. *Journal of Manufacturing Processes* **2004,** *6* (2), 170-178.
53. Levenhagen, N. P.; Dadmun, M. D., Bimodal molecular weight samples improve the isotropy of 3D printed polymeric samples. *Polymer* **2017,** *122*, 232-241.
54. Wool, R. P.; Willett, J. L.; McGarel, O. J.; Yuan, B. L., Strength of polymer interfaces. *Am. Chem. Soc. Polym. Prepr. Div. Polym. Chem.* **1987,** *28* (2), 38-39.

55. Hossain, M. S.; Ramos, J.; Espalin, D.; Perez, M.; Wicker, R., Improving tensile properties of FDM manufactured specimens via modifying build parameters. *Journal of Manufacturing Science and Engineering* **2014,** *136* (6), 380-392.
56. Huang, B.; Singamneni, S., Raster Angle Mechanics in Fused Depostion Modeling. *Journal of Composite Materials* **2014,** *49* (3), 363-383.
57. Davidson, J. R.; Appuhamillage, G. A.; Thompson, C. M.; Voit, W.; Smaldone, R. A., Design Paradigm Utilizing Reversible Diels−Alder Reactions to Enhance the Mechanical Properties of 3D Printed Materials. *Applied Materials and Interfaces* **2016,** *8*, 16961-16966.
58. Adeniyi, J. B.; Kolawole, E. G., Thermal and Photo-Degradation of Unstabilized ABS. *European Polymer Journal* **1984,** *20* (1), 43-47.
59. Duh, Y.-S.; Ho, T.-C.; Chenn, J.-R.; Kao, C.-S., Study on Exothermic Oxidation of Acrylonitrile-butadienestyrene (ABS) Resin Powder with Application to ABS Processing Safety. *Polymer* **2010,** (2), 174-187.
60. Guyader, M.; Audouin, L.; Colin, X.; Verdu, J.; Chevalier, S., Epoxides in the theral oxidation of polybutadiene. *Polymer Degradation and Stability* **2006,** *91*, 2813-2815.
61. Martin, R. B., Reactions of Carbonyl Compounds with Amines and Derivatives. *Journal of Physical Chemistry* **1963,** *68* (6), 1369-1377.
62. Aliheidari, N.; Tripuraneni, R.; Ameli, A.; Nadimpalli, S., Fracture resistance measurement of fused deposition modeling 3D printed polymers. *Polymer Testing* **2017,** *60*, 94-101.
63. Duty, C.; Kunc, V.; Compton, B.; Post, B.; Erdman, D.; Smith, R.; Lind, R.; Lloyd, P.; Love, L., Structure and mechanical behavior of Big Area Additive Manufacturing (BAAM) materials. *Rapid Prototyping Journal* **2017,** *23* (1), 181-189.
64. Kishore, V.; Ajinjeru, C.; Nycz, A.; Post, B.; Lindahl, J.; Kunc, V.; Duty, C., Infrared preheating to improve interlayer strength of big area additive manufacturing (BAAM) components. *Additive Manufacturing* **2017,** *14*, 7-12.
65. Lee, H.; Neville, K., Handbook of Epoxy Resins. **1967**.
66. William A. Henderson, J.; Schultz, C. J., The Nucleophilicity of Amines. *J. Org. Chem.* **1962,** *27* (12), 4643-4646.
67. Chapman, N. B.; Isaacs, N. S.; Parker, R. E., 386. The mechanism of epoxide reactions. Part I. The reactions of 1 : 2-epoxyethylbenzene, 1 : 2-epoxy-3-phenylpropane, and 1 : 2-epoxy-3-phenoxypropane with some secondary amines. *Journal of the Chemical Society (Resumed)* **1959,** (0), 1925-1934.
68. Badawi, H. M., A comparative study of the structure and vibrational spectra of diphenylmethane, the carcinogen 4,4'-methylenedianiline and 4,4'-methylenebis(N,N-dimethylaniline). *Spectrochimica Acta Part A: Molecular and Biomolecular Spectroscopy* **2013,** *109*, 213-220.
69. Horie, K.; Hiura, H.; Sawada, M.; Mita, I.; Kambe, H., Calorimetric investigation of polymerization reactions. III. Curing reaction of epoxides with amines. *Journal of Polymer Science Part A-1: Polymer Chemistry* **1970,** *8* (6), 1357-1372.
70. Rondan, N. G.; Marks, M. J.; Hoyles, S.; Pham, H., paper presented at the *225th ACS National Meeting*. **2003**.
71. Ellis, B., *Chemistry and Technology of Epoxy resins*, 1st ed. . Ashcroft, W. R., Ed. Blackie Academic and Professional Glasgow, U.K., 1993; pp 37, 71.
72. Fedtke, M.; Domaratius, F.; Pfitzmann, A., Curing of epoxy resins with dicyandiamide. *Polymer Bulletin* **1990,** *23* (4), 381-388.

73. Pham, H. Q.; Marks, M. J., Epoxy Resins. *Ullmann's Encyclopedia of Industrial Chemistry* **2005**.
74. Casavola, C.; Cazzato, A.; Moramarco, V.; Pappalettera, G., Residual stress measurement in Fused Deposition Modelling parts. *Polymer Testing* **2017,** *58*, 249-255.
75. D'Amico, A. A.; Debaie, A.; Peterson, A. M., Effect of layer thickness on irreversible thermal expansion and interlayer strength in fused deposition modeling. *Rapid Prototyping Journal* **2017,** *23* (5), 943-953.
76. Parlevliet, P. P.; Beukers, A., Residual Strains in Thick Thermoplastic Composites: An Experimental Approach. **2010**.
77. Spoerk, M.; Holzer, C.; Gonzalez-Gutierrez, J., Material extrusion-based additive manufacturing of polypropylene: A review on how to improve dimensional inaccuracy and warpage. *Journal of Applied Polymer Science* **2019,** *137* (12), 48545.
78. Wang, T.-M.; Xi, J.-T.; Jin, Y., A model research for prototype warp deformation in the FDM process. *The International Journal of Advanced Manufacturing Technology* **2007,** *33* (11), 1087-1096.
79. Duty, C.; Ajinjeru, C.; Kishore, V.; Compton, B.; Hmeidat, N.; Chen, X.; Liu, P.; Hassen, A. A.; Lindahl, J.; Kunc, V., What makes a material printable? A viscoelastic model for extrusion-based 3D printing of polymers. *Journal of Manufacturing Processes* **2018,** *35*, 526-537.
80. Xinhua, L.; Shengpeng, L.; Zhou, L.; Xianhua, Z.; Xiaohu, C.; Zhongbin, W., An investigation on distortion of PLA thin-plate part in the FDM process. *The International Journal of Advanced Manufacturing Technology* **2015,** *79* (5), 1117-1126.
81. D'Amico, A.; Peterson, A. M., An adaptable FEA simulation of material extrusion additive manufacturing heat transfer in 3D. *Additive Manufacturing* **2018,** *21*, 422-430.
82. Levenhagen, N. P.; Dadmun, M. D., Interlayer diffusion of surface segregating additives to improve the isotropy of fused deposition modeling products. *Polymer* **2018,** *152*, 35-41.
83. Seppala, J. E.; Migler, K. D., Infrared thermography of welding zones produced by polymer extrusion additive manufacturing. *Additive Manufacturing* **2016,** *12*, 71-76.
84. Spoerk, M.; Savandaiah, C.; Arbeiter, F.; Traxler, G.; Cardon, L.; Holzer, C.; Sapkota, J., Anisotropic properties of oriented short carbon fibre filled polypropylene parts fabricated by extrusion-based additive manufacturing. *Composites Part A: Applied Science and Manufacturing* **2018,** *113*, 95-104.
85. Du, F.; Fischer, J. E.; Winey, K. I., Coagulation method for preparing single-walled carbon nanotube/poly(methyl methacrylate) composites and their modulus, electrical conductivity, and thermal stability. *Journal of Polymer Science Part B: Polymer Physics* **2003,** *41* (24), 3333-3338.
86. D'Amico, T.; Barrett, C.; Presing, J.; Peterson, A. M., Micromechanical modeling of irreversible thermal strain. *Additive Manufacturing* **2019,** *27*, 91-98.
87. Costanzo, A.; Spotorno, R.; Candal, M. V.; Fernandez, M. M.; Muller, A. J.; Graham, R. S.; Cavallo, D.; McIlroy, C., Residual alignment and its effect on weld strength in material-extrusion 3D-printing of polylactic acid. *Additive Manufacturing* **2020,** *36*, 101415.
88. McIlroy, C.; Olmsted, P. D., Disentanglement effects on welding behaviour of polymer melts during the fused-filament-fabrication method for additive manufacturing. *Polymer* **2017,** *123*, 376-391.
89. Mu, M.; Clarke, N.; Composto, R. J.; Winey, K. I., Polymer Diffusion Exhibits a Minimum with Increasing Single-Walled Carbon Nanotube Concentration. *Macromolecules* **2009,** *42* (18), 7091-7097.

90. Alberto, M.; Bhavsar, R.; Luque-Alled, J. M.; Vijayaraghavan, A.; Budd, P. M.; Gorgojo, P., Impeded physical aging in PIM-1 membranes containing graphene-like fillers. *Journal of Membrane Science* **2018,** *563*, 513-520.
91. Karatrantos, A.; Clarke, N.; Kruger, M., Modeling of Polymer Structure and Conformations in Polymer Nanocomposites from Atomistic to Mesoscale: A Review. *Polymer reviews* **2016,** *56* (3), 385-428.
92. Rissanou, A.; Power, A.; Harmandaris, V., Structural and Dynamical Properties of Polyethylene/Graphene Nanocomposites through Molecular Dynamics Simulations. *Polymers* **2015,** *7* (3), 390-417.
93. Rissanou, A. N.; Harmandaris, V., A Molecular Dynamics Study of Polymer/Graphene Nanocomposites. *Macromolecular symposia.* **2013,** *331-332* (1), 43-49.
94. McIlroy, C.; Olmsted, P. D., Deformation of an amorphous polymer during the fused-filament-fabrication method for additive manufacturing. *Journal of Rheology* **2017,** *61* (2), 379-397.
95. Koning, C.; Van Duin, M.; Pagnoulle, C.; Jerome, R., Strategies for compatibilization of polymer blends. *Progress in Polymer Science* **1998,** *23* (4), 707-757.
96. Di Lorenzo, M. L.; Frigione, M., Compatibilization criteria and procedures for binary blends: A review. *Journal of Polymer Engineering* **1997,** *17* (6), 429-460.
97. Arlen, M. J.; Dadmun, M. D., The reinforcement of polystyrene and poly(methyl methacrylate) interfaces using alternating copolymers. *Polymer* **2003,** *44* (22), 6883-6889.
98. Xu, J.; Eagan, J. M.; Kim, S.-S.; Pan, S.; Lee, B.; Klimovica, K.; Jin, K.; Lin, T.-W.; Howard, M. J.; Ellison, C. J.; LaPointe, A. M.; Coates, G. W.; Bates, F. S., Compatibilization of Isotactic Polypropylene (iPP) and High-Density Polyethylene (HDPE) with iPP-PE Multiblock Copolymers. *Macromolecules* **2018,** *51* (21), 8585-8596.
99. Nomura, K.; Peng, X.; Kim, H.; Jin, K.; Kim, H. J.; Bratton, A. F.; Bond, C. R.; Broman, A. E.; Miller, K. M.; Ellison, C. J., Multiblock Copolymers for Recycling Polyethylene-Poly(ethylene terephthalate) Mixed Waste. *ACS Applied Materials & Interfaces* **2020,** *12* (8), 9726-9735.
100. Sheldon, R. A.; Norton, M., Green chemistry and the plastic pollution challenge: towards a circular economy. *Green Chemistry* **2020,** *22* (19), 6310-6322.
101. Ragaert, K.; Hubo, S.; Delva, L.; Veelaert, L.; Du Bois, E., Upcycling of contaminated post-industrial polypropylene waste: A design from recycling case study. *Polymer Engineering & Science* **2018,** *58* (4), 528-534.
102. Paul, D. R.; Newman, S., Polymer blends. **1978**.
103. Leibler, L., Theory of phase equilibria in mixtures of copolymers and homopolymers. 2. Interfaces near the consolute point. *Macromolecules* **1982,** *15* (5), 1283-1290.
104. Leibler, L., Emulsifying effects of block copolymers in incompatible polymer blends. *Makromolekulare Chemie. Macromolecular Symposia* **1988,** *16* (1), 1-17.
105. Benkoski, J. J.; Fredrickson, G. H.; Kramer, E. J., Effects of composition drift on the effectiveness of random copolymer reinforcement at polymer-polymer interfaces. *Journal of Polymer Science Part B: Polymer Physics* **2001,** *39* (20), 2363-2377.
106. Creton, C.; Kramer, E. J.; Hui, C. Y.; Brown, H. R., Failure mechanisms of polymer interfaces reinforced with block copolymers. *Macromolecules* **1992,** *25* (12), 3075-3088.
107. Balazs, A. C.; DeMeuse, M. T., Miscibility in ternary mixtures containing a copolymer and two homopolymers. Effect of sequence distribution. *Macromolecules* **1989,** *22* (11), 4260-4267.

108. Creton, C.; Kramer, E. J.; Hadziioannou, G., Critical molecular weight for block copolymer reinforcement of interfaces in a two-phase polymer blend. *Macromolecules* **1991,** *24* (8), 1846-1853.
109. Levitt, L.; Macosko, C. W., Shearing of Polymer Drops with Interface Modification. *Macromolecules* **1999,** *32* (19), 6270-6277.
110. Sabouri-Ghomi, M.; Ispolatov, S.; Grant, M., Molecular weight effects on chain pull-out fracture of reinforced polymeric interfaces. *Physical Review E* **1999,** *60* (4), 4460-4464.
111. Lu, Q.-W.; Hoye, T. R.; Macosko, C. W., Reactivity of common functional groups with urethanes: Models for reactive compatibilization of thermoplastic polyurethane blends. *Journal of polymer science. Part A, Polymer chemistry* **2002,** *40* (14), 2310-2328.
112. Yin, Z.; Koulic, C.; Jeon, H. K.; Pagnoulle, C.; Macosko, C. W.; Jerome, R., Effect of Molecular Weight of the Reactive Precursors in Melt Reactive Blending. *Macromolecules* **2002,** *35* (24), 8917-8919.
113. Ashcraft, E.; Ji, H.; Mays, J.; Dadmun, M., A Novel Reactive Processing Technique: Using Telechelic Polymers To Reactively Compatibilize Polymer Blends. *ACS Applied Materials & Interfaces* **2009,** *1* (10), 2163-2173.
114. O'Brien, C. P.; Rice, J. K.; Dadmun, M. D., Reactive processing with difunctional oligomers to compatibilize polymer blends. *European Polymer Journal* **2004,** *40* (7), 1515-1523.
115. O'Shaughnessy, B.; Sawhney, U., Reaction Kinetics at Polymer-Polymer Interfaces. *Macromolecules* **1996,** *29* (22), 7230-7239.
116. Guegan, P.; Macosko, C. W.; Ishizone, T.; Hirao, A.; Nakahama, S., Kinetics of Chain Coupling at Melt Interfaces. *Macromolecules* **1994,** *27* (18), 4993-4997.
117. Orr, C. A.; Cernohous, J. J.; Guegan, P.; Hirao, A.; Jeon, H. K.; Macosko, C. W., Homogeneous reactive coupling of terminally functional polymers. *Polymer* **2001,** *42* (19), 8171-8178.
118. Wunderlich, B., Thermal Analysis. Academic Press: 1990; pp 417-431.
119. Fetters, L. J.; Lohse, D. J.; Richter, D.; Witten, T. A.; Zirkel, A., Connection between Polymer Molecular Weight, Density, Chain Dimensions, and Melt Viscoelastic Properties. *Macromolecules* **1994,** *27* (17), 4639-4647.
120. Wu, S., Chain structure and entanglement. *Journal of polymer science. Part B, Polymer physics* **1989,** *27* (4), 723-741.
121. Ruckdaschel, H.; Sandler, J. K. W.; Altstadt, V.; Schmalz, H.; Abetz, V.; Muller, A. H. E., Toughening of immiscible PPE/SAN blends by triblock terpolymers. *Polymer (Guilford)* **2007,** *48* (9), 2700-2719.
122. Joseph, S.; Thomas, S., Modeling of tensile moduli in polystyrene/ polybutadiene blends. *Journal of Polymer Science Part B: Polymer Physics* **2002,** *40* (8), 755-764.
123. Kummerlowe, C.; Kammer, H. W.; Malinconico, M.; Martuscelli, E., Polymer blends of poly(p-phenylene 1,3,4-oxadiazole) and poly(p-phenylene terephthalamide): morphology and mechanical behaviour. *Polymer* **1993,** *34* (8), 1677-1683.
124. Kerner, E. H., The Elastic and Thermo-elastic Properties of Composite Media. *Proceedings of the Physical Society. Section B* **1956,** *69* (8), 808-813.
125. Sonnenschein, M. F., In *Polyurethanes: Science, Technology, Markets, and Trends, Second Edition*, John Wiley and Sons: 2021; pp 133-166.
126. Bandyopadhyay, G. G.; Bhagawan, S. S.; Ninan, K. N.; Thomas, S., Viscoelastic behavior of polypropylene/nitrile rubber thermoplastic elastomer blends: Application of Kerner's models

for reactively compatibilized and dynamically vulcanized systems. *Journal of Polymer Science Part B: Polymer Physics* **2004,** *42* (8), 1417-1432.
127. Davies, W. E. A., The theory of elastic composite materials. *Journal of Physics D: Applied Physics* **1971,** *4* (9), 1325-1339.

Vita

Stevenson Connor Perryman was born in Columbia, Tn. His childhood and teen years were spent in Chapel Hill, Tn, where his family roots run deep. After graduating from Forrest High School in 2011, Connor began his undergraduate career at Austin Peay State University, where he would graduate Magna Cum Laude with a Bachelor of Science in Chemistry in 2015. Following a beneficial summer research experience in 2014, Connor would again advance his education by entering the doctorate program at the University of Tennessee, Knoxville as a member of Dr. Mark Dadmun's research group. In November 2021, Connor successfully defended his dissertation and graduated in the Fall of 2021 with a Ph. D. in Chemistry and Polymer Science.